④

Applied Research Laboratory

Technical Report

MEASUREMENT OF THE COMPLEX REFLECTIVITY OF SUBMERGED THIN PLATES AT OBLIQUE INCIDENCE ANGLES USING THE TWO-SENSOR INTENSITY TECHNIQUE

by

D. W. DeVilbiss
A. D. Stuart

PENNSTATE

4

The Pennsylvania State University
APPLIED RESEARCH LABORATORY
P.O. Box 30
State College, PA 16804

MEASUREMENT OF THE COMPLEX REFLECTIVITY OF SUBMERGED THIN PLATES AT OBLIQUE INCIDENCE ANGLES USING THE TWO-SENSOR INTENSITY TECHNIQUE

by

D. W. DeVilbiss
A. D. Stuart

Technical Report No. TR 90-012
August 1990

Supported by:
Space and Naval Warfare Systems Command

L.R. Hettche, Director
Applied Research Laboratory

Approved for public release; distribution unlimited

REPORT DOCUMENTATION PAGE

Form Approved
OMB No. 0704-0188

1. AGENCY USE ONLY *(Leave blank)*

2. REPORT DATE
August 1990

3. REPORT TYPE AND DATES COVERED

4. TITLE AND SUBTITLE
Measurement of the Complex Reflectivity of Submerged Thin Plates at Oblique Incidence Angles Using the Two-Sensor Intensity Technique

5. FUNDING NUMBERS

6. AUTHOR(S)
D. W. DeVilbiss, A. D. Stuart

7. PERFORMING ORGANIZATION NAME(S) AND ADDRESS(ES)

Applied Research Laboratory
The Pennsylvania State University
P. O. Box 30
State College, PA 16804

8. PERFORMING ORGANIZATION REPORT NUMBER
TR 90-012

9. SPONSORING/MONITORING AGENCY NAME(S) AND ADDRESS(ES)

Space and Naval Warfare Systems Command
Department of the Navy
Washington, DC 20363-5100

10. SPONSORING/MONITORING AGENCY REPORT NUMBER
N-00039-88-C-0051

11. SUPPLEMENTARY NOTES

12a. DISTRIBUTION/AVAILABILITY STATEMENT
Unlimited

12b. DISTRIBUTION CODE

13. ABSTRACT *(Maximum 200 words)*

This study has involved the adaptation of the two-sensor acoustic intensity measurement method to an underwater environment. The intensity technique involves measuring the acoustic pressure at two closely spaced points. The average of the pressures approximates the pressure at the midpoint of the two sensors while the difference between the pressures and the application of the Euler's equation leads to an approximation for the acoustic particle velocity at the midpoint between the two sensors. These two quqntities, the acoustic pressure and the acoustic particle velocity, are all that is needed to approximate the acoustic intensity and the acoustic impedance. The objective of this research was to develop the system and use it to measure the complex reflectivity of submerged thin plates at non-normal angles of incidence. The two-sensor technique has advantages over more conventional methods of measuring the reflectivity in that the sensors need only be positioned once during the test. This leads to a savings in effort and time for the experimenter. The source of acoustic energy used to ensonify the plates took the form of a parametric or virtual and fire array. The parametric array is formed by exciting a transducer with a high frequency carrier signal which has been amplitude modulated with a low frequency signal. The nonlinear characteristics of the medium create a low

14. SUBJECT TERMS
Keywords: complex reflectivity, plates, intensity, underwater, parametric array, [illegible]

15. NUMBER OF PAGES
121

16. PRICE CODE

17. SECURITY CLASSIFICATION OF REPORT
UNCLASSIFIED

18. SECURITY CLASSIFICATION OF THIS PAGE
UNCLASSIFIED

19. SECURITY CLASSIFICATION OF ABSTRACT
UNCLASSIFIED

20. LIMITATION OF ABSTRACT
SAR

NSN 7540-01-280-5500

Standard Form 298 (Rev 2-89)
Prescribed by ANSI Std. Z39-18
298-102

90 09 [illegible]

13. ABSTRACT (Continued)

frequency difference signal whose frequency is equal to the modulation frequency. This source has a particularly beneficial characteristic in that the beamwidth of the low frequency signal is on the order of that of the high frequency signal. By using this type of source, we were able to concentrate the acoustic pressure on the center of the test plate, thereby reducing the edge effects caused by finite plate size. This thesis describes the theory and experiments which were employed while developing the intensity and parametric array systems. A comparison of theoretical values to experimental data is made for the cases of a thin aluminum plate and a pressure release boundary. This comparison shows good agreement between theory and experiment. Experimental values for the reflectivity of an aluminum plate covered with thin rubber acoustic tiles shows the usefulness of this technique for measuring the non-normal reflectivity for an unknown sample.

ABSTRACT

This study has involved the adaptation of the two-sensor acoustic intensity measurement method to an underwater environment. The intensity technique involves measuring the acoustic pressure at two closely spaced points. The average of the pressures approximates the pressure at the midpoint of the two sensors while the difference between the pressures and the application of the Euler's equation leads to an approximation for the acoustic particle velocity at the midpoint between the two sensors. These two quantities, the acoustic pressure and the acoustic particle velocity, are all that is needed to approximate the acoustic intensity and the acoustic impedance. The objective of this research was to develop the system and use it to measure the complex reflectivity of submerged thin plates at non-normal angles of incidence. The two-sensor technique has advantages over more conventional methods of measuring the reflectivity in that the sensors need only be positioned once during the test. This leads to a savings in effort and time for the experimenter. The source of acoustic energy used to ensonify the plates took the form of a parametric or virtual end fire array. The parametric array is formed by exciting a transducer with a high frequency carrier signal which has been amplitude modulated with a low frequency signal. The nonlinear characteristics of the medium create a low frequency difference signal whose frequency is equal to the modulation frequency. This source has a particularly beneficial characteristic in that the beamwidth of the low frequency signal is on the order of that of the high frequency signal. By using this type of source, we were able to concentrate the acoustic pressure on the center of the test plate, thereby reducing the edge effects caused by finite plate size. This thesis describes the theory and experiments which were employed while developing the intensity and parametric array systems. A comparison of theoretical values to experimental data is made for the cases of a thin aluminum plate and a pressure release boundary. This comparison shows good agreement between theory and experiment. Experimental values for the reflectivity of an aluminum plate covered with thin rubber acoustic tiles shows the usefulness of this technique for measuring the non-normal reflectivity for an unknown sample.

TABLE OF CONTENTS

Page

Chapter

TABLE OF CONTENTS (continued)

TABLE OF CONTENTS (continued)

LIST OF FIGURES

LIST OF FIGURES (continued)

LIST OF FIGURES (continued)

LIST OF FIGURES (continued)

NOMENCLATURE

A	Active area of piston
c	Speed of sound
$C(\theta)$	Normalized angular dependence
e	Field amplitude difference
$E\{x(t)\}$	Expected value of x(t)
H_{12}	Initial transfer function
H^{s}_{12}	Switched transfer function
$\vec{I}$	Acoustic intensity
$\vec{I}_r$	Active intensity
$Im\,[x]$	Imaginary part of x
k	Acoustic wavenumber
L_*	Primary wave matching distance
P	Real valued acoustic pressure magnitude
p(t)	Acoustic pressure
$\vec{Q}_r$	Reactive intensity
$\vec{r}$	Field point location
R	Real part of the specific acoustic impedance
r_0	Rayliegh distance
Δr	Microphone separation
$Re\,[x]$	Real part of x
SL	Source level
SPL	Sound pressure level
$S_{p_n p_n}(\omega)$	Autospectrum
$S_{p_n p_m}(\omega)$	Cross Spectrum

NOMENCLATURE (continued)

T	Kinetic energy
$\vec{u}(t)$	Acoustic particle velocity
U_a	Real part of the particle velocity
U_r	Imaginary part of the particle velocity
V	Potential energy
X	Imaginary part of the specific acoustic impedance
$\bar{Z}$	Specific acoustic impedance
α	Absorption coefficient
δ	Magnitude mismatch
ε_b	Bias error
λ	Wavelength
μ_F	Viscosity
η_b	Estimation bias error
$\Delta\phi$	Electronic phase mismatch
ρ_o	Density
ω	Angular frequency
ω_o	Carrier frequency
ω_Δ	Difference frequency
$*$	Complex conjugate

Chapter 1

HISTORICAL BACKGROUND AND OBJECTIVES

1.1. Introduction

When sound is incident on the boundary between two media, a percentage of the acoustic energy is transmitted into the second medium, the rest is reflected back into the first medium. Knowledge of these percentages is important when one is trying to understand how sound reacts when it impinges on an object. This research concerns the reflection of sound off various submerged panels at both normal and non-normal angles of incidence.

The approach was to measure the specific acoustic impedance and it is based on the two-sensor acoustic intensity measurement method. The basis of this method is to use the average of the acoustic pressure between the two closely-spaced points to approximate the pressure at their midpoint. The gradient between the two pressures and the linearized Euler's equation leads to an approximation of the acoustic particle velocity. From these two approximations, we can calculate either the acoustic intensity or the acoustic impedance. Intensity is the product of acoustic pressure and acoustic particle velocity at a particular frequency while impedance is the ratio of these quantities. This study was concerned with the measurement of the acoustic impedance but for completeness, a discussion of the acoustic intensity measurement scheme and instrumentation is also given.

It will be shown in a later chapter that the specific acoustic impedance can also be calculated from the active and reactive acoustic intensities and the kinetic energy. Therefore, it is possible to use an existing intensity measurement system to measure the specific acoustic impedance. Once we know the specific acoustic impedance, we can calculate the complex reflectivity via a simple expression.

The existing in-air intensity measurement system was adapted to make underwater measurements by changing the software to account for the different parameters of the medium, such as density and speed of sound, and by using hydrophones instead of microphones.

Another interesting aspect of this research was the use of a nonlinear parametric array as a source of acoustic energy. By transmitting an amplitude modulated, high frequency signal at levels which are high enough to make the medium react nonlinearly, a low frequency difference signal is generated whose frequency is equal to the modulation frequency. This method of generating the low frequency signal has particularly beneficial effects in that the beamwidth of the low frequency difference signal is on the order of the beamwidth of the high frequency carrier signal and there are no side lobes created. By using a parametric array, we were able to generate low frequency signals with much narrower beamwidths than is possible with any conventional source.

This study compares the predicted complex reflectivities of submerged thin plates calculated using well known formulations to those measured with the experimental setup. The materials studied included a 3/8 inch thick aluminum sheet, a pressure release boundary material and a 3/8 inch thick aluminum sheet covered with 1/4 inch thick rubber tiles.

1.2. Impedance Measurement Methods

Measurement of the absorptive and reflective properties of materials in air has been accomplished since the early 1900's when Taylor[1] developed a method of measuring the sound absorption of a material in a tube. This method required the measurement of the maximum and minimum pressure amplitudes in the standing wave field set up in the tube. From these amplitudes, Taylor was able to calculate the absorptive properties of the material. This method, however, is only valid for sound normally incident on the material.

Further development of Taylor's concept resulted in a technique to measure the complex acoustic impedance of a material. Wente and Bedell[2] modified Taylor's method to account for the phase shift which results when sound impinges on a surface. The measurement of this complex acoustic impedance requires the measurement of not only the level of the maximum and minimum acoustic pressures, but also the distance from the sample to the first pressure minimum. Again, this method only applied for normal incidence.

The first use of the tube technique in underwater sound measurements was made by Meyer, et al.[3]. Instead of using steady state sound excitation and measuring the standing-wave field set up in the tube, the technique involves exciting the medium with sound pulses of short duration, thus allowing the temporal separation of the incident and reflected fields. Comparison of the incident and reflected pulse amplitudes leads to a characterization of the absorptive characteristics of the material under investigation. Measurement of the complex impedance is a little more difficult in that the phase change of the reflected wave must be measured. Measurement of the phase change required a relative comparison with a reference reflector.

Measurements of acoustic properties using the tube techniques described can be very time consuming. The standing wave in the tube is usually measured manually by moving the microphone in the tube while exciting the tube at discrete frequencies. In order for the phase to be accurately determined, the location of the nodes must be accurately measured.

In 1946, Bolt and Petrauskas[4] introduced a technique using two stationary microphones. It was not until the 1970's, however, with the advent of modern signal processing hardware that their technique became feasible. Seybert and Ross[5] and Chung and Blaser[6] were able to use the modern hardware to implement Bolt and Petrauskas' technique. The methods developed by these authors use either the transfer function or the cross-spectrum between the two microphones to resolve the incident and reflected fields. This method can be used for broad-band random excitation, not just single frequency excitation. Using the information concerning the incident and reflected fields, the complex impedance can be calculated. This method alleviates the need for single frequency excitation and the need to move the microphone to measure the standing wave field.

Recently, the two microphone method has been developed for use in underwater measurements. In 1983, Corbett[7] adapted the methods developed by Seybert and Ross, and Chung and Blaser for measurements in water filled tubes. Corbett excited a pulse tube using steady state sound. By measuring the transfer function between the pressures at two closely spaced hydrophones, he was able to calculate the complex reflectivity of materials at normal incidence.

All of the work presented so far deals with normally incident sound. There has been some work dealing with non-normal incidence. One method of measuring the non-normal absorptive properties developed by Sides and Mulholland[8] is based on the standing wave method employed in tubes. The measurement of the absorption characteristics for non-normal angles of incidence is made in a free field environment, not in a tube. A probe is used to measure the standing wave field in the same manner as it was in the tube.

Other methods using impulses as sources of sound have been developed. Davies and Mulholland[9] measured the normal impedance at oblique incidence by comparing the acoustic impulses at the surface of the absorbing material with those at a reference point recorded remote from the surface. Crammond and Don[10] measured the acoustic impedance of a grass surface using two microphones to simultaneously measure the direct and reflected impulses. The concept is the same as that of Meyer, et al. Allard and Sieben[11] used the transfer function between two closely spaced microphones to measure the impedance with normally incident sound. This method was further developed by Allard, et al.[12] to measure the acoustic impedance at oblique angles.

1.3. Development of the Parametric Array

The development of the theory regarding the parametric array began with work by Lighthill[13] on the sound produced by turbulence. Lighthill found the exact equation of motion for an arbitrary fluid. This equation of motion also holds for the interaction of sound beams. The development of this equation was the beginning point for many of the subsequent studies concerning the parametric array.

In 1956, Ingard and Pridmore-Brown[14] studied the pressure fields produced by a parametric array at the sum and difference frequency. They were able to derive an expression for the far field pressure at the sum frequency by neglecting viscous effects. They calculated and measured the sum and difference frequency components scattered from the interaction region of two sound beams in air intersecting each other at right angles.

Westervelt[15,16] studied the scattering of sound by sound. He developed an expression which characterized the far field behavior when two sound waves pass through a common region. Further work by Westervelt[17] produced an expression which describes the sound field formed by what he called a parametric array. The term parametric array was chosen because the array is formed by the nonlinear parameters of the medium. He studied the field produced by two high frequency collimated beams of sound. Included in Westervelt's derivations was an expression for the far field sound pressure produced by the parametric array and the beamwidth associated with the array.

Lauvstad and Tjötta[18] extended Westervelt's far field analysis to account for the finite apertures of the primary beams. Muir and Willette[19] accounted for the directivity of the array at the two primary frequencies by assuming that most nonlinear interaction occurs beyond the near field and then integrating over the product of the primary beam directivity functions. This formulation is restricted to the far field.

Near field analysis of the parametric array was performed by Berktay and Shooter[20]. They found an exact closed-form solution to the acoustic field produced by a continuous end fire array. Analysis by Novikov, et al.[21] resulted in a closed-form analytical near field solution for primary beam patterns that where Gaussian in shape. In his analysis, Fenlon[22] also assumed a Gaussian shaped beam patterns. He derived expressions describing the difference frequency field formed by the excitation of square, line, and rectangular radiators. These expressions give results which are in agreement with experiments throughout the near field and far field regions of the array.

1.4. Outline of the Thesis

Chapter 2 will introduce the theory for the two-sensor intensity and impedance measurement technique. Included is a description of the derivation of the intensity, energy, and impedance frequency domain estimators. Also discussed are the inherent errors of the two-sensor technique.

Chapter 3 gives a description of the parametric array used as a source. Included are the experiments conducted to measure the axial response and the beamwidths. An intensity scan of an on-axis plane of the parametric array is given.

Chapter 4 discusses the experimental system used in making the measurements. Included is a description of the intensity system hardware and software, probe hydrophone selection, and a description of the measurement environment. Also included in this chapter is a description of the instrumentation used to form the parametric array.

Chapter 5 describes the experiments conducted and compares the experimental results with the theoretical calculations. Included are the real and imaginary impedances measured for the aluminum plate, the pressure release boundary and the rubber tile covered aluminum plate. Conclusions and recommendations for further research are given at the end of this chapter.

Chapter 2

ACOUSTIC INTENSITY, ENERGY, AND IMPEDANCE ESTIMATORS

2.1. Introduction

In order to get a full understanding of the work performed in this research, it is necessary to first develop an understanding of the basic theory involved in experimentally measuring the acoustic intensity, energy, and impedance. This chapter gives an overview of the derivations and approximations used to calculate these quantities, as well as the inherent errors involved.

2.2. Theory

Measurement of acoustic intensity and energy requires the knowledge of both the acoustic pressure and the acoustic particle velocity at a single point at an instant of time. The average or effective acoustic intensity, $\vec{I}$, is defined here as the expected or mean value of the instantaneous intensity, $\vec{I}(t)$,

$$\vec{I} = E\left\{\vec{I}(t)\right\} = E\left\{p(t)\,\vec{u}(t)\right\} \tag{2.1}$$

where the expected or mean value operator is defined for a stationary ergodic process, x(t), as

$$E\left\{x(t)\right\} = \lim_{T\to\infty} \frac{1}{T}\int_{-T/2}^{T/2} x(t)\,dt \quad . \tag{2.2}$$

The measurement of acoustic pressure in air and water has been made for many years using simple pressure sensitive transducers. A practical and accurate transducer for the measurement of the acoustic particle velocity has, however, not been developed. An approximation to this last quantity, the acoustic particle velocity, can be developed from Euler's equation. This equation relates the time derivative of the particle velocity to the gradient of the acoustic pressure by

$$\rho_o \frac{\partial \vec{u}\left(\vec{r}, t\right)}{\partial t} = - \nabla\, p\left(\vec{r}, t\right) \quad . \tag{2.3}$$

The particle velocity $\vec{u}\left(\vec{r}, t\right)$ can, at some location $\vec{r}$, be calculated from the time integral

$$\vec{u}\left(\vec{r}, t\right) = - \frac{1}{\rho_o} \int \nabla p\left(\vec{r}, t\right) dt \quad . \tag{2.4}$$

The gradient of the pressure $\nabla p\left(\vec{r}, t\right)$ can be estimated using a finite difference approximation

$$\nabla \hat{p}\left(\vec{r}, t\right) = \frac{\partial \hat{p}\left(\vec{r}, t\right)}{\partial r} \approx \frac{p_2\left(r_2, t\right) - p_1\left(r_1, t\right)}{\Delta r} \tag{2.5}$$

where $p_1\left(r_1, t\right)$ and $p_2\left(r_2, t\right)$ are the pressures measured at two closely spaced points, $r_1 = r - \Delta r/2$ and $r_2 = r + \Delta r/2$, by the pressure sensors and Δr is the distance between those two sensors. The dimensions r_1, r_2, and Δr are shown in Figure 2.1. Using the

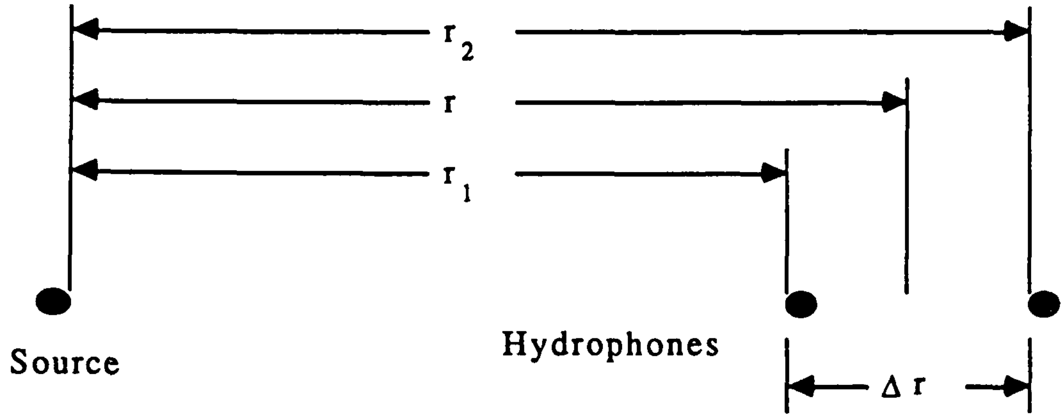

Figure 2.1. Sketch of sensor positioning.

linearized Euler's equation leads to an approximation of the component of the acoustic particle velocity which lies along a line joining the two sensors. This quantity is estimated by

$$\vec{u}(\vec{r}, t) \approx -\frac{1}{\rho_o \Delta r}\int \left[p_2(r_2, t) - p_1(r_1, t)\right] dt \quad . \qquad (2.6)$$

The acoustic pressure at the center point between the two sensors is approximated by the average of the acoustic pressures

$$\hat{p}(r, t) \approx \frac{p_1(r_1, t) + p_2(r_2, t)}{2} \quad . \qquad (2.7)$$

An estimate for the acoustic intensity can now be obtained by using Eq.(2.1), Eq.(2.6), and Eq.(2.7). This estimation is given as

$$\vec{I}(r) = -\frac{1}{2\rho_o \Delta r} E\left\{\left[p_1\left(r_1, t\right) + p_2\left(r_2, t\right)\right]\int\left[p_2\left(r_2, t\right) - p_1\left(r_1, t\right)\right] dt\right\} . \tag{2.8}$$

Work by Elko[23] leads to a frequency domain estimation of the acoustic intensity. This estimation gives the intensity in terms of the autospectra and cross-spectrum measured at the two pressure sensors. In his derivation, Elko makes an implicit assumption that the acoustic pressure field, p(r,t), is a stationary and ergodic. The estimate of the acoustic intensity spectra, at the field location r, is the sum of the active and reactive intensity spectra as shown in Appendix A,

$$\vec{I}^{c}(\omega) = \vec{I}\,(r, \omega) + j\,\vec{Q}\,(r, \omega) \tag{2.9}$$

where the real or active intensity is given (see Eq.(A.8))

$$\vec{I}(\omega) = \frac{1}{\omega \rho_o \Delta r} Im \left[S_{p_1 p_2}(\omega)\right] \tag{2.10}$$

and the imaginary or reactive intensity is given (see Eq.(A.9))

$$\vec{Q}(\omega) = \frac{1}{2\omega \rho_o \Delta r}\left[S_{p_2 p_2}(\omega) - S_{p_1 p_1}(\omega)\right] \quad . \tag{2.11}$$

For completeness, a derivation of the frequency domain estimators for the active and reactive intensities is given in Appendix A.

Development of the potential and kinetic energies follows in a similar manner as did that for the acoustic intensity. The first of these, the potential energy density $\left(\mathrm{N\text{-}m/m^3}\right)$ is defined as

$$V = \frac{1}{4\rho_o c^2} E\left\{p(t)\, p(t)\right\} \quad . \tag{2.12}$$

Substitution of Eq.(2.7) into Eq.(2.12) gives the estimate

$$\hat{V} = \frac{1}{16\rho_o c^2} E\left\{\left[p_1(r_1, t) + p_2(r_2, t)\right]\left[p_1(r_1, t) + p_2(r_2, t)\right]\right\} \quad . \tag{2.13}$$

The kinetic energy density is defined as

$$T = \frac{\rho_o}{4} E\left\{\vec{u}\,(t)\, \vec{u}^{*}\,(t)\right\} \quad . \tag{2.14}$$

Substitution of Eq.(2.6) into Eq.(2.14) gives the estimate for the kinetic energy density

$$\hat{T} = \frac{1}{\omega^2 \rho_o \Delta r^2} \times$$

$$E\left\{\int\left[p_2(r_2, t) - p_1(r_1, t)\right] dt \int\left[p_2(r_2, t) - p_1(r_1, t)\right] dt\right\} \quad . \tag{2.15}$$

Elko[23] also developed the frequency domain estimation of both the potential and kinetic energy densities(see Appendix A). In the frequency domain, the spectrum of the potential energy density and kinetic energy density can be estimated by

$$\hat{V}(\omega) = \frac{1}{16\rho_o c^2}\left\{S_{p_1p_1}(\omega) + S_{p_2p_2}(\omega) + 2\,Re\left[S_{p_1p_2}(\omega)\right]\right\} \qquad (2.16)$$

and

$$\hat{T}(\omega) = \frac{1}{\omega^2\rho_o(\Delta r)^2}\left\{S_{p_1p_1}(\omega) + S_{p_2p_2}(\omega) - 2\,Re\left[S_{p_1p_2}(\omega)\right]\right\} \ . \qquad (2.17)$$

The derivation of the specific acoustic impedance estimator is a little different in that it is derived in terms of the spectral intensities and energies. Specific acoustic impedance at r is defined as the ratio of acoustic pressure, $p(r, \omega)$, to acoustic particle velocity, $\vec{u}(r, \omega)$,

$$\vec{Z}(\omega) = \frac{P(\omega)}{\vec{U}(\omega)} \qquad (2.18)$$

where $\vec{U}(\omega) = \vec{U}_a(\omega) + j\,\vec{U}_r(\omega)$ is the complex valued magnitude of the velocity and $P(\omega)$ is the real valued magnitude of the pressure. This expression assumes that both the velocity and the pressure have the same $\exp(j\omega t)$ time dependence. $\vec{U}_a(\omega)$ is the real or active part of the particle velocity that is in phase with the pressure and $\vec{U}_r(\omega)$ is the imaginary or reactive part that is 90° out of phase with the pressure. The impedance can now be written in terms of the pressure and particle velocity spectra

$$\bar{Z}(\omega) = \frac{P(\omega)}{\vec{U}_a(\omega) + j\,\vec{U}_r(\omega)} \quad . \tag{2.19}$$

By multiplying both the numerator and the denominator by the complex conjugate of $\vec{U}(\omega)$, the impedance becomes

$$\bar{Z}(\omega) = \frac{P(\omega)\,\vec{U}_a(\omega)}{|\vec{U}(\omega)|^2} - j\,\frac{P(\omega)\,\vec{U}_r(\omega)}{|\vec{U}(\omega)|^2} = \frac{\vec{I}(\omega) - j\,\vec{Q}(\omega)}{\frac{2\,T(\omega)}{\rho_o}} \quad . \tag{2.20}$$

The numerators of the real and imaginary parts of the impedance are proportional to the real and imaginary intensities and the denominator is proportional to the kinetic energy. Algebraic manipulation of Eq.(2.20) leads to estimators for the real and imaginary components of the specific acoustic impedance, $R(\omega)$ and $X(\omega)$ respectively, in terms of the acoustic intensities and the kinetic energy. The specific acoustic impedance is given as

$$\bar{Z}(\omega) = R(\omega) + j\,X(\omega) \tag{2.21}$$

where the specific acoustic resistance is

$$R(\omega) = \frac{\rho_o}{2}\frac{\vec{I}(\omega)}{T(\omega)} \tag{2.22}$$

and the specific acoustic reactance is

$$X(\omega) = -\frac{\rho_o}{2}\frac{\vec{Q}(\omega)}{T(\omega)} \quad . \tag{2.23}$$

In terms of the autospectra and cross-spectrum, these quantities can be estimated as

$$\hat{R}(\omega) = \frac{\rho_o}{2}\frac{\vec{I}(\omega)}{\hat{T}(\omega)} = 2\omega\rho_o\Delta r\frac{Im\left[S_{p_1p_2}(\omega)\right]}{S_{p_1p_1}(\omega) + S_{p_2p_2}(\omega) - 2Re\left[S_{p_1p_2}(\omega)\right]} \tag{2.24}$$

and

$$\hat{X}(\omega) = -\frac{\rho_o}{2}\frac{\vec{Q}(\omega)}{\hat{T}(\omega)} = -\omega\rho_o\Delta r\frac{S_{p_2p_2}(\omega) - S_{p_1p_1}(\omega)}{S_{p_1p_1}(\omega) + S_{p_2p_2}(\omega) - 2Re\left[S_{p_1p_2}(\omega)\right]} \tag{2.25}$$

These expressions can easily be implemented either in the form of Eq.(2.22) and Eq.(2.23) or Eq.(2.24) and Eq.(2.25).

2.3. Errors

The errors involved in the estimation of the acoustic intensity, energy density, and impedance can be divided into two subsets: bias errors and random errors. Bias errors are systematic errors in that they represent deviations of the expected values of the estimation to the true exact values. Random errors represent mean square fluctuations of the estimators around the expected value.

2.3.1. Bias Errors: Finite Sum/Difference Approximations

The first source of bias errors to be discussed is the result of the finite difference and finite sum approximations made for the acoustic particle velocity and acoustic pressure. These errors are dependent on the complexity of the acoustic field. Thompson and Tree[24] have investigated these errors for various source configurations including monopole, dipole, and quadrupole sources. For a monopole source, the relative bias error for the active intensity is

$$\varepsilon_{b\vec{I}} = \frac{\vec{I}(\omega)}{\vec{I}(\omega)} = \frac{\sin(k\Delta r)}{k\Delta r} \frac{r^2}{r_1 r_2} \qquad (2.26)$$

where the distances r_1, r_2, r, and Δr were defined in Figure 2.1. For use in later plots, the following conversion is made of the quantity $r^2/r_1 r_2$

$$\frac{r^2}{r_1 r_2} = \frac{1}{1 - \left(\frac{\Delta r}{2r}\right)^2} \qquad (2.27)$$

The relative bias error due to the finite approximations for the reactive intensity resulting from a monopole source has been derived by Elko[23] and is

$$\varepsilon_{b\vec{Q}} = \frac{\vec{Q}(\omega)}{\vec{Q}(\omega)} = \left[\frac{r^2}{r_1 r_2}\right]^2 \quad . \qquad (2.28)$$

This error is not a function of the frequency, only of the distance between sensors and the distance from the sensor midpoint to the source.

For a monopole type source, the estimation bias error due to the finite approximations for the potential energy density estimator is

$$\varepsilon_{bV} = \frac{\hat{V}(\omega)}{V(\omega)} = \frac{r^2}{r_1 r_2}\left[\frac{r^2}{r_1 r_2} - \sin^2\left(\frac{k\Delta r}{2}\right)\right] \qquad (2.29)$$

and the kinetic energy density estimator bias error is

$$\varepsilon_{bT} = \frac{\hat{T}(\omega)}{T(\omega)} = \left(\frac{r^2}{r_1 r_2}\right)^2 \left[\frac{1}{1 + (k\Delta r)^2}\right]\left[1 + \frac{k^2 r_1 r_2 \sin^2(k\Delta r/2)}{(k\Delta r/2)^2}\right] \quad ..(2.30)$$

Figures 2.2 and 2.3 show the estimation bias errors for the active and reactive intensities and the potential and kinetic energies. It is evident from these figures that the estimation bias errors can be minimized by keeping the parameters $k\Delta r$ and $\Delta r/r$ small. Thompson and Tree[24] define limits for these parameter using the bias errors due to a quadrupole source as a worst case. These

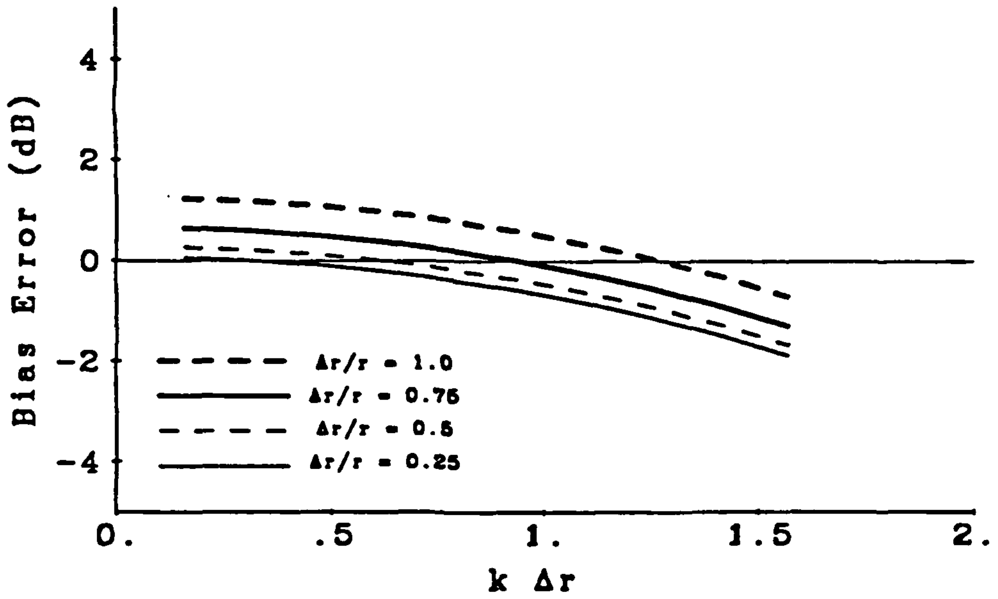

(a) Active intensity, $\varepsilon_{b\vec{I}}$

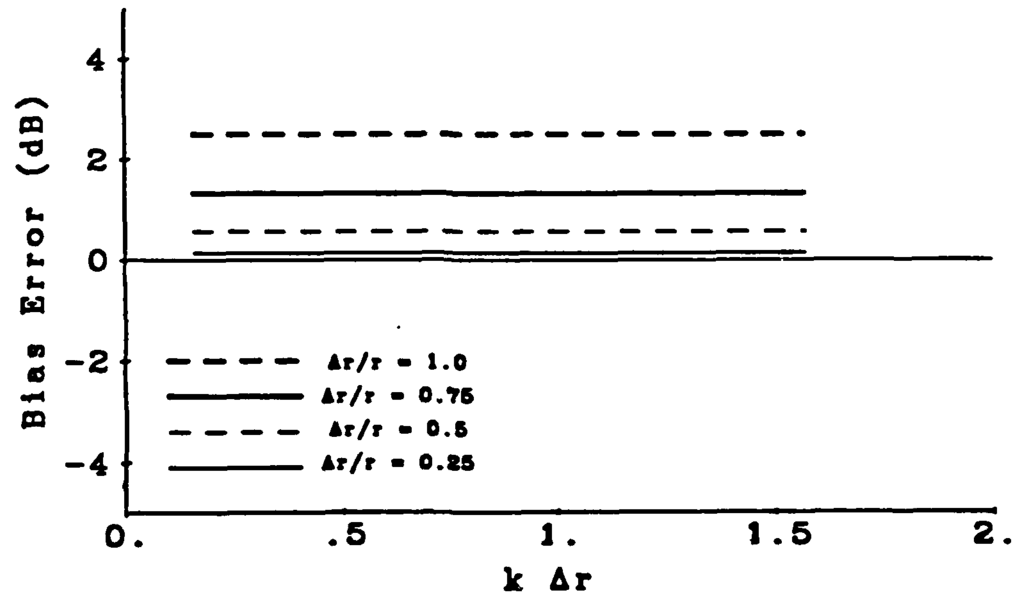

(b) Reactive intensity, $\varepsilon_{b\vec{Q}}$

Figure 2.2. Finite difference approximation bias error for a monopole source.

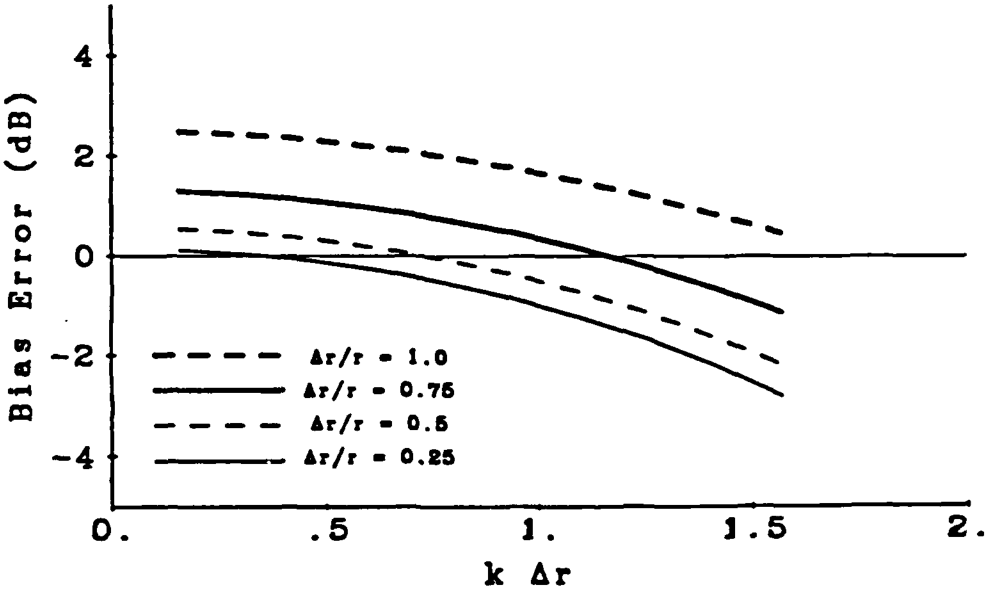

(a) Potential Energy, ε_{bV}

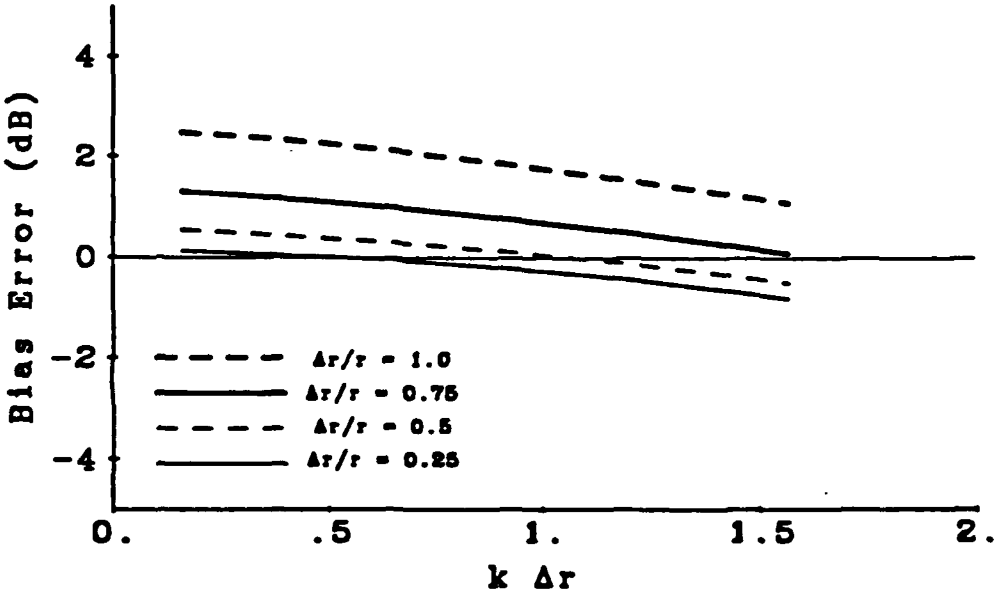

(b) Kinetic Energy, ε_{bT}

Figure 2.3. Finite difference approximation bias error for a monopole source.

parameter limits are given as $k\Delta r < 1.3$ and $\Delta r/r < 0.5$ for an inaccuracy less than 1.5 dB.

It is a simple matter to derive the estimation bias error for the impedance estimators in terms of the estimation bias errors for the acoustic intensity and energy density estimators. Beginning with the exact value for the real part of the specific acoustic resistance (see Eq. (2.22))

$$R = \frac{\rho_o}{2}\frac{\vec{I}}{T} \tag{2.31}$$

and the estimated value for the specific acoustic resistance

$$\hat{R} = \frac{\rho_o}{2}\frac{\hat{\vec{I}}}{\hat{T}} \tag{2.32}$$

we can develop the estimation bias error as

$$\varepsilon_{bR} = \frac{\hat{R}(\omega)}{R(\omega)} = \frac{\left(\vec{I}/\vec{I}\right)}{\left(\hat{T}/T\right)} = \frac{\varepsilon_{b\vec{I}}}{\varepsilon_{bT}} \quad . \tag{2.33}$$

This error can be recognized as the ratio of the active intensity bias error to the kinetic energy bias error. The bias error for the imaginary part of the specific acoustic impedance is derived to be the ratio of the reactive intensity bias error to the kinetic energy bias error

$$\varepsilon_{bX} = \frac{\hat{X}(\omega)}{X(\omega)} = \frac{\left(\vec{Q}/\vec{Q}\right)}{\left(\hat{T}/T\right)} = \frac{\varepsilon_{b\vec{Q}}}{\varepsilon_{bT}} \quad . \tag{2.34}$$

Figure 2.4 shows the bias errors for the real and imaginary parts of the impedance for a monopole source.

It is evident from this figure that the impedance bias errors can also be minimized by assuring that both the parameters kΔr and Δr/r are kept small. This requirement is the same as the requirement to keep the acoustic intensity and energy density bias errors small.

2.3.2. Bias Errors: Instrumentation Phase/Magnitude Mismatch.

Another source of estimation bias errors is due to sensor and instrumentation phase and magnitude mismatch between the two measurement channels. This error for the active intensity is given by Elko[23] as

$$\eta_{bI} = \frac{\hat{I}(\omega) - I(\omega)}{I(\omega)} \approx \frac{\sin(\Delta\phi)\, Re\left[S_{p_1p_2}(\omega)\right]}{Im\left[S_{p_1p_2}(\omega)\right]} \tag{2.35}$$

where $\Delta\phi$ is the instrumentation phase mismatch which accounts for all elements in the data acquisition system, including the two probe hydrophones and the electronics. This bias error is function only of the phase error between the two acoustic pressure sensors and of the acoustic field.

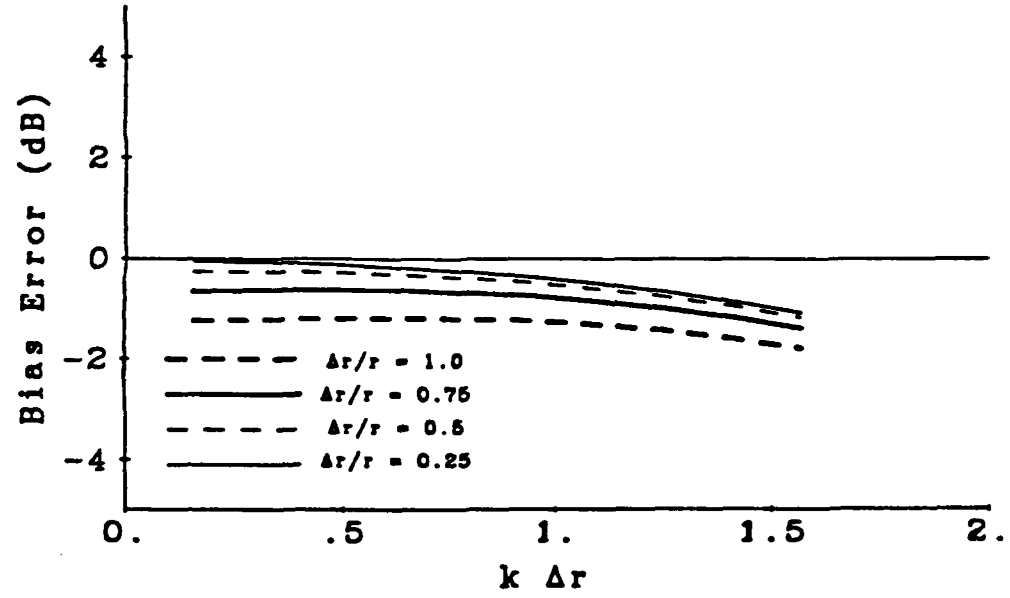

(a) Specific Acoustic Resistance, ε_{bR}

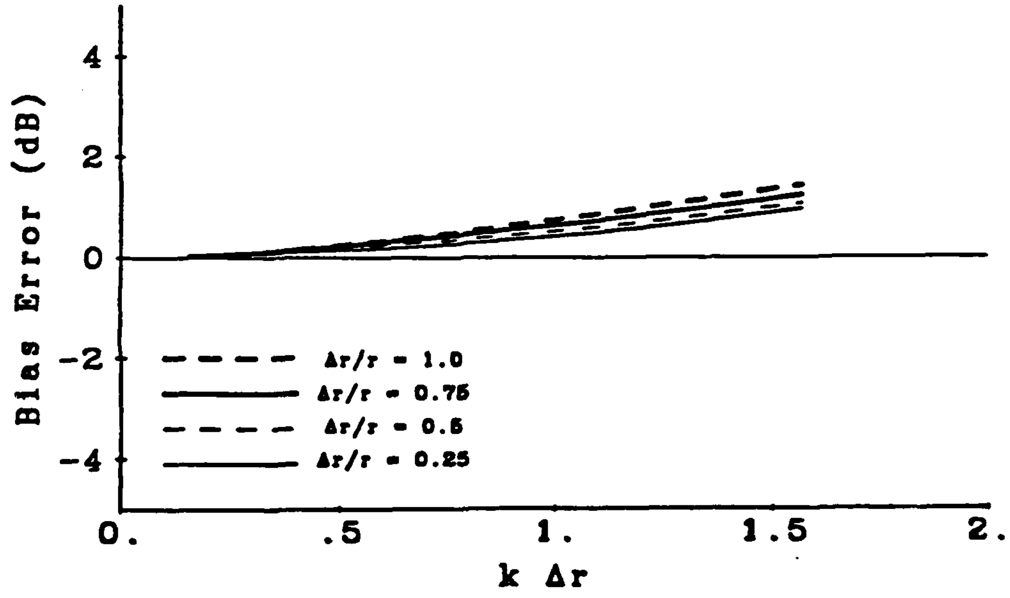

(b) Specific Acoustic Reactance, ε_{bX}

Figure 2.4. Finite difference approximation bias error for a monopole source.

The bias error for the reactive intensity estimator is given as

$$\eta_{bQ} = \frac{\hat{Q}(\omega) - Q(\omega)}{Q(\omega)} \approx \frac{\delta(\omega)}{e(\omega)} \tag{2.36}$$

where $\delta(\omega)$ is the magnitude mismatch within the hydrophones and electronics and $e(\omega)$ is the field amplitude difference. The field amplitude difference is the actual magnitude difference of the acoustic field between the two sensors. It is apparent from Eq.(2.36) that this bias error is not a function of the instrumentation and sensor phase mismatch but only of the magnitude mismatch between the two channels.

The bias errors for the potential and kinetic energies are given as

$$\eta_{bV} = \frac{\hat{V}(\omega) - V(\omega)}{V(\omega)} \approx \frac{2\,\sin(\Delta\phi)\, Im\left[S_{p_1p_2}(\omega)\right]}{S_{p_1p_1}(\omega) + S_{p_2p_2}(\omega) + 2\,Re\left[S_{p_1p_2}(\omega)\right]} \tag{2.37}$$

and

$$\eta_{bT} = \frac{\hat{T}(\omega) - T(\omega)}{T(\omega)} \approx \frac{\sin(\Delta\phi)\, Im\left[S_{p_1p_2}(\omega)\right]}{S_{p_1p_1}(\omega) + S_{p_2p_2}(\omega) - 2\,Re\left[S_{p_1p_2}(\omega)\right]}\ . \tag{2.38}$$

Both of these error expressions were derived assuming that only phase mismatches were present.

The normalized bias error for the real and imaginary impedances will now be derived in terms of the intensity and energy bias errors. The normalized bias error for the specific acoustic resistance is defined as

$$\eta_{bR} = \frac{\hat{R}(\omega) - R(\omega)}{R(\omega)} \quad . \tag{2.39}$$

Algebraic manipulation of Eq.(2.39) leads to the normalized bias error for the real part of the impedance, the specific acoustic resistance in terms of the intensity and energy bias errors. This error is approximated by

$$\eta_{bR} \approx \frac{\eta_{bI} - \eta_{bT}}{\eta_{bT} + 1} \tag{2.40}$$

The normalized bias error for the imaginary part of the impedance, the specific acoustic reactance, can similarly be derived as

$$\eta_{bX} = \frac{\hat{X}(\omega) - X(\omega)}{X(\omega)} \approx \frac{\eta_{bQ} - \eta_{bT}}{\eta_{bT} + 1} \quad . \tag{2.41}$$

It is apparent from Eq.(2.40) and Eq.(2.41) that, since both the intensity bias errors, η_{bI} and η_{bQ}, and the kinetic energy bias error, η_{bT}, are functions of the phase mismatch, the bias errors for the impedances will also be a function of the phase mismatch. For this experiment, it was assumed that the bias errors for the impedances were much the same as those for the active intensity so the active intensity was used as a guide line .

2.3.3. Combined Effects of Bias Errors

At low frequencies, the phase mismatch is a limitation to the accuracy of the system. The limitation is at low frequencies because the actual field phase difference between two closely spaced points can be very small. Therefore, a small electronic phase mismatch can overwhelm the actual field phase difference. Because of the phase mismatch limitation, it is necessary to calibrate the system to account for the phase mismatch between the sensor and channel electronics.

2.3.4. Calibration Technique

The technique employed for this experiment uses the fact that for a general stationary acoustic field (one which is stationary with time), the difference between the transfer function of a sensor pair and that of the same pair when the sensors are exchanged in position is simply related to the differences between the two sensors and not the acoustic field. This method is convenient because few restraints are made on the acoustic field, only that it is stationary during the calibration procedure and that the reactive field does not dominate the acoustic field. The first restraint is met by assuring that nothing in the tank is moved and that the signal to the transmitting hydrophone remains constant. The second restraint implies that the calibration is not performed in the very near field of the transmitting hydrophone. Other methods, such as the plane-wave tube method and the electrostatic actuator method, which are commonly used with the in-air intensity system calibration techniques, are not easily applied to our test set-up.

The modified switching technique that was employed involves measuring the cross-spectrum between the two channels with the sensors in an initial position and with the sensors switched in position. A diagram of the initial and switched sensor positions is given in Figure 2.5.

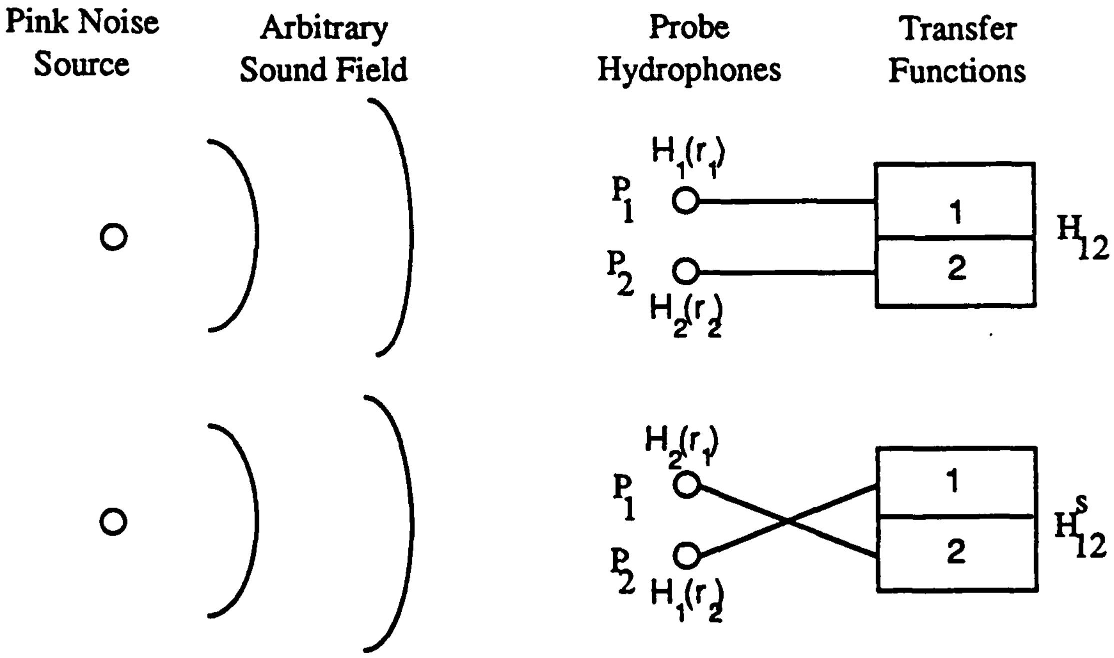

Figure 2.5. Sensor phase mismatch calibration diagram.

The calibrated cross-spectrum is calculated from the following relationships

$$\left[G_{12}\right]_{calibrated} = \frac{\left[G_{12}\right]_{measured}}{K_{12}\left|H_1\right|^2} \tag{2.42}$$

where

$$K_{12}(\omega) = \sqrt{\frac{H_{12}(r, \omega)}{H^s_{12}(r, \omega)}} \tag{2.43}$$

The initial transfer function between the two measurement channels is

$$H_{12}(r, \omega) = \frac{H_2(r_2, \omega)}{H_1(r_1, \omega)} \tag{2.44}$$

and the switched transfer function between the measurement channels is

$$H^s_{12}(r, \omega) = \frac{H_2(r_1, \omega)}{H_1(r_2, \omega)} \tag{2.45}$$

If the magnitude errors between the measurement channels are neglected, i.e. calibrated to minimize the magnitude mismatches, the phase error between the measurement channels can be calculated from

$$\phi_{12}(\omega) = \frac{1}{2} \tan^{-1} \left[\frac{Im\left[G^*_{12}/G^s_{12}\right]_{\text{measured}}}{Re\left[G^*_{12}/G^s_{12}\right]_{\text{measured}}} \right] \tag{2.46}$$

where the superscript s denotes the switched spectrum.

Calibration measurements indicate that the phase mismatch between the hydrophone pair used in this research is approximately linear. This result is similar to results found with microphones. A program developed for the intensity system calculates a least-squares fit to the phase mismatch. The slope and zero crossing of this least squares line leads to a time delay between the two channels. All future cross-spectra can be corrected for phase mismatch by using this time delay. Figure 2.6 shows the phase mismatch as a function of frequency. Although the least-squares approximation differs from the measured data slightly at some frequencies, this error was small compared to the field phase differences which were measured.

In the error derivations given in this chapter, magnitude errors could generally be assumed small. This assumption could be made since the gain on the Ithaco amplifiers were adjusted to give the same output for each hydrophone when the hydrophones were placed in the same sound field. This calibration was accomplished by placing one hydrophone into a sound field and storing the wave form on a digital oscilloscope. The second hydrophone was then placed in the same position and in the same sound field. Differences in the

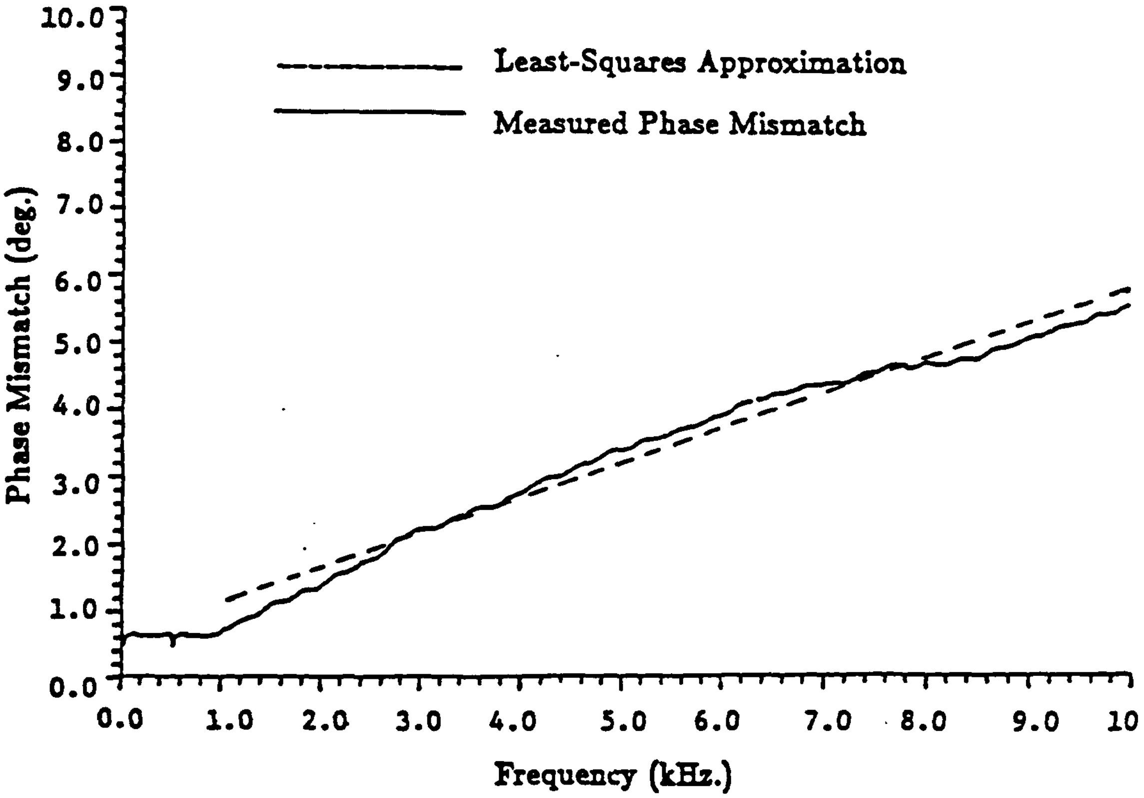

Figure 2.6. Sensor phase mismatch calibration curves.

amplitudes between the two wave forms could then be detected on the same oscilloscope. The amplifiers were then set so that the level of the second was equal to the level of the first. This magnitude calibration procedure was performed at each individual frequency of interest.

2.3.5. Random Errors

The last source of errors to be discussed is the random errors. Random errors can be caused by using finite sample length estimation for random processes that are defined in a stationary ergodic sense. These errors were found to be inversely proportional to the square root of the number of uncorrelated ensemble averages. Therefore, by increasing the number of ensemble averages, the random errors associated with finite sample lengths can be minimized.

Another source of random errors is due to sample quantization noise in both the A/D converters and in the computational roundoff noise in the FFT processing of the data. Quantization noise is due to the finite step size intervals in the A/D conversion. It was found that these errors could be minimized by amplifying the input signals so that the full range of the A/D converters could be used without overload.

Chapter 3

THE PARAMETRIC ARRAY

3.1. Introduction

The projector of acoustic energy used in this study was a nonlinear parametric array. This type of projector is able to produce much narrower beam patterns at low frequencies than conventional projectors. The narrow beam pattern is desirable in this experiment because of the small dimensions of the anechoic water tank. The narrow beamwidth also permits the use of small sample sizes with minimal edge effects.

The parametric array is formed in one of two ways. One way involves simultaneously radiating two acoustic signals having frequencies ω_1 and ω_2 from a single source. The other way uses a amplitude modulated signal composed of a high frequency carrier ω_0 that is amplitude modulated by the desired low frequency ω_Δ. When the amplitudes of the two primary signals (or the carrier signal) are high enough, then the nonlinearities of the medium will create sum and difference frequency components. The sum frequency, ω_+, equals $\omega_1 + \omega_2$ and the difference frequency, ω_Δ equals $\omega_2 - \omega_1$. The second of these two components, the difference frequency component, is the one of most interest. Since high frequency energy is attenuated at a greater rate than low frequency energy, the low frequency signal will propagate farther than the high frequency signals. The most important consequence of generating the difference frequency component as described is that the directivity pattern of the difference frequency component is roughly equal to that of the primaries.

3.2. Theory

Theoretical formulations concerning the parametric array began in 1963 with Westervelt[17]. In his paper, Westervelt investigated the difference frequency field resulting from the nonlinear interaction of two perfectly collimated plane finite amplitude waves of different frequencies propagating in the same direction. He derived expressions for the sound pressure in the far field of a parametric array and an expression of the 3 dB beamwidth of the array.

Much of the work since Westervelt has concerned the far field performance of the parametric array. Owing to the small dimensions of the water tank, however, we are more concerned with the near field behavior. Fenlon[22], has derived an expression which gives a simple closed-form solution for the difference frequency field along the parametric array axis in both the near field and far field. These expressions were used as the theoretical base with which to compare the experimental results.

Fenlon breaks up the parametric array's axis into the near field and far field. A point is considered in the near field if $\alpha_0 r < 1$ dB where α_0 is the absorption coefficient in dB per meter at the carrier frequency ω_0 and r is the distance to the field point. If $\alpha_0 r > 1$ dB, then the point is in the far field. Using this constraint, the near field to far field transition is at the distance $r_T = 1/\alpha_0$. Fenlon also has two categories depending on whether or not the viscous absorption is sufficient to confine all finite amplitude interaction within the mean primary wave matching distance, $L_* = r_0\omega_0/\omega_\Delta$ where r_0 is the Rayliegh distance defined as $r_0 = A/\lambda_0$. A is the active area of the piston. There are, therefore, four ranges that could be used to describe the parametric array. All four cases are given as variations on a single expression. This expression gives the peak sound pressure level on the axis of the array in terms of various parameters. The sound pressure level at the difference frequency and at the range, r, is given by

$$SPL_\Delta(r) = SL_1 + SL_2 + 20\log_{10}\left[f_\Delta(\mathrm{kHz})\right] + 10\log_{10}\left|\Phi(r)\right| - \alpha_\Delta r - 290 \text{ dB re } 1\mu\mathrm{Pa} \qquad (3.1)$$

where SL_1 and SL_2 are the source levels of the primary components. The variation on this expression comes in the term $\Phi(r)$. Starting with the case when the finite amplitude interaction is not limited to the mean primary wave matching distance, that is when $\alpha_0 L_* \ll 1$ dB, the expression for $\Phi(r)$ is

$$\Phi(r) = \frac{\left\{\left[\alpha_0 r - \frac{1}{2}\ln\left\{\frac{\left(1 + 4r^2/r_0^2\right)^2}{1 + \left(4r/k_\Delta r_0\right)^2}\right\}\right]^2 + \left[\tan^{-1}\left(4r/k_\Delta r_0\right)\right]^2\right\}}{L_*^2 + r^2} \qquad (3.2)$$

when in the near field (i.e. $\alpha_0 r < 1$ dB) and

$$\Phi(r) \rightarrow \frac{\left|E_1\left(-i\alpha_0 L_*\right)\right|}{r} \tag{3.3}$$

when in the far field (ie. $\alpha_0 r > 1$ dB). When the finite amplitude interaction is limited to the mean primary matching distance or when $\alpha_0 L_* \gg 1$ dB, the expression for $\Phi(r)$ becomes

$$\Phi(r) \cong \frac{\left(k_\Delta/\alpha_0 r_0\right)\left\{\left[1 - \frac{e^{-\alpha_0 r}}{1 + 4r^2/r_0}\right]^2 + \left[\left(\frac{4r/k_\Delta r_0}{1 + 4r^2/r_0^2}\right) e^{-\alpha_0 r}\right]^2\right\}}{\left(k_\Delta r_0/4\right)^2 + r^2} \tag{3.4}$$

when in the near field and

$$\Phi(r) \rightarrow \frac{1}{\alpha_0 r} \tag{3.5}$$

when in the far field.

By knowing the values of α_0, L_* and r, we can choose the correct expression for $\Phi(r)$. These quantities are calculated from the parameters of the system. In order to calculate the absorption coefficient, α_0, we need to know the center or carrier frequency of the projector. The projector used in this experiment was a Lowrance Model TTH-2192-8 transducer. This transducer has a resonance frequency of 192.0 kHz. Preliminary experiments working at the resonance frequency indicated that the power amplifier that we had available was not able to drive the projector at sufficiently high power to obtain the desired nonlinear behavior at this frequency. By scanning through the frequency range from 100 kHz to 300 kHz, it was found that the actual output of the amplitude-transducer combination was maximized at 131 kHz. This frequency was therefore used as the center frequency for the rest of the measurements.

Using the center frequency, 131 kHz, we are able to calculate the quantities needed to define the acoustic field on the axis of the parametric array. The first quantity to be calculated is the absorption coefficient. This quantity can be calculated from[25]

$$\alpha_o = \frac{4.34}{\rho_o c^3}\left(\frac{4\mu_F}{3} + \mu_F'\right)\omega_o^2 \quad . \tag{3.6}$$

The absorption coefficient is $4.27(10^{-3})$ dB/m. The matching distance, $L_* = r_o\omega_o/\omega_\Delta$ is calculated for a difference frequency of 10 kHz. This distance is 2.3 m. Multiplying these two quantities together chooses two of the four expressions for $\Phi(r)$. The product of L_* and α_o is $9.8(10^{-3})$ dB $\ll$ 1 dB. This result narrows the choice down to Eq.(3.2) or Eq.(3.3). The choice between these two expressions is determined by the location of the field point. The division between near field and far field is made based on the quantity $\alpha_o r$. In this case, the size of the anechoic water tank limits the value of r to less than 3 m. This makes the quantity, $\alpha_0 r < 0.03$ dB < 1 dB. With this final constraint, the expression for $\Phi(r)$ for the system used in this experiment is given by Eq.(3.2).

The main advantage of using a parametric array as a source of acoustic energy is the narrow beamwidths obtained at low frequencies. The theory by which we will compare the experimental results is from Muir and Blue[26]. The normalized angular dependence of the sound pressure at the difference frequency can be written as

$$C(\theta) = \frac{P_\Delta\left(r,\,\theta\right)}{P_\Delta\left(r,\,0\right)} = \left[\frac{\alpha^2}{\alpha^2 + k_\Delta{}^2\,\sin^4(\theta/2)}\right]^{1/2} \tag{3.7}$$

where k_Δ is the difference frequency wave number. An interesting aspect of this directivity pattern is the absence of side lobes. Further modification of this expression by Naze and Tjötta[27] accounts for the finite aperture of the primary beam for circular transducers

$$D(\theta) = C(\theta)\left|\frac{2\,J_1\left(k_\Delta a\,\sin(\theta)\right)}{k_\Delta a\,\sin(\theta)}\right| \tag{3.8}$$

where A is the radius of the active portion of the transducer. A comparison of these expressions for a difference frequency of 10 kHz is given in Figure 3.1.

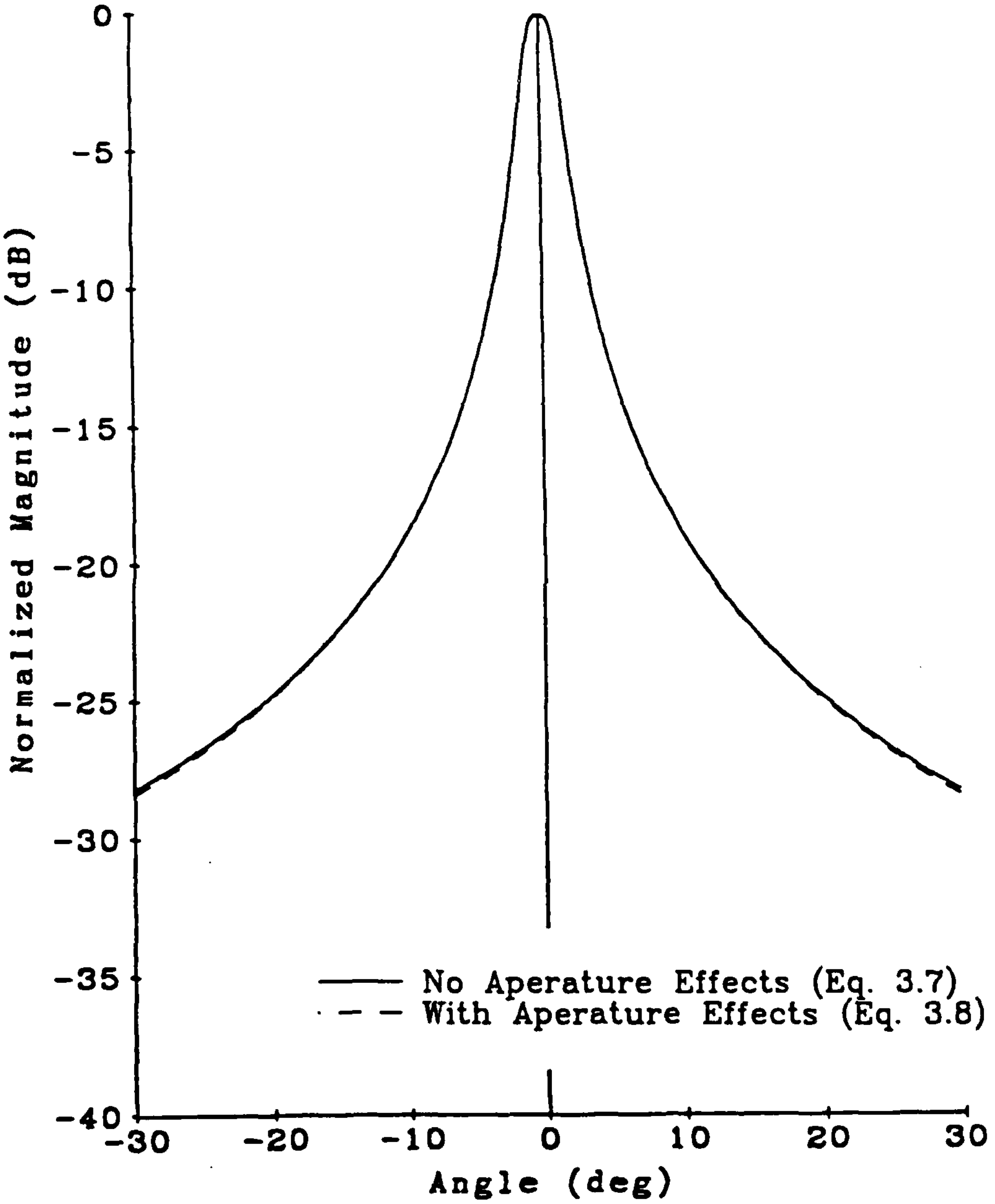

Figure 3.1. Comparison of theoretical beam patterns with and without inclusion of finite aperture effects.

3.3. Experimental Results

Experiments performed on the parametric array to verify its operation included on-axis sound pressure and intensity levels, and beam patterns. An intensity scan of the field produced by the parametric array was also completed.

3.3.1. On-Axis Sound Pressure Level

The first experiments done on the parametric source were to measure the on-axis sound pressure level and intensity level. The experimental procedure consisted of manually moving the positioning trolley, with the hydrophones attached, at locations along the axis of the array. The parametric array was positioned at one end of the tank. Figure 3.2 shows the set-up and dimensions in the tank.

Measurement of the on-axis response began with the measurement of the response at the 131 kHz center frequency. Since the intensity measurement system has a maximum frequency of 10 kHz, set by the maximum frequency for the anti-aliasing filters, the intensity level at 131 kHz could not be measured. The sound pressure level could, however, be measured using a rms volt meter. Figure 3.3 shows the on-axis sound pressure at 131 kHz as a function of distance. This figure was obtained using a continuous signal and compares two sets of measurements made under identical conditions. Although the general trend of the sound pressure level follows the theoretical -3 dB per doubling of distance dependence, there is a slight spatial periodic variation about the theoretical curve.

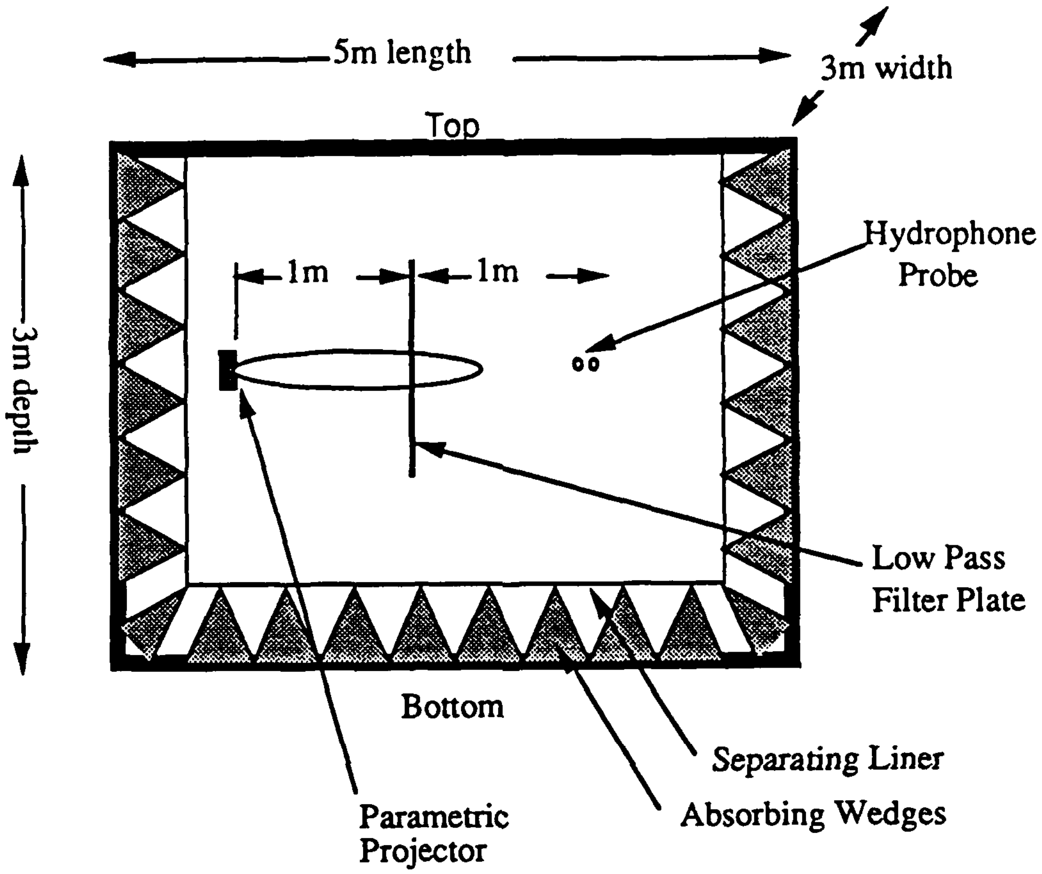

Figure 3.2. Water tank dimensions and set-up.

Experiments performed using short pulses of sound projected at 131 kHz lead to Figure 3.4. By using pulses, the slight spatial periodicity with distance disappears suggesting that the pattern was produced by reflections within the anechoic tank. Both measurements, with and without pulsing, indicate that the sound pressure level at 131 kHz does in fact follow the theoretical spherical spreading curve. The levels produced at the 131 kHz carrier signal frequency is above 180 dB and is therefore above the level where the nonlinear phenomena occur.

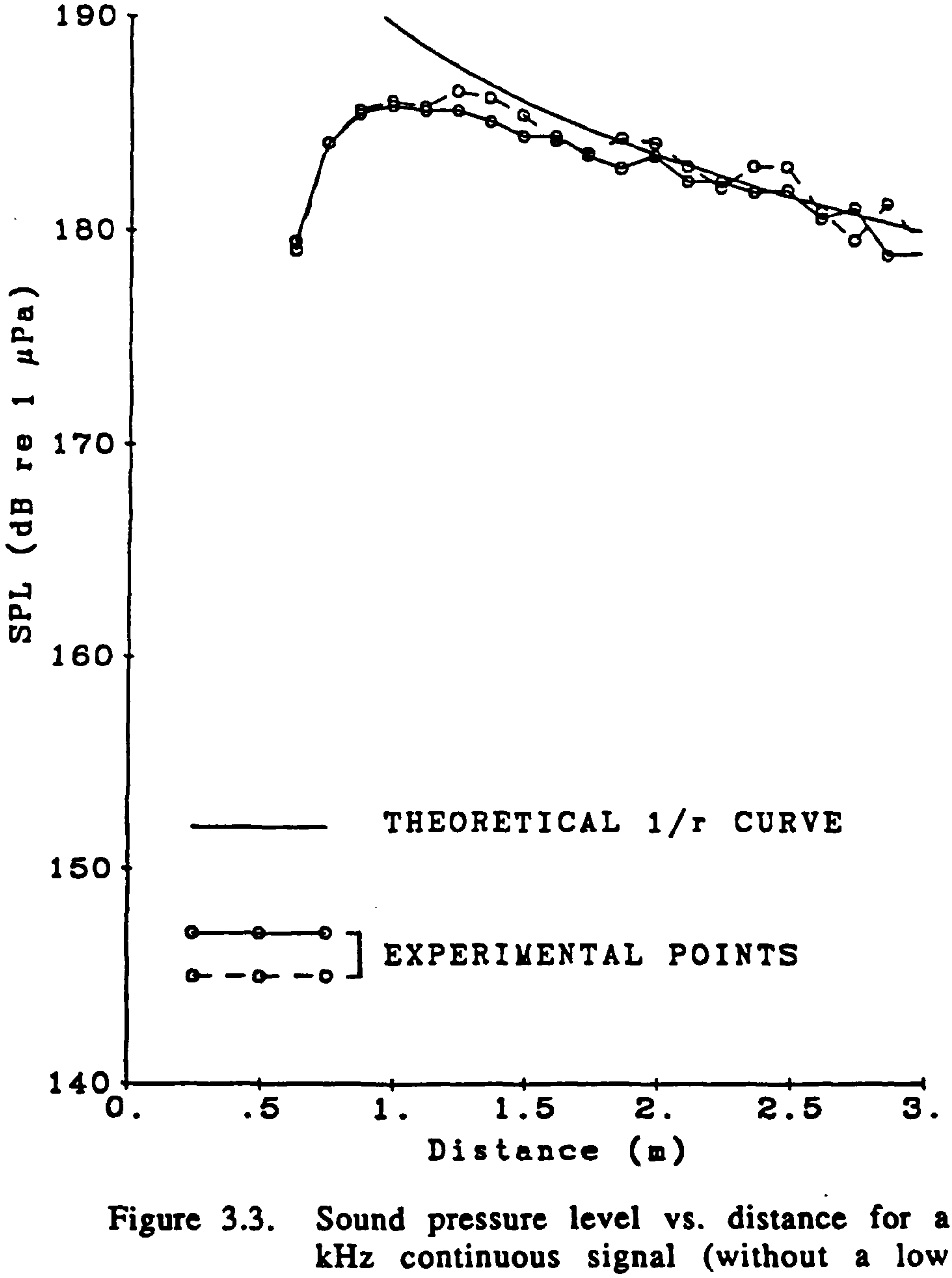

Figure 3.3. Sound pressure level vs. distance for a 131 kHz continuous signal (without a low-pass filter plate).

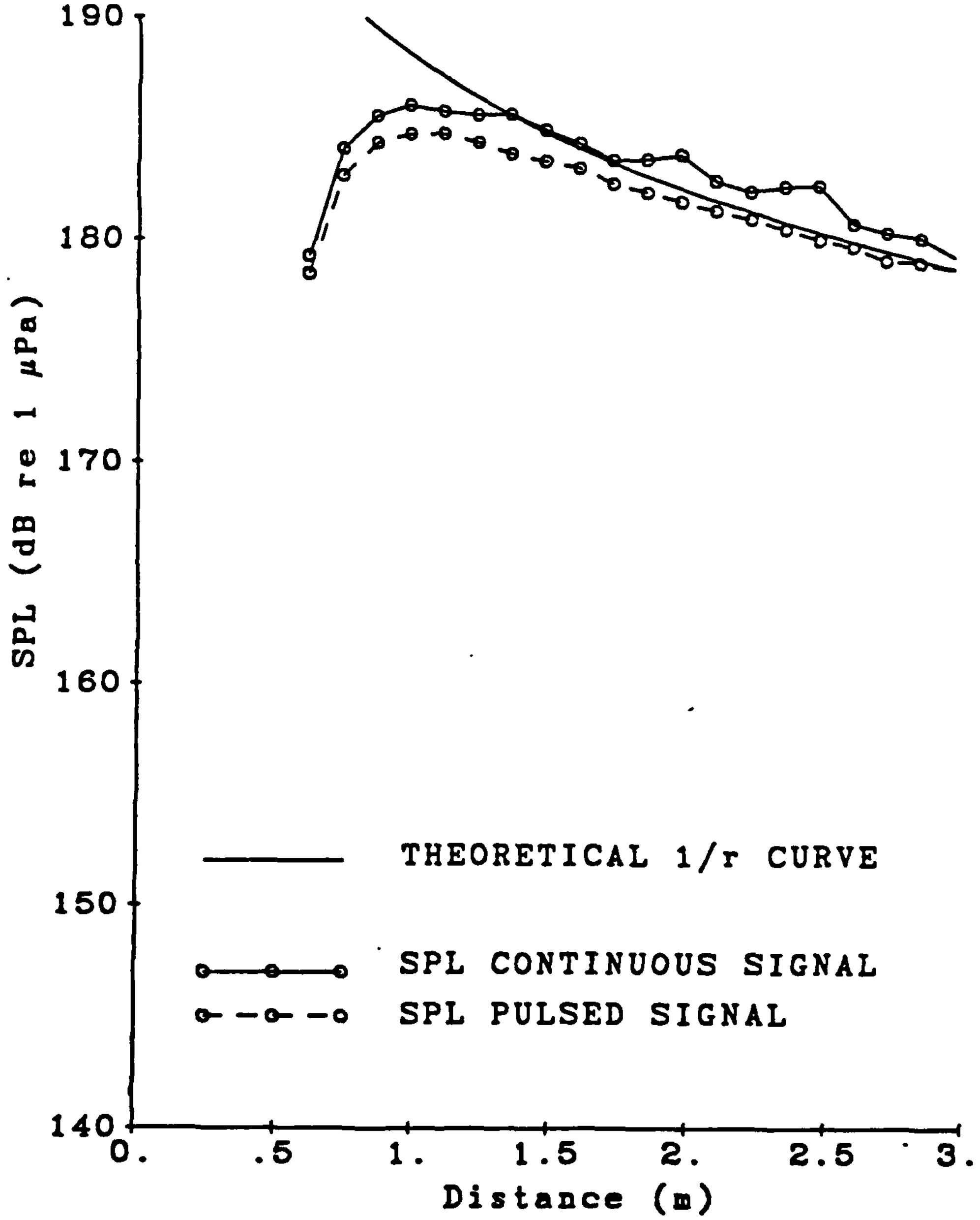

Figure 3.4. Sound pressure level vs. distance for a 131 kHz continuous and pulsed signal (without a low-pass filter plate).

The next experiments were performed to determine the effect of the low-pass filter plate. The low-pass filter plate is a thin aluminum plate placed between the parametric array and the sample plate. The purpose of the plate is to attenuate the high frequency carrier signal before it reaches the sample and intensity hydrophone probe. This helps to reduce the nonlinear effects in the actual receive hydrophones and electronics. The sound pressure level measurements with and without using the filter panel, made using a continuous signal are presented in Figure 3.5. The plot of the sound pressure level vs. distance with the filter plate shows wide fluctuations in level that are attributed to the diffraction about the edge of the filter panel since standing wave patterns along the axis produced smaller fluctuations. The curve does however show the lower levels obtained with the filter plate. Figure 3.6 shows the sound pressure level with and without the filter plate when done with a pulsed signal. A comparison of Figures 3.5 and 3.6 shows that by using pulses instead of continuous sound, the sound pressure level with the filter plate is actually smooth and falls off with the 3 dB per doubling of distance dependence. More importantly, these results show that the filter plate attenuates the 131 kHz carrier signal by 15 dB. This agrees with the theoretical attenuation for an infinitely large thin plate in which edge diffraction is not of concern.

Fenlon[22] expression, Eq.(3.1), indicates that the sound pressure level at the difference frequency is proportional to the difference frequency. This level is also proportional to the source

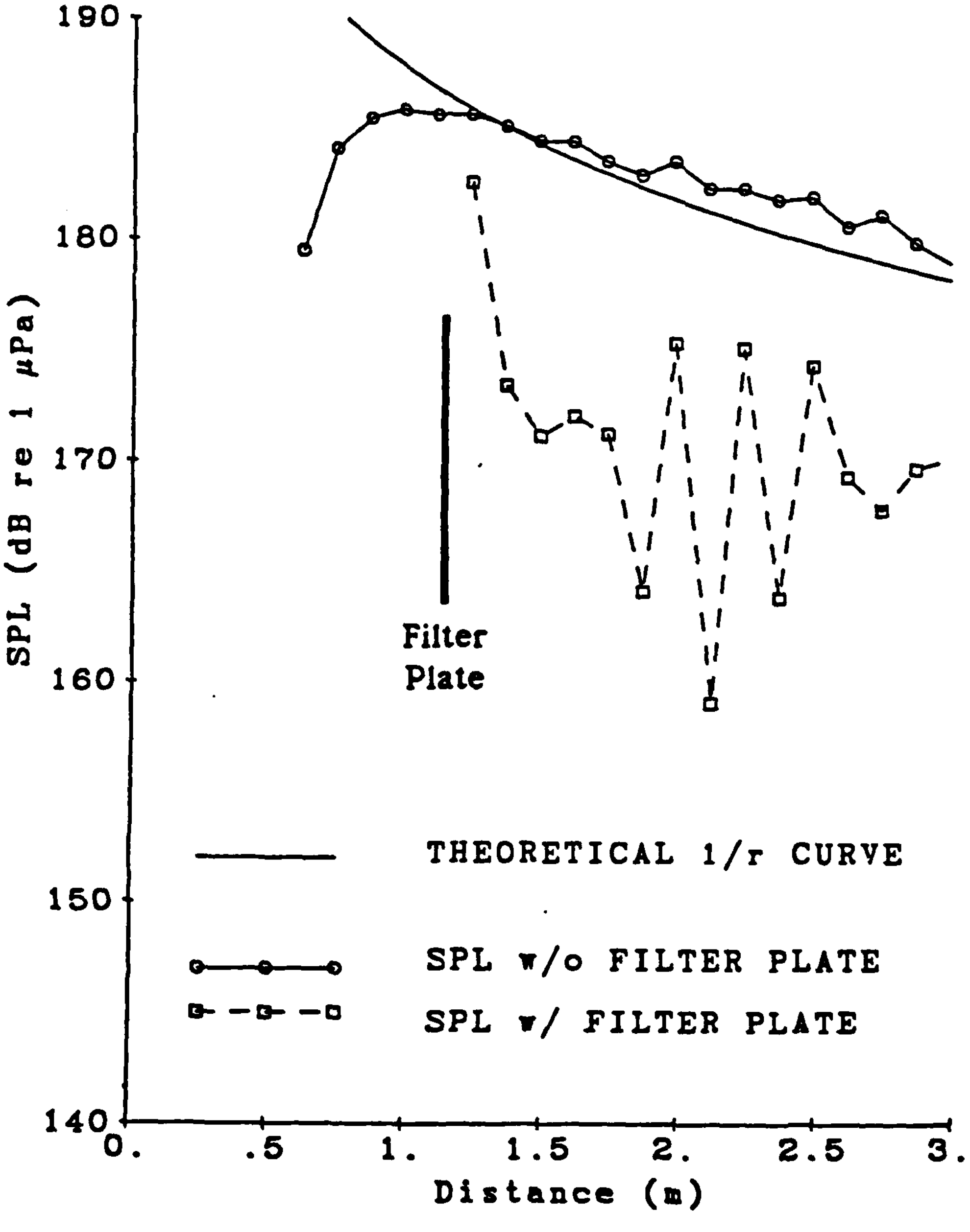

Figure 3.5. Sound pressure level vs. distance for a 131 kHz continuous signal (with and without a low-pass filter plate).

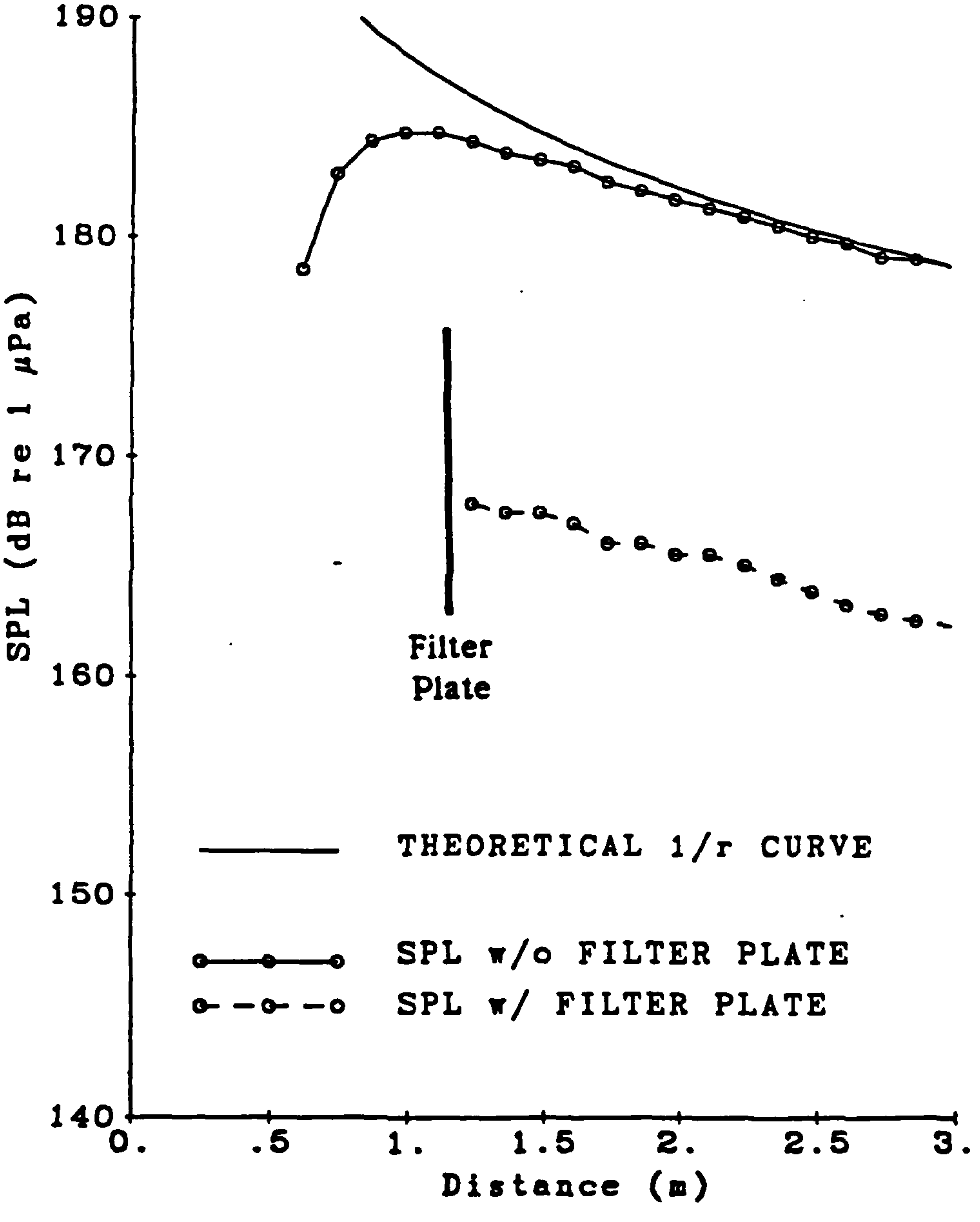

Figure 3.6. Sound pressure level vs. distance for a 131 kHz pulsed signal (with and without a low-pass filter plate).

level of the carrier signal. Therefore, higher difference frequency signal levels will be obtained by using higher difference frequencies and higher carrier signal levels. Since the carrier signal level is limited by the power amplifier, higher difference frequency signal levels are obtained by using higher difference frequencies. Since the A-D circuits in the intensity measurement system are limited to 10 kHz, this frequency, 10 kHz, was used as the difference frequency for the experiments. Measurements of the on-axis response at a 10 kHz difference frequency were performed to compare the theory with the experiment. Figure 3.7 gives a comparison of the on-axis response measured with a single hydrophone on the Spectral Dynamics spectrum analyzer and with the two hydrophone probe on the intensity system. These levels are comparable and follow Fenlon's theoretical curve for the parametric array. It should be noted that this theoretical curve does not follow the normal 20log(r) spherical spreading loss that would be obtained with a conventional linear source but actually falls off at a slower rate. This result is due to the continued difference frequency signal generation in the near field of the array. The difference frequency signal will approach the spherical spreading dependence in the far field of the array.

The effects of the low-pass filter plate on the 10 kHz difference frequency signal was studied next. The difference frequency level was measured with both the spectrum analyzer and with the intensity system. The measurements were performed with and without a bare 1/4 inch thick aluminum plate placed 1 m. in

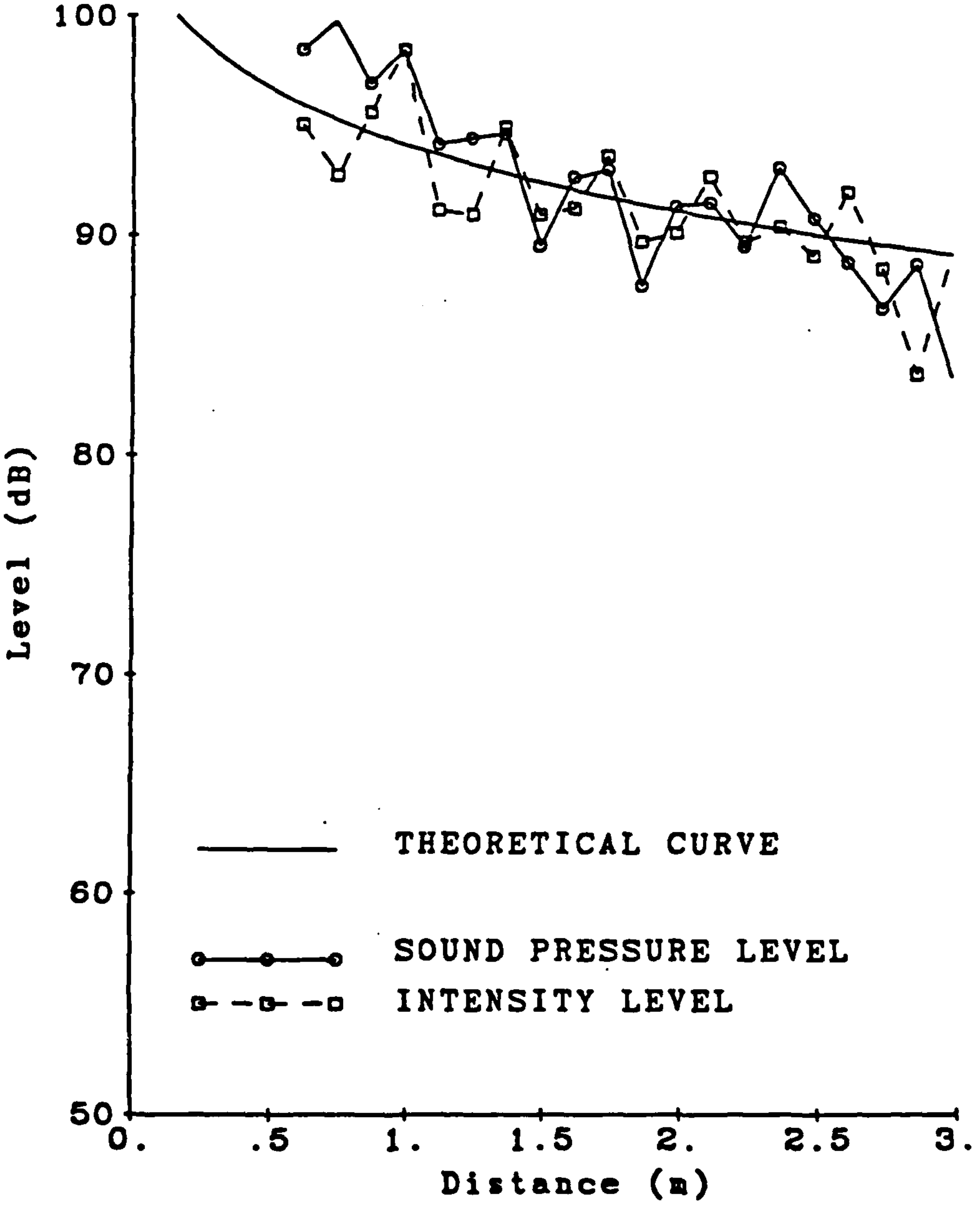

Figure 3.7. On-axis sound pressure level and intensity vs. distance for a 10 kHz continuous parametric signal (without a low-pass filter plate).

front of the transmitter. Figure 3.8 shows the on-axis response with and without the filter plate. The response with the filter plate follows the same dependence but is 2 to 3 dB below the response without the filter plate. This is consistent with theory which indicated a 2 dB a transmission loss for a 1/4 inch thick aluminum plate at 10 kHz. Figure 3.9 shows the intensity level as a function of distance. Again, the response with the filter plate is 2 to 3 dB below the response without the filter plate.

3.3.2. Beam Patterns

Measurement of the beam patterns produced by a parametric array was completed for a difference frequency of 10 kHz. The beam pattern was measured with and without the low-pass filter plate in front of the projector.

The set up for measuring the beam patterns consisted of the parametric array suspended from the positioning trolley in such a way that free rotation through 360° was possible. The two-sensor intensity probe was mounted at a location 2 m. from the source. For measurements made with the low-pass filter plate, the plate was located at a distance of 1 m. from the source but did not rotate with the test plates.

The directionality of the sound pressure level with and without the low-pass filter plate is given in Figure 3.10. For small angles, the experimental data follows the theory well. At large angles, the experimental data tends to deviate. The levels at the larger angles are low and are approaching the background noise levels. This could

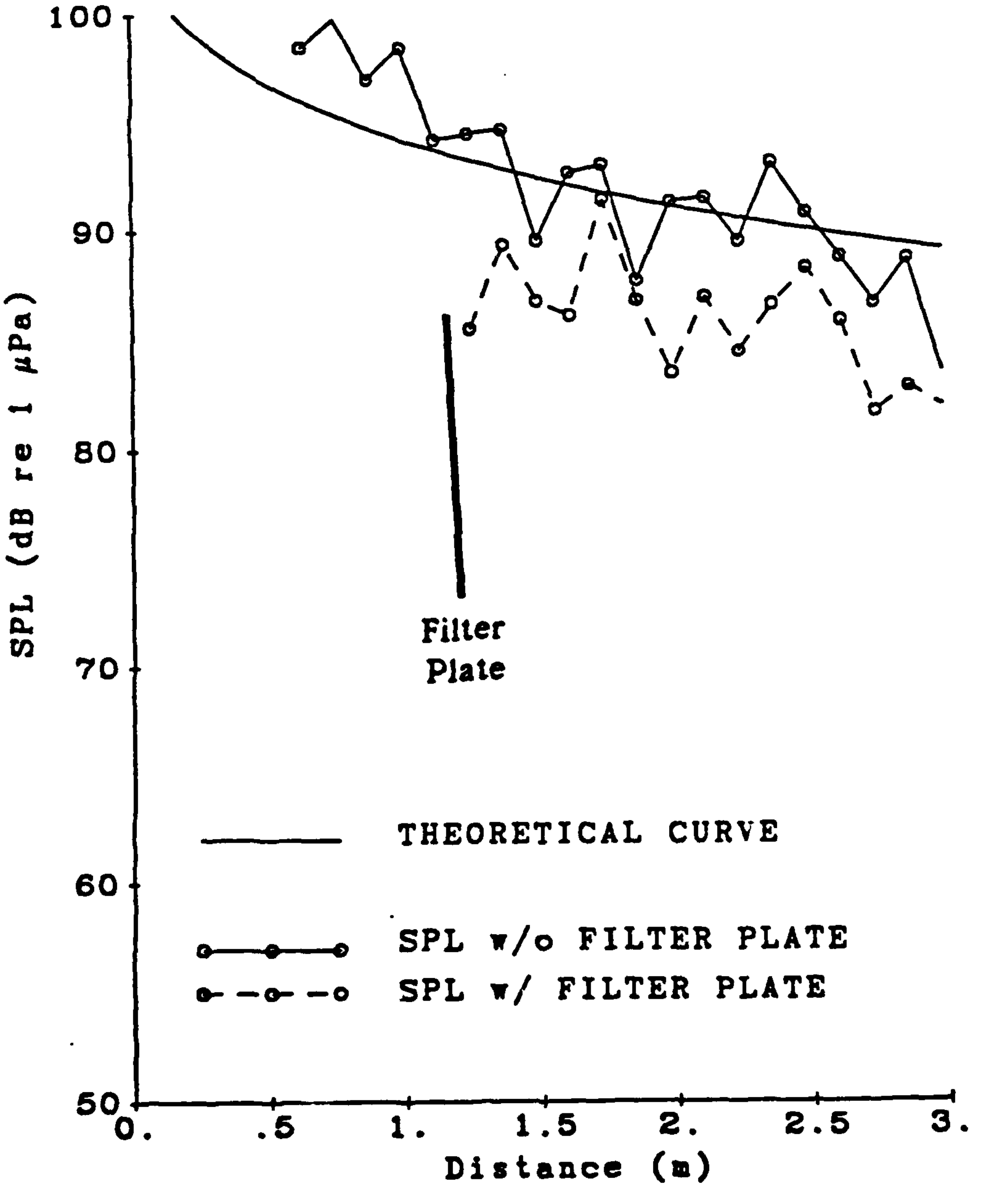

Figure 3.8. On-axis sound pressure level vs. distance, for a 10 kHz continuous parametric signal (with and without a low-pass filter plate).

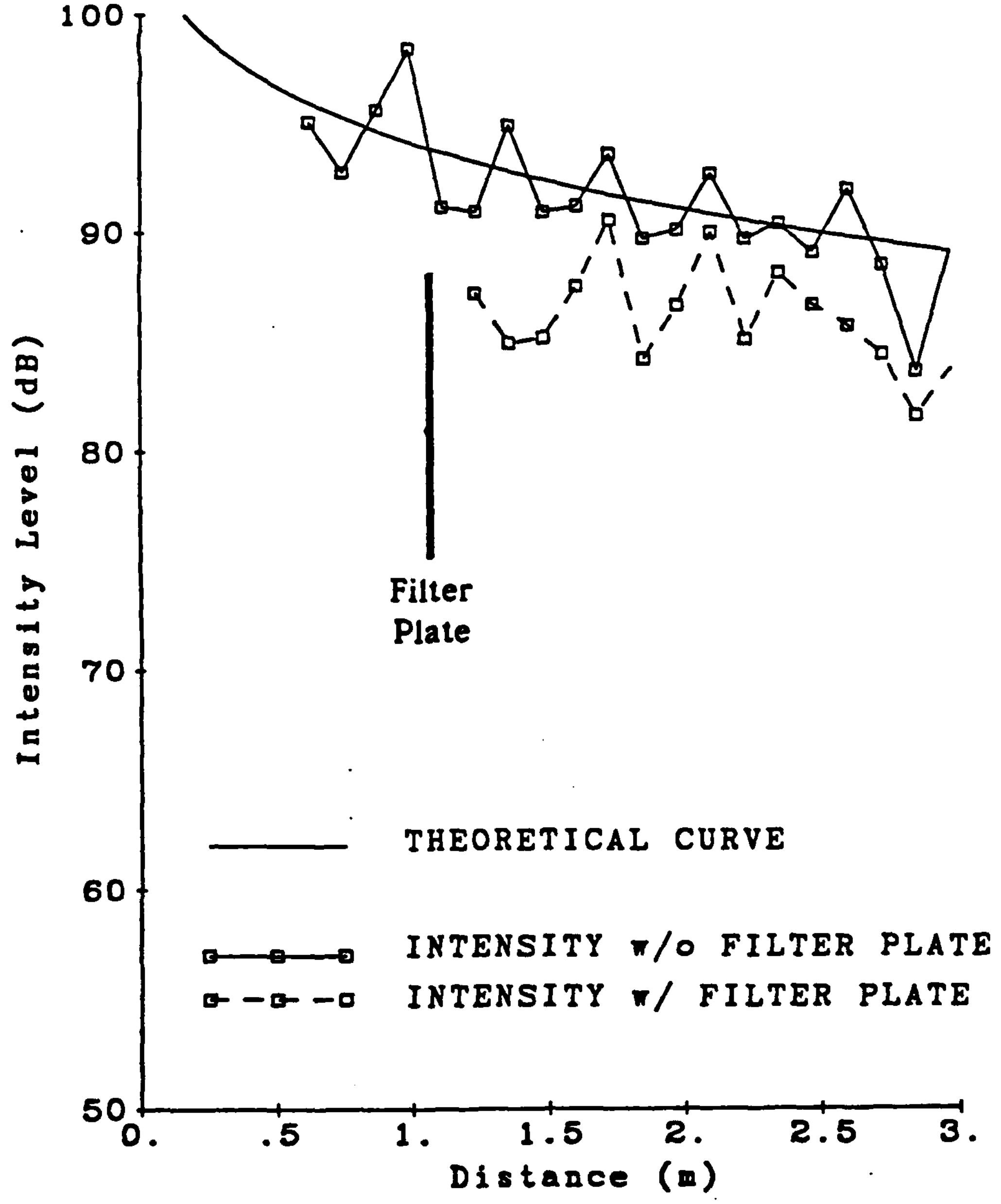

Figure 3.9. On-axis intensity vs. distance for a 10 kHz continuous parametric signal (with and without a low-pass filter plate).

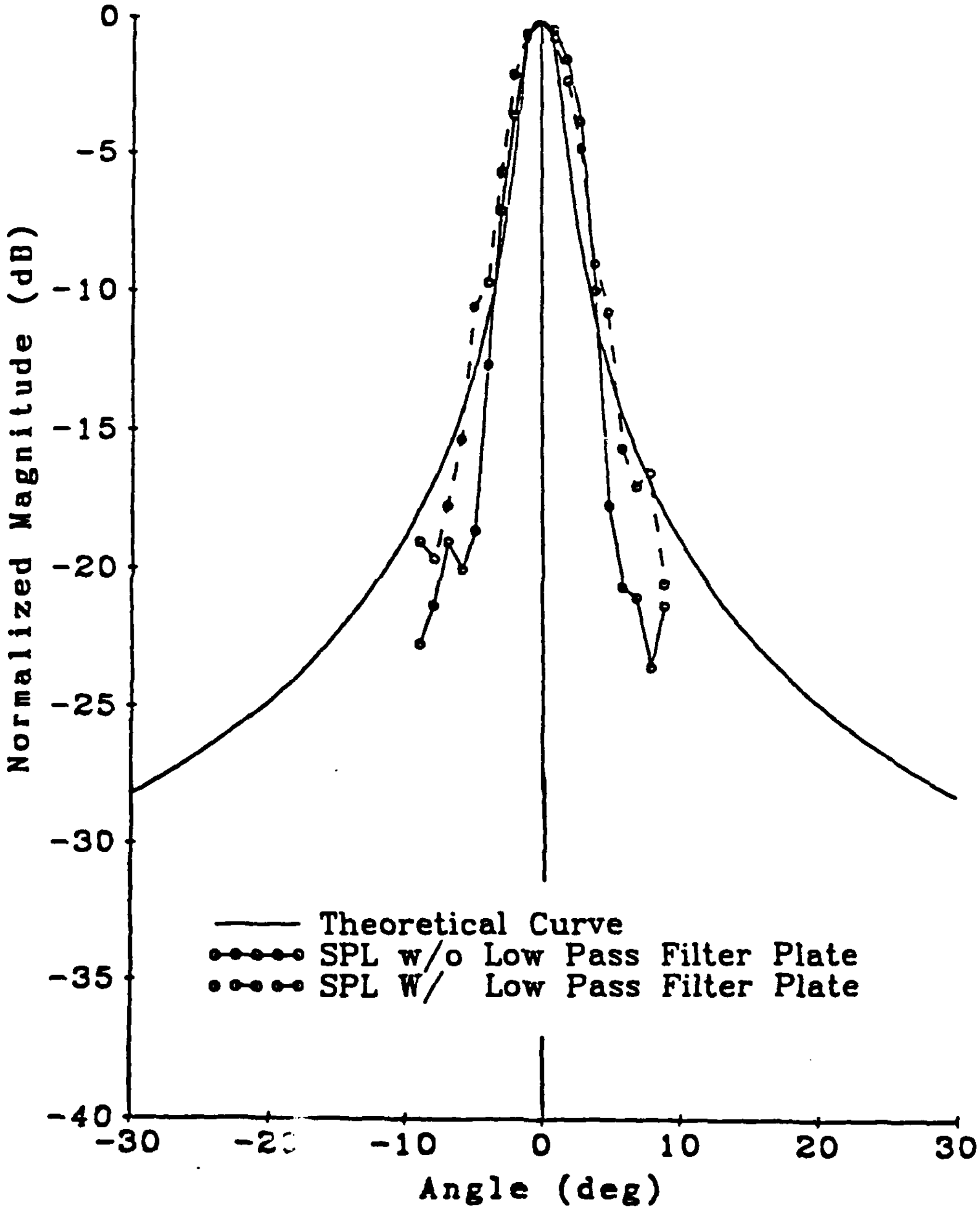

Figure 3.10. Sound pressure level vs. angle for a 10 kHz continuous parametric signal (with and without a low-pass filter plate).

account for some of the deviations at the larger angles. The sound pressure level without the low-pass filter plate shows some side lobe characteristics which is contrary to theory which states that there will be no side lobes. Without the filter plate, there is still energy at the carrier frequency reaching the hydrophones. Even with the electronic low-pass filtering, some intermodulation occurs in the receive amplifier circuits. The low frequency side lobe behavior could therefore be caused by side lobes in the projector high frequency directivity. The sound pressure level measured with the low-pass filter plate also follows the theoretical curve at small angles, but deviates for larger angles. The side lobe characteristics found without the filter plate are not present. This is due to the decrease in energy of the carrier frequency due to the filter plate. The level of the carrier frequency side lobes are not high enough to cause the intermodulation when the filter plate is present.

Measurement of the acoustic intensity versus angle was the next experiment. Figure 3.11 gives the results of this measurement. As was found with the sound pressure level measurements, the levels were comparable to the theory for small angles. For larger angles, beyond 15°, the levels were low and into the ambient noise level of the tank and could therefore not be accurately measured. The intensity system was able to pick out these levels a little better than the sound pressure level measurements because of the directional response of the intensity probe. The probe is most sensitive to acoustic energy flowing along the line joining the two

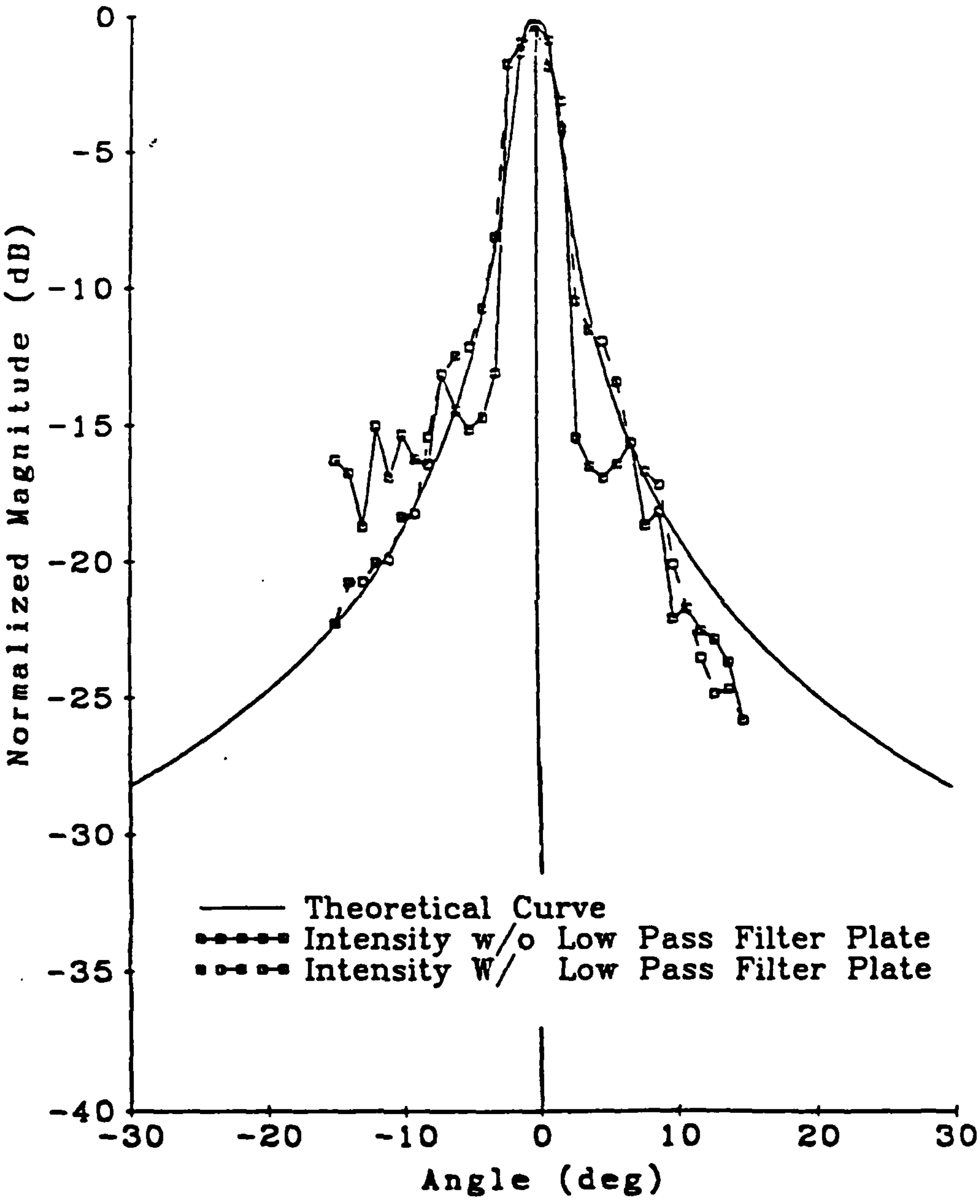

Figure 3.11. Intensity vs. angle for a 10 kHz continuous parametric signal (with and without a low-pass filter plate).

sensors. Energy from the sides is attenuated somewhat. Again, the intensity with the filter plate in place is comparable with the intensity without the filter except the side lobes of the carrier signal are not attenuated and therefore cause some intermodulation.

Comparison of the beam patterns obtained through simple pressure measurements and those obtained with the intensity technique indicate agreement between the two methods. Figures 3.12 and 3.13 compare the two techniques without and with the filter plate respectively. Agreement between the two methods occurs over all angles with the filter in position. Without the filter plate however, the results from the two techniques vary somewhat at the larger angles. This is due partly to the intensity probes directional response.

3.3.3. Intensity Scan

Scanning the intensity field of the parametric array gives an idea of where and how the 10 kHz acoustic energy flows from the source into the medium. The field was scanned in the vertical plane on the axis of the array. The experimental procedure involved moving the two-sensor probe to discrete distances and depths along the center of the tank. At each of these locations, two measurements were made, one with the probe aligned horizontally, another with the probe in a vertical position. When the probe is aligned horizontally, the line joining the two sensors is horizontal in the tank thereby measuring the horizontal component of the acoustic intensity. With the probe aligned vertically, the line joining the two sensors is

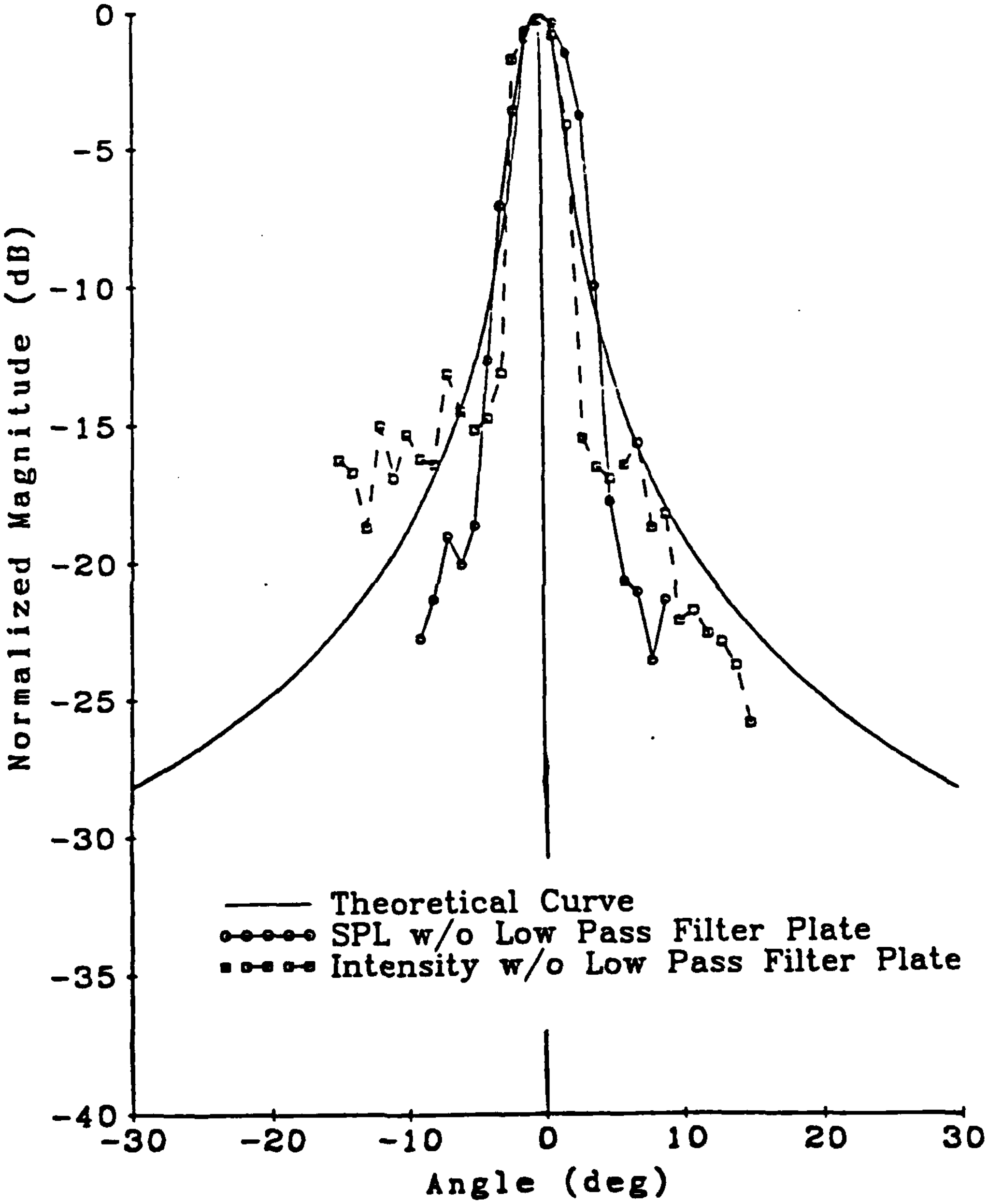

Figure 3.12. Intensity and pressure vs. angle for a 10 kHz continuous parametric signal (without a low-pass filter plate).

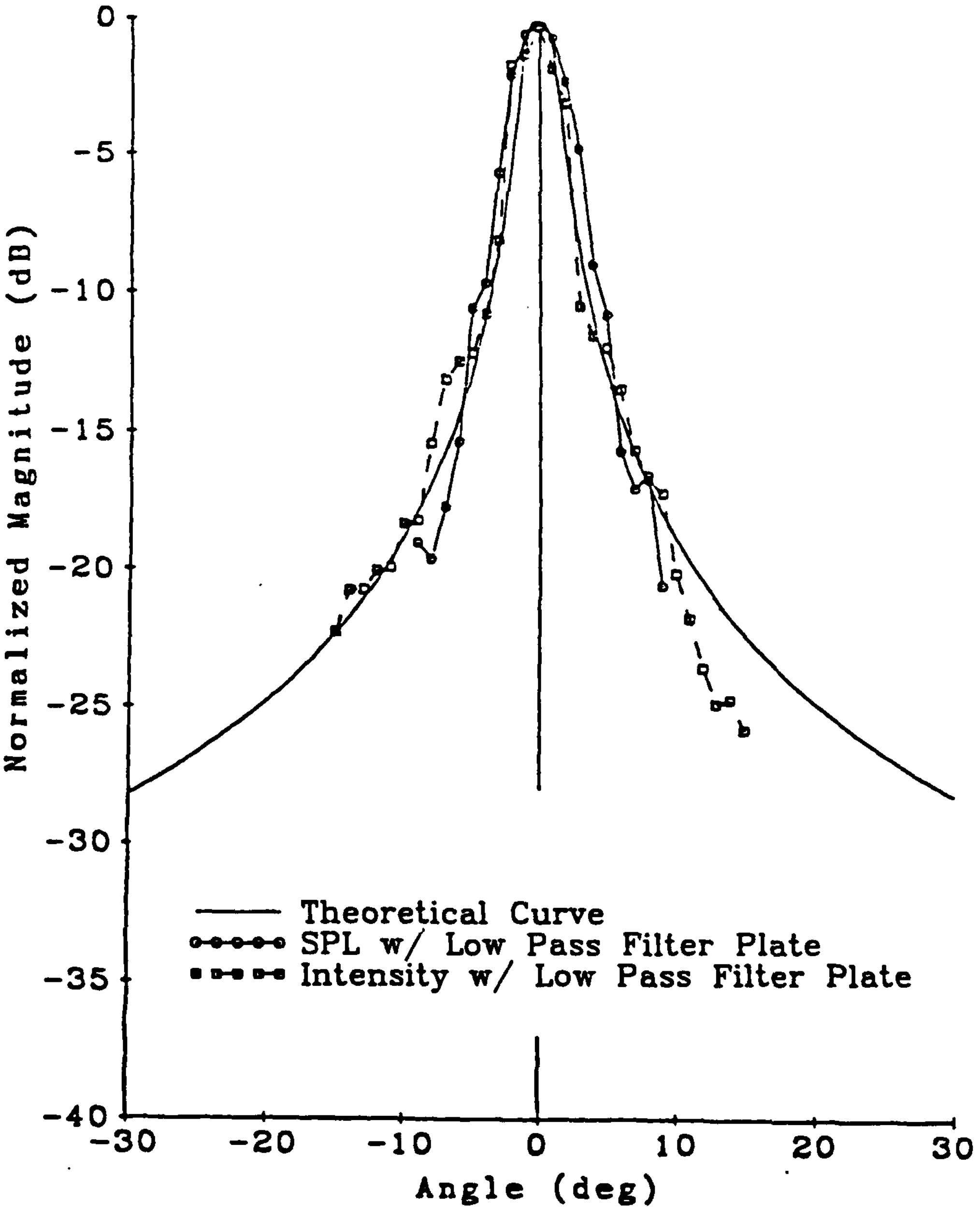

Figure 3.13. Intensity and pressure vs. angle for a 10 kHz continuous parametric signal (with a low-pass filter plate).

vertical thereby measuring the vertical component of the acoustic intensity. Using these two measurements, the intensity vector in the vertical plane can be derived.

The first measurement was made without the filter plate in place. The results from this measurement are given in Figure 3.14. The active intensity, Figure 3.14a, shows the direction and magnitude of the acoustic energy flow. It is apparent from this figure that the energy is flowing out of the source which is located at the center on the left hand side of the plot. The maximum acoustic energy flow is located on the axis of the source. The smaller arrows as we move away from the source show the decrease in intensity with distance.

The second plot, Figure 3.14b, shows the reactive intensity. The reactive intensity shows the standing wave component of the acoustic field. The direction of the reactive intensity vectors normally points out of pressure maxima and into pressure minima. In this case, we would expect the reactive intensity to be pointing out of the axis of the array and away from the source point. This would be a valid assumption because the maximum acoustic pressure is located on the axis of the source and at the source. In this setup, we have a pressure release boundary at the water-air interface located at the top of the figure. A pressure release boundary gives zero pressure. This situation could explain the upward direction of the vectors, into the pressure minimum at the surface. Even with this situation, we would expect there to be a standing wave set up in the vertical direction. This would lead to alternating pressure

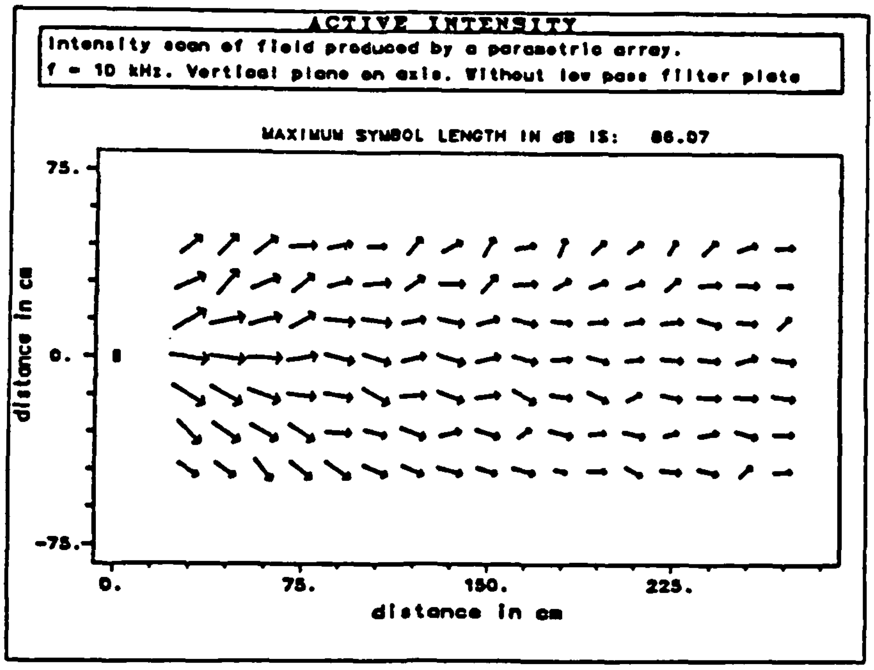

(a) Active intensity

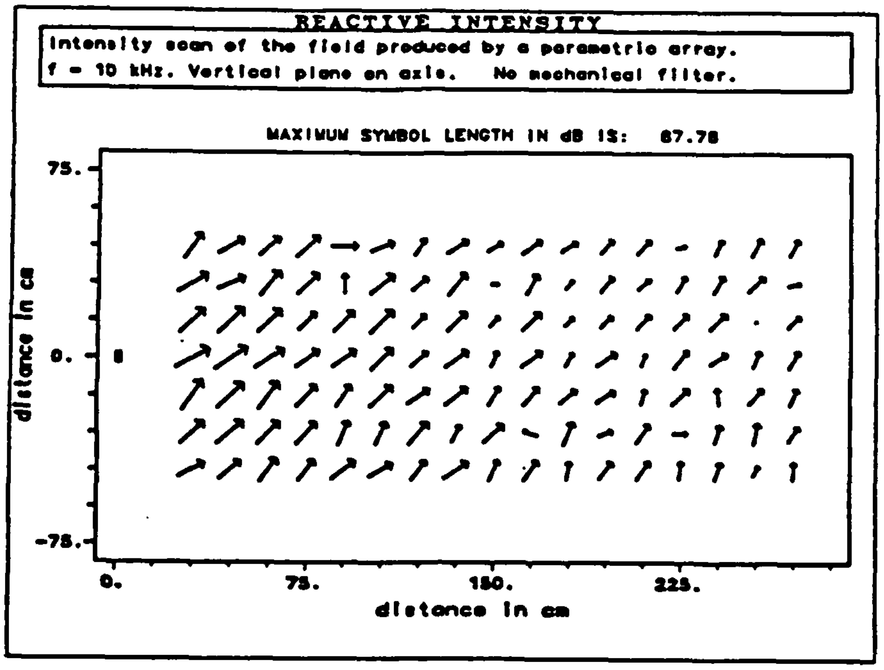

(b) Reactive intensity

Figure 3.14. Intensity field of a 10 kHz - continuous parametric signal. Measured in the vertical plane on the axis of the source (without a low-pass filter plate).

maxima and minima in the vertical direction. The reactive intensity does not show this behavior which would lead us to expect some other reason.

Another possible explanation of the reactive intensity field would be bias errors caused by magnitude mismatch between the two sensors. Observe that the reactive intensity levels are the same or only slightly lower than the active intensity levels. Since the reactive intensity is rather low, compared to the noise in the tank the acoustic field is essentially free with little standing wave behavior present. Bias errors for the reactive intensity are given as the ratio of the magnitude mismatch to the field amplitude difference. In a free field situation, indicated by a zero reactive intensity level, the field amplitude difference between the two closely spaced sensors is small. Therefore, the bias errors caused by even very small magnitude mismatches can be large. In fact, the effects of the small field amplitude difference is enough to dominate any magnitude calibrations that we are able to make.

The low reactive field does not indicate a problem with the measurement scheme. It does show that the wedges are effective in absorbing the 10 kHz signal and that the field is essentially free.

The next measurement which was made was with the low-pass filter plate positioned 1 m. from the source. As before, the field was sampled at discrete points on the side of the plate opposite from the source. Figure 3.15 shows the active and reactive fields. The active intensity field shows some energy diffraction around the plate. This

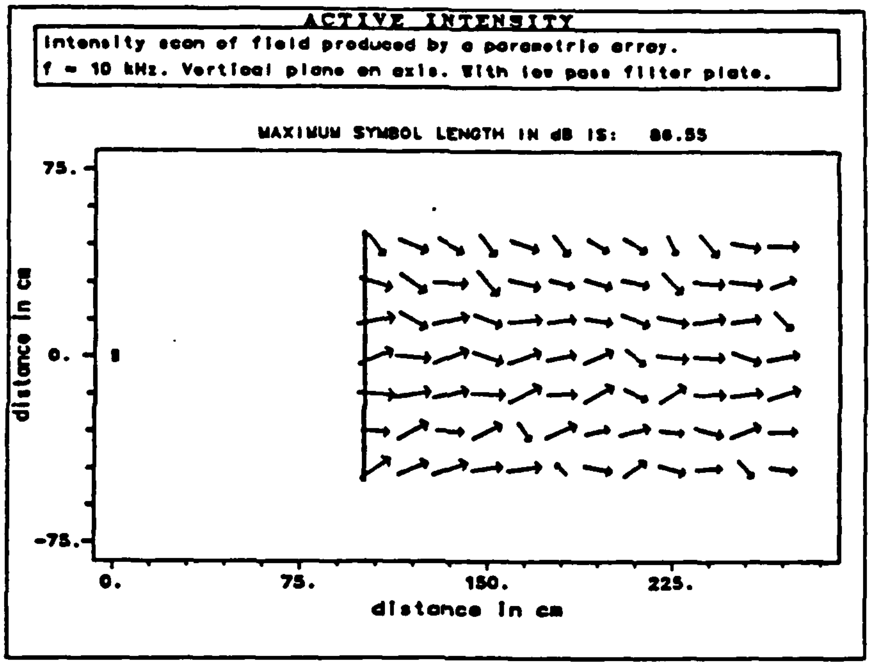

(a) Active intensity

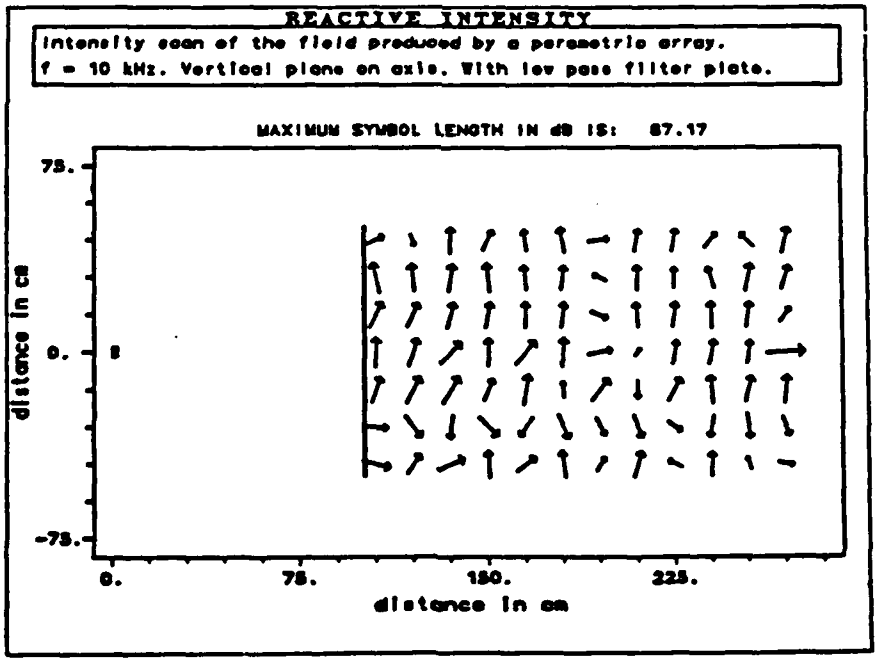

(b) Reactive intensity

Figure 3.15. Intensity field of a 10 kHz continuous parametric signal. Measured in the vertical plane on the axis of the source (with a low-pass filter plate).

is indicated by the inward pointing vectors at the edges of the plate. The rest of the field, while slightly irregular, does show the left to right propagation of the acoustic energy. The reactive intensity shown follows the same tendencies as were reported for the case without the low-pass filter plate. The reactive intensity vectors are generally pointing from the bottom to top of the tank. The same explanations given previously could also apply here.

To test if the field was actually behaving as indicated by the reactive intensity or if the field amplitude differences were too small to be measured, an auxiliary test was performed. This test consisted of measuring the reactive intensity of a small section of the acoustic field. The intensity probe was rotated 180° and the reactive intensity was again measured. If the field was actually as indicated, then the reactive intensity vectors measured in the two scans would have the same magnitude but opposite directions. Figures 3.16 and 3.17 show the results of this test. The active intensity, given by the top figures is unaffected by probe 180° rotation. Note that the computer program used to plot these figures accounts for the probes 180° rotation by multiplying the vectors of one of the plots by -1. In any case, the active intensity, accounting for the 180° rotation, is not affected to a great extent by the probe orientation. The slight differences between the two active intensity plots shown in Figures 3.15a and 3.16a could be caused by errors in placement of the intensity probe. The reactive intensity changes its amplitude and direction considerably from one scan to the next. If there were no

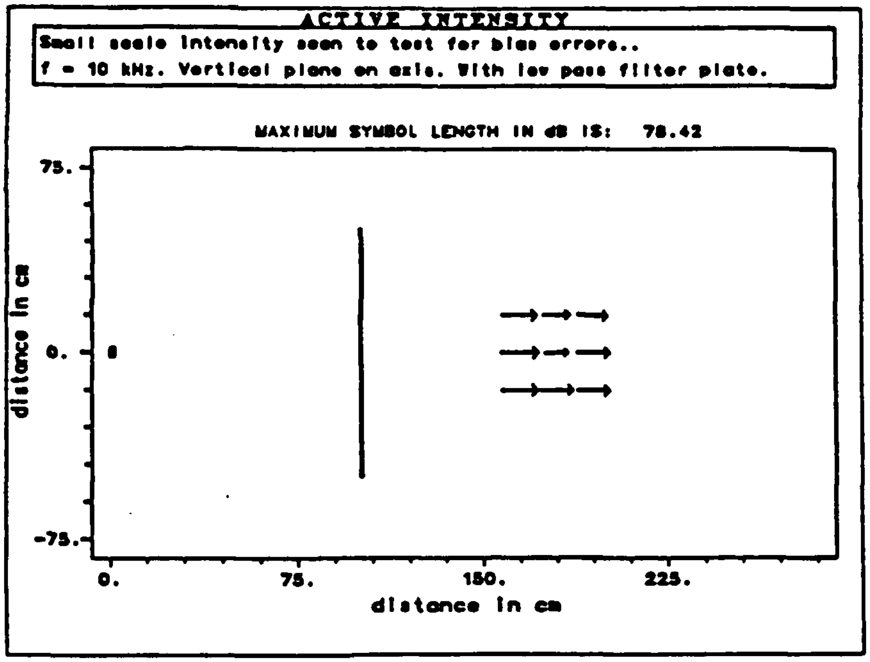

(a) Active intensity

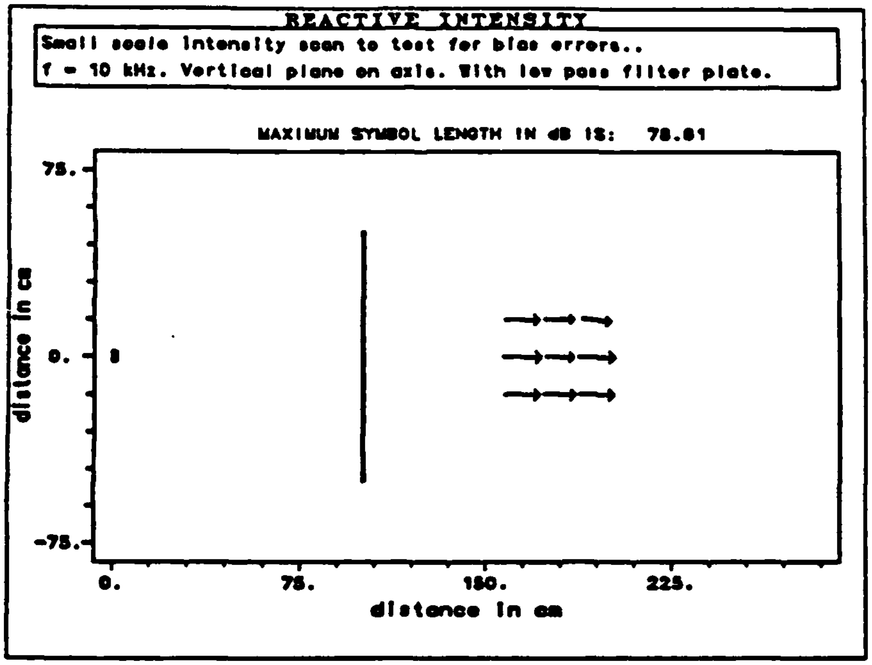

(b) Reactive intensity

Figure 3.16. Intensity scan on the field produced by a parametric array to test for magnitude mismatch bias errors. Probe in normal "positive direction"

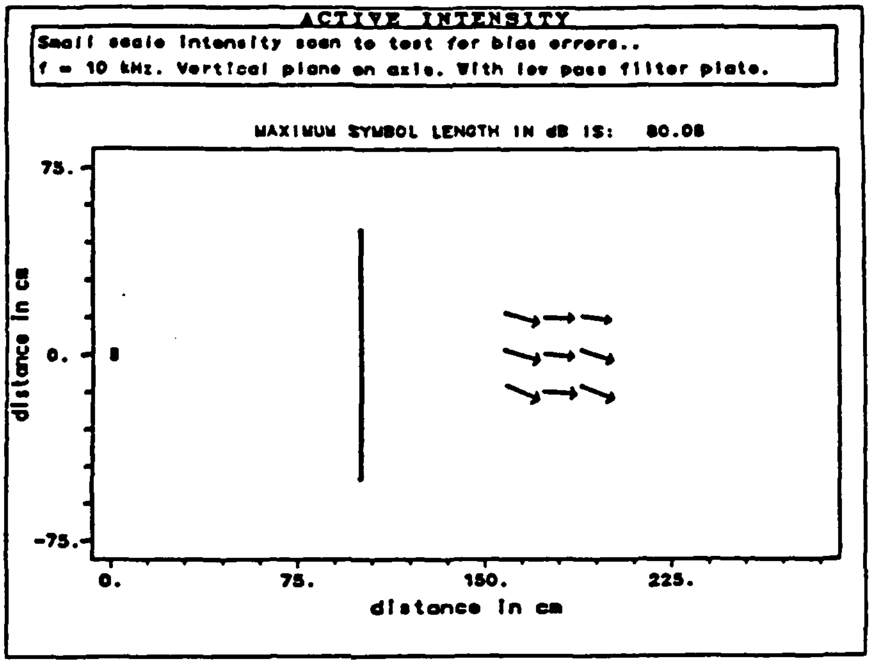

(a) Active intensity

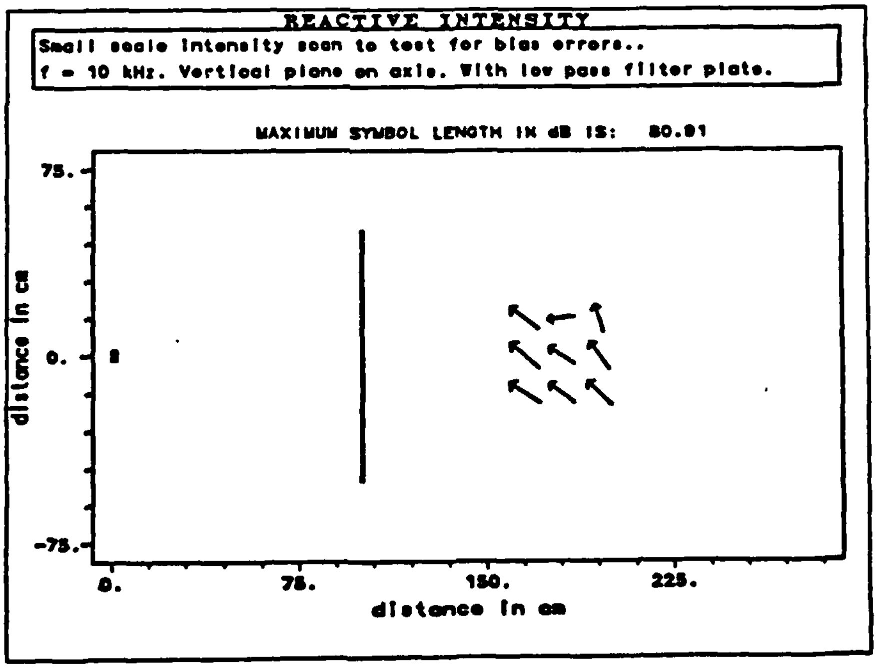

(b) Reactive intensity

Figure 3.17. Intensity scan on the field produced by a parametric array to test for magnitude mismatch bias errors. Probe in switched or "negative position"

magnitude mismatches in the system or if the mismatches were much smaller than the field magnitude differences, then the reactive intensity would have behaved similarly to the active intensity. This result indicates that there are in fact some magnitude mismatches present in the system compared to the magnitude differences which were measured.

To test the extent of the magnitude mismatch, the probe was placed in a situation which would produce a highly reactive field. This situation was produced by placing the probe close to the filter plate on the same side as the source. The reactive intensity was measured with the probe aligned in the two directions as before. Again, the reactive intensity vector from the rotated probe should have the same magnitude but different direction. The magnitudes obtained from this measurement were consistently within 1 dB of each other and the directions were always opposite. Allowing for inconsistencies in the placement of the hydrophone from measurement to measurement, this result is considered within experimental error. This experiment therefore shows that the probe is able to measure higher reactive intensities but that errors in magnitude matching are extensive at low levels of the reactive intensity obtained from the parametric array at 10 kHz.

As another assessment of the parametric array intensity, a scan was made of the field produced by a conventional linear source. The linear source tested was a 6 inch diameter free flooding cylindrical projector with 12 inch diameter plexiglass discs attached to the top and bottom of the cylinder. The projector is an ITC model MOD2002A transducer. It is possible that the plexiglass discs on the top and bottom of the transducer alter the omni-directional pattern of the transducer in the vertical plane causing some directional characteristics. Figure 3.18 shows the active and reactive intensity scans in the vertical plane on the axis of this projector. This figure indicates the outward radiating vectors near the source and the decrease of active intensity with distance. The reactive intensity shows the same bottom to top tendencies as the parametric array field. The reactive intensity level is again the same or only slightly below the active intensity indicating a low reactive intensity. The same explanation of overriding magnitude bias errors is appropriate.

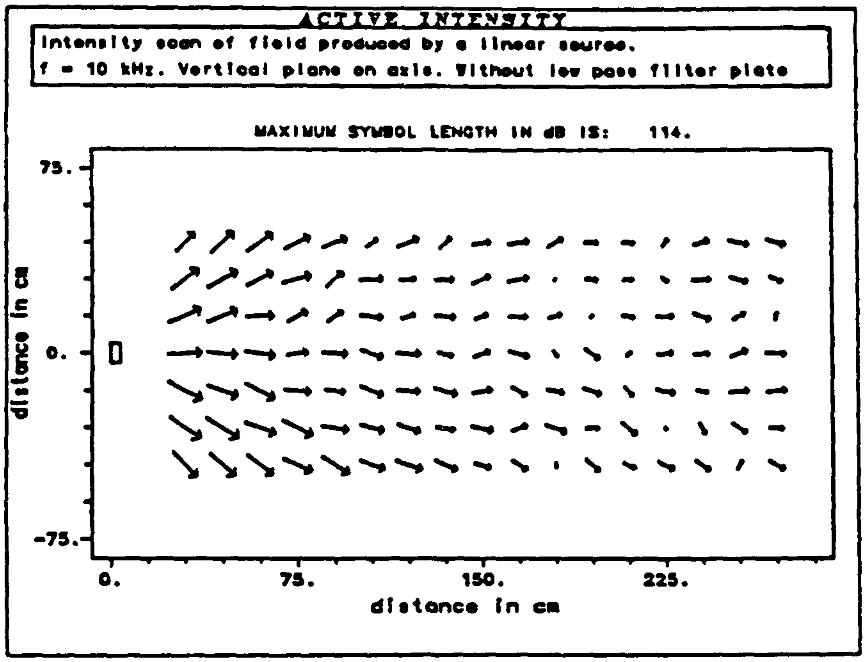

(a) Active intensity

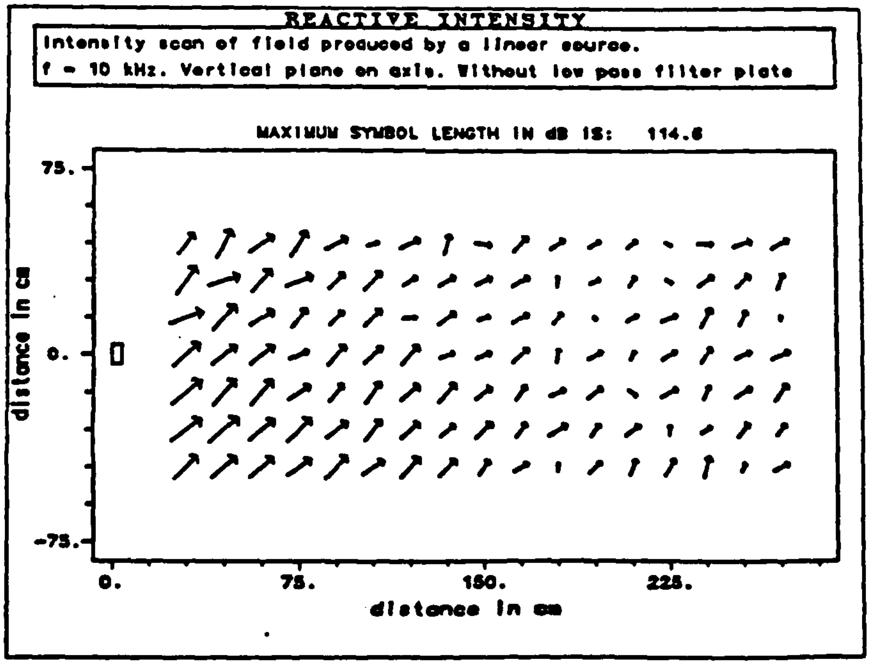

(b) Reactive intensity

Figure 3.18. Intensity field of a 10 kHz continuous conventional signal. Measured in the vertical plane on the axis of the source (without a low-pass filter plate).

Chapter 4

EXPERIMENTAL SET-UP

4.1. Introduction

The data acquisition and signal processing performed in this research were based in-part on existing software that was developed by Elko[23] for intensity measurements in air. This chapter cutlines the procedure used for measuring intensity and impedance and describes the apparatus necessary for the formation of the parametric array. Also included in this chapter is a description of the anechoic tank facility and its acoustic characteristics.

4.2. Intensity Instrumentation

To measure the acoustic intensity in water, hydrophones where used instead of microphones. The rest of the intensity data acquisition system was essentially the same as for in-air experiments. At first the hydrophones were to be designed and built in-house. These hydrophone were made out of a perforated PZT-polymer "3-1" composite provided by the Materials Research Laboratory of P.S.U. The basic characteristics of these polymer composites is described by Safari, et al.[28]. The PZT-polymer composites were prepared by drilling holes in sintered PZT blocks and filling the perforated block with a polymer. By drilling the holes perpendicular to the poling direction, the sensitivity of the piezoelectric composite was greatly increased over standard PZT materials. A sample of this type of hydrophone was fabricated and tested, but its frequency response was not satisfactory as can be seen in the lower curve of Figure 4.1. Although further development of this transducer may alleviate the problem with the frequency response, it was decided to proceed with a commercially available hydrophone. The hydrophone that was selected was a Celesco Industries LC-10 Hydrophone. This hydrophone was chosen for its small size (0.4" in diameter by 2.1" long), its flat frequency response and for its high sensitivity. The upper curve of Figure 4.1 shows the frequency response of a typical LC-10 hydrophone. Comparing this response to that of the PZT hydrophone indicates that the response of the LC-10 is more desirable in terms of both its more flat frequency dependence and its higher free field sensitivity. Later experiments with the phase calibrations indicated that it also had desirable phase characteristics. The hydrophones were held in a position side by side by a small aluminum bracket with a fixed separation of 7/8 inch. This configuration, Figure 4.2, is advantageous over the end to end configuration in that it allows the probe to be placed close to the sample. Another advantage of this configuration is that the acoustic centers of the hydrophones are easier to locate along the axis than on the side.

The signal from the hydrophones is first filtered by an Ithaco Model 4113 electronic filter to attenuate the high frequency carrier wave leaving only the low frequency difference signal. An Ithaco Model 435 amplifier is used to amplify the signal to a level acceptable for the A/D converters. The anti-alias filtering is accomplished by a Rockland Wavetek System 816 filter. This filter

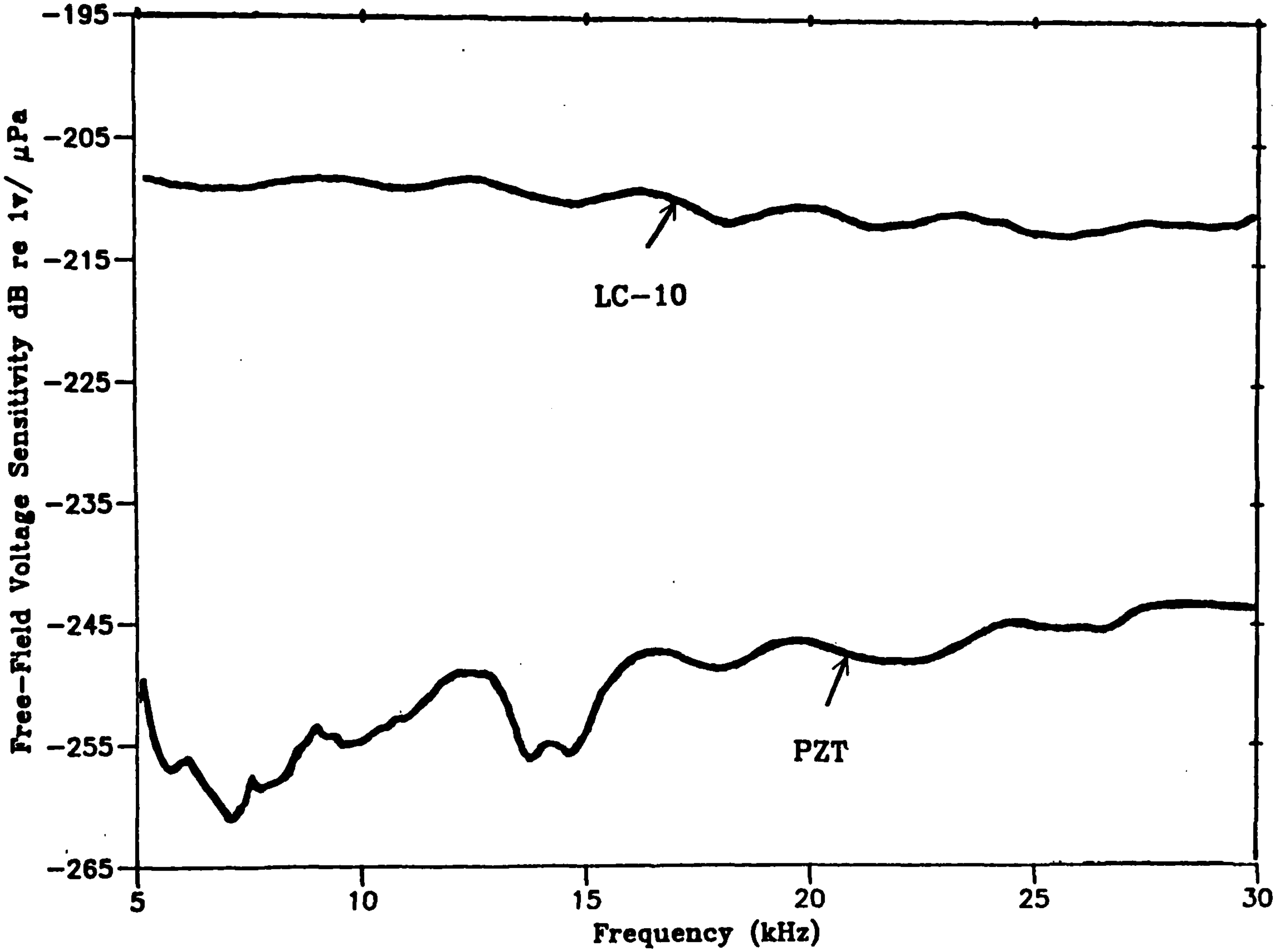

Figure 4.1. Free-field voltage sensitivity of representative perforated PZT and LC-10 hydrophones.

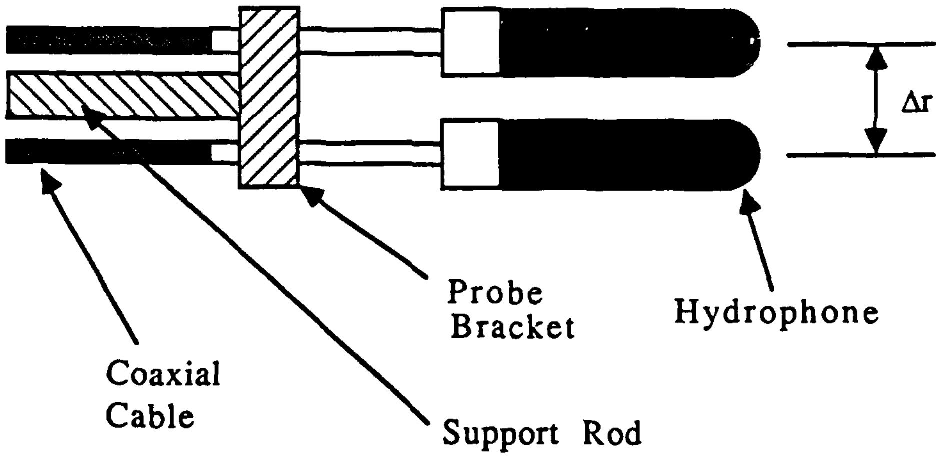

Figure 4.2. Sketch of side by side hydrophone positioning bracket.

has a variable cutoff frequency and was set to the sampling frequency which is 12 kHz. Next, the analog signal is converted to the required digital signal by a 16 channel Computer Design and Applications MIP-3A analog to digital converter. The resulting digital signal is then stored in a Digital PDP-11 minicomputer which runs the data acquisition program. A Computer Design and Applications array processor then performs the FFTs on the data necessary for the calculation of the autospectra and the complex cross-spectrum. The PDP-11 uses the autospectra and the cross-spectrum to calculate the acoustic intensities, energies densities and specific acoustic impedances. Display of the graphics is made on a Tektronix 4010-1 terminal and hard copy graphics are available on a Tektronix 4611 plotter or on a laser printer via the VAX 780 main frame computer. A block diagram of the signal path of the intensity measurement system is given in Figure 4.3.

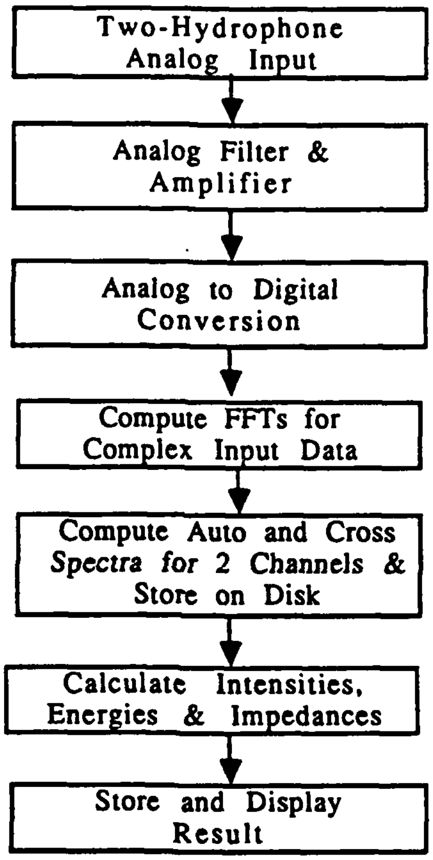

Figure 4.3. Intensity measurement instrumentation block diagram.

4.3. Parametric Array Instrumentation

The source of acoustic energy in this experiment was a nonlinear parametric array. The formation of the parametric array requires an amplitude modulated acoustic signal of sufficiently high amplitude to allow the medium to react nonlinearly thereby producing the desired low frequency difference signal. The high frequency carrier signal is greatly attenuated by the absorption of the water while the low frequency difference or modulation signal will propagate.

The projector used for the sound source in this experiment was a Lowrance Model TTH-2192-8 transducer. This transducer was chosen for its high resonant frequency and for its small size. The active region of the projector is approximately 1 inch in diameter and its resonant frequency is 192 kHz. This frequency was not chosen as the center frequency for the parametric array, however, because the amplifier we had available was not able to produce sufficiently high levels for the desired nonlinear effects. A scan of the frequency from 100 to 300 kHz indicated that the best frequency for the projector-amplifier combination is actually 131 kHz. Figure 4.4 shows the transmitting voltage response of the projector when a high frequency amplifier is used. Peaks in the response are located at 131 kHz, 192 kHz and 230 kHz.

The amplifier used in this study was a McIntosh MI200AB 60 Watt power amplifier. The output from the amplifier was fed to the projector through an impedance matching network which was set to 600 Ω. It was found that there was a slight direct radiation of the difference frequency by the transducer. The signal for this direct radiation was formed by nonlinear effects in the power amplifier. For this reason, a high-pass filter was placed in line between the amplifier and the projector. This filter took the form of a simple RC

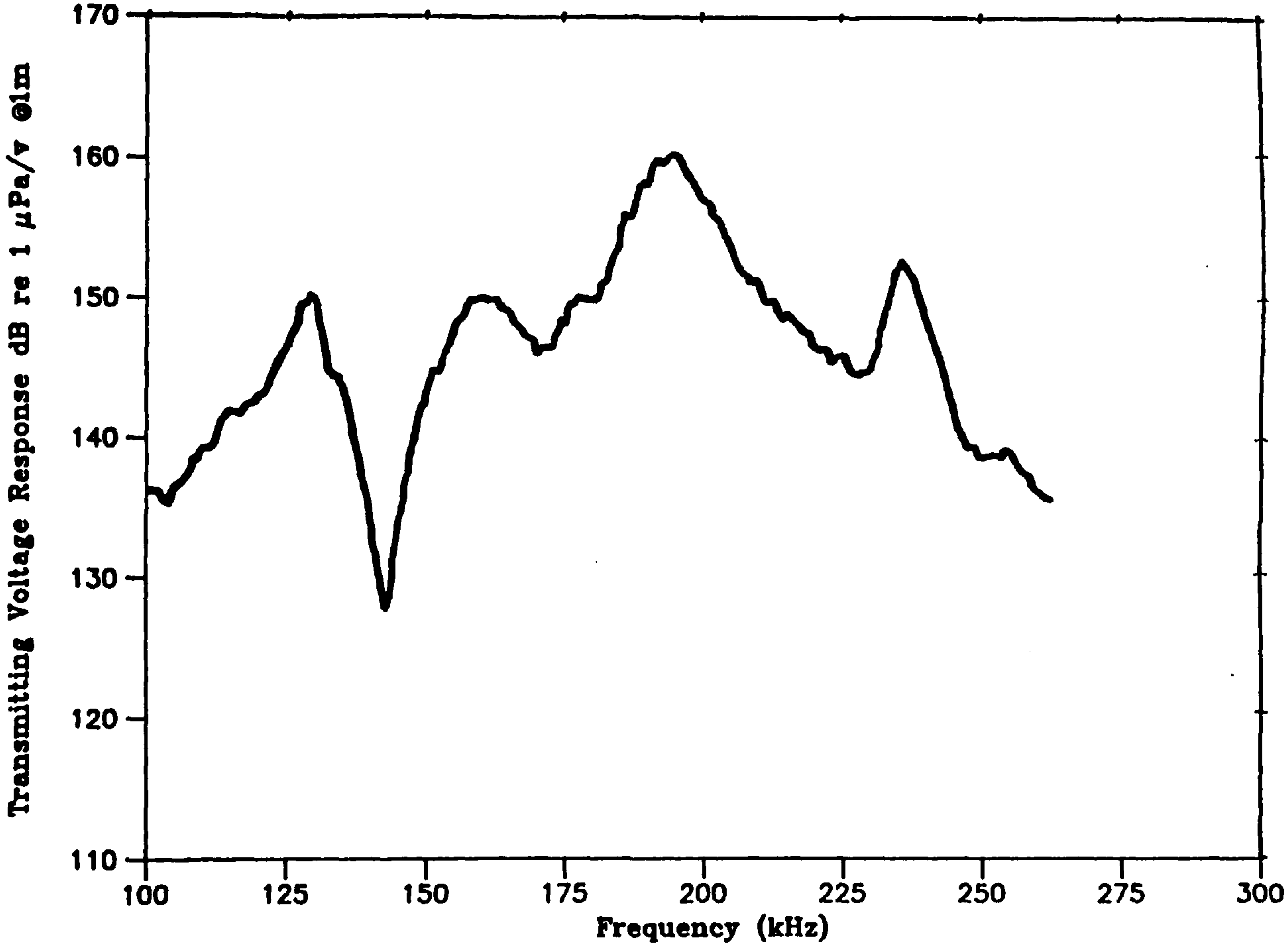

Figure 4.4. Transmitting voltage response of the Lowrance TTH-2192-8 transducer.

network with the hydrophone impedance providing the resistive components and an external capacitor providing the capacitance.

The two types of signals for the parametric array could be either the sum of two high frequency primary components or an amplitude modulated high frequency carrier signal. The latter of these two input signals, the amplitude modulated signal, was chosen because of its ease of operation and for a slight increase in difference frequency level for this mode. In terms of operation, using the amplitude modulation scheme requires only the adjustment of the amplitude modulation frequency where the two signal scheme would require adjusting both of the high frequency components around a center frequency. The increase in difference frequency signal generation using the amplitude modulated signal compared to the classical two frequency procedure was found by Eller[29] to be around 2.5 dB.

The amplitude modulated signal was provided by a Hewlett-Packard Model 3314 Function Generator. The function generator modulated the amplitude of the internally produced high frequency carrier signal by a low frequency signal provided by a Rockland Model 5100 Frequency Synthesizer. A block diagram of the parametric array input signal instrumentation is given in Figure 4.5.

Since the size of the water tank limits the distance from the source to the test specimen, the experiments had to be performed in the near field of the array. It is desirable therefore to filter the high frequency component out of the signal to limit the region of

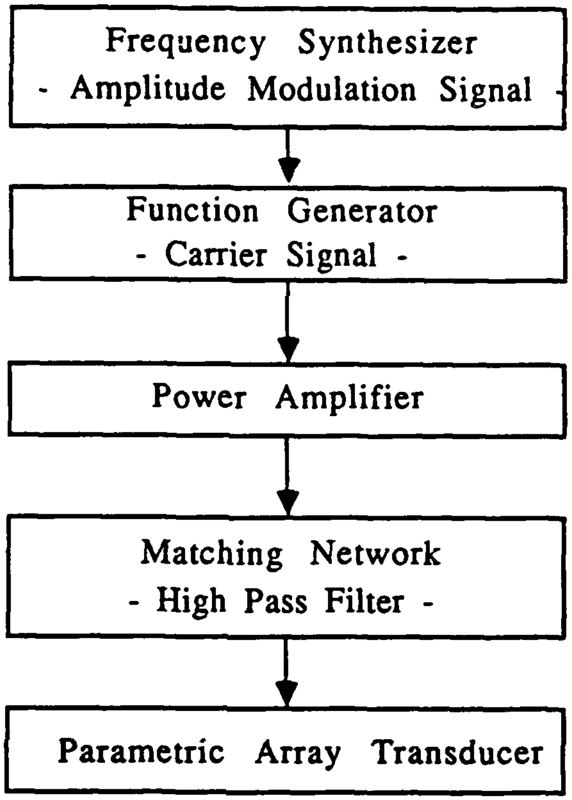

Figure 4.5. Parametric array instrumentation diagram.

interaction. This filter took the form of a thin plate whose thickness was chosen to attenuate the 131 kHz carrier frequency while passing the difference frequency component with little attenuation. If the measurements could be made in the far field of the transducer, then the absorption of the high frequency carrier would be accomplished by the water.

A thin plate will provide maximum transmission loss of a signal if the thickness of the filter plate is a quarter of an acoustic wavelength. The decision of which material to use to make the filter was based on maximum attenuation and weight. The material chosen was aluminum. At 131 kHz a signal has a wavelength of 1.9 inches in aluminum. A quarter wavelength would therefore be 0.5 inches. The filter plate which was utilized was 36 × 36 × 0.5 inches. The dimensions of this plate were such that the majority of the beam formed by the parametric array would be completely covered.

The transmission loss of a plate for normally incident sound is given by [30]

$$TL \approx 10 \log_{10} \left\{ \frac{1}{1 + \frac{1}{4}\left(\frac{Z_1}{Z_2}\right)^2 \sin^2\left(k_2 L\right)} \right\} \tag{4.1}$$

where Z_2 and Z_1 are the magnitudes of the impedance for the filter plate and the surrounding fluid respectively. Application of this expression gives a transmission loss of 15 dB at 131 kHz while the transmission loss at 10 kHz is less than 2 dB. Figures 4.6 and 4.7 give the normal incidence transmission loss compiled from Eq.(4.1) for a 0.5 inch thick aluminum plate at high and low frequencies respectively.

4.4. Water Tank Environment

The water tank used in this experiment is approximately 3 × 6 × 5 meters. The walls of the tank are lined with wedges of sound absorbing material approximately 1.5 meters long. The floor of the tank is also lined with these "ensilcrete" wedges. The top of

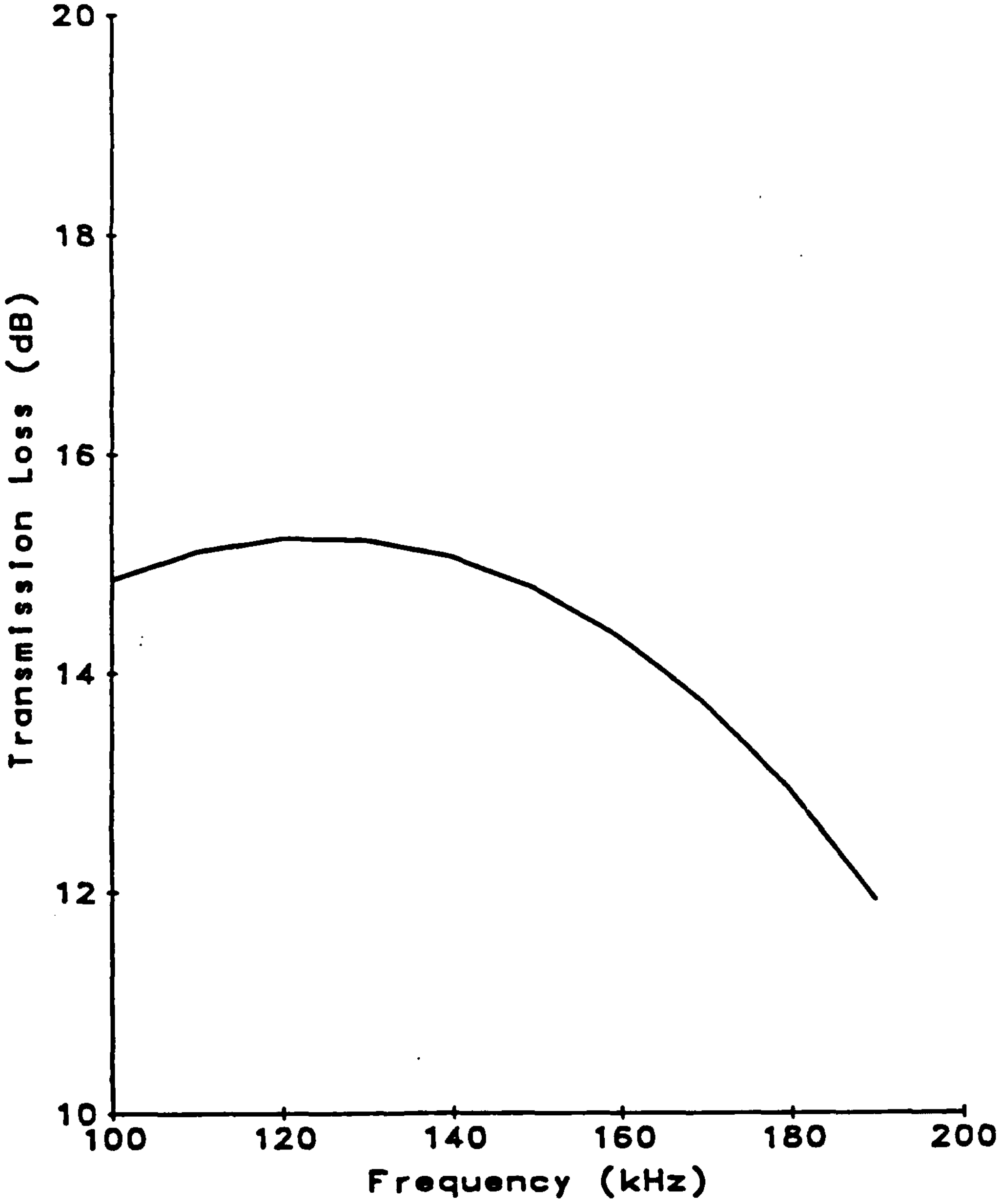

Figure 4.6. Transmission loss of a 1/2 inch aluminum plate at high frequencies.

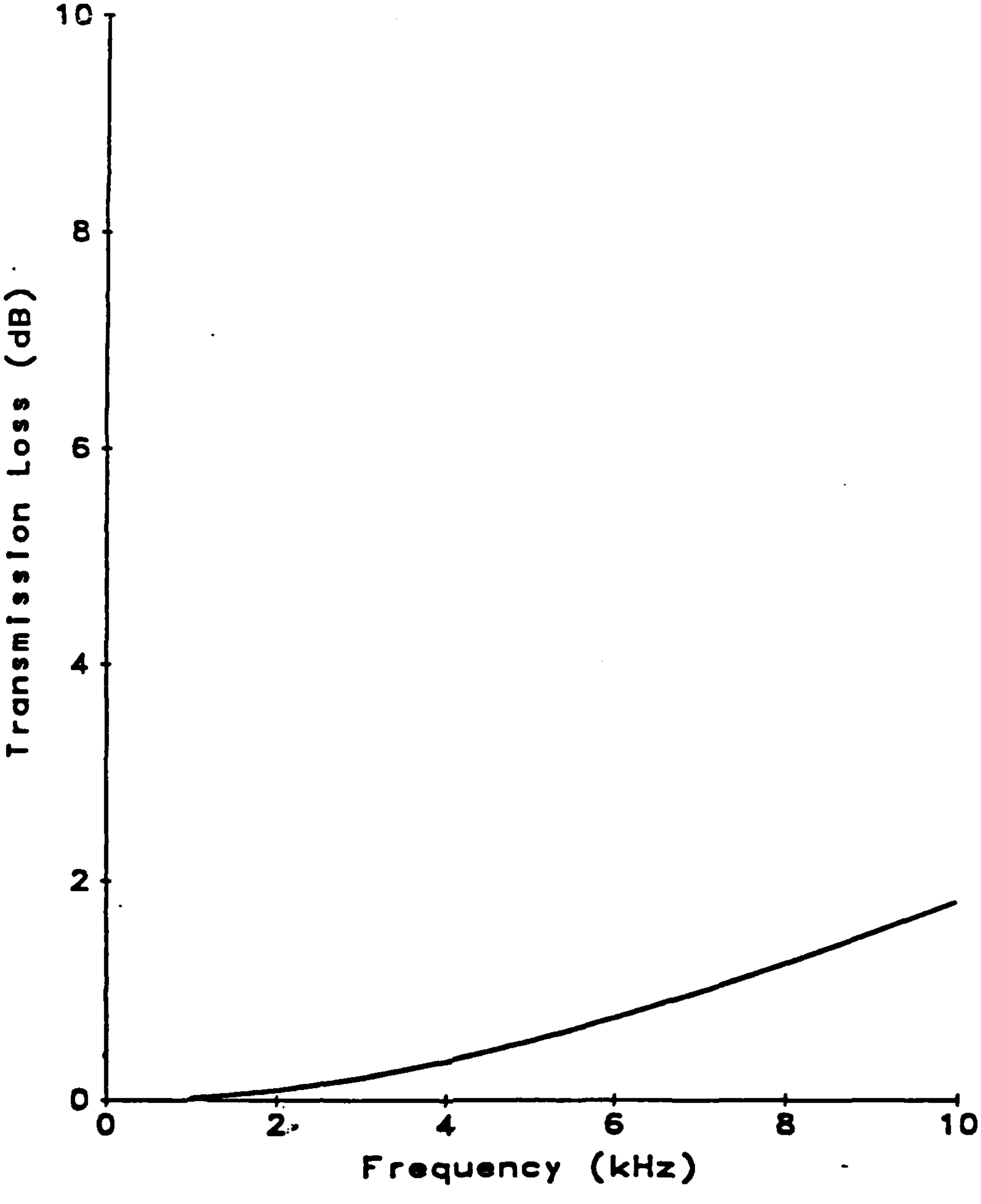

Figure 4.7. Transmission loss of a 1/2 inch aluminum plate at low frequencies.

the tank represents a pressure release boundary. Preparation of the tank for use in this experiment involved draining the water and cleaning the plastic liner which separates the measurement environment from the wedges. The tank is provided with a filter system which allows the water in the tank to be circulated and filtered. This system has a separate filter for the inside and outside tanks.

Movement of the test panel was accomplished using a positioning trolley. This trolley allowed movement of the plate along the length of the tank and up and down in the tank. The support mechanism on the trolley also allowed rotation of the plate along their center axis. The angle of the plate surface could be measured with an indicator attached to the support. Figure 4.8 gives a diagram of the water tank and the location of the parametric array and the two hydrophone probe. The filter plate and test specimen were positioned in the tank so that the axis of the source corresponds with the center of the plate.

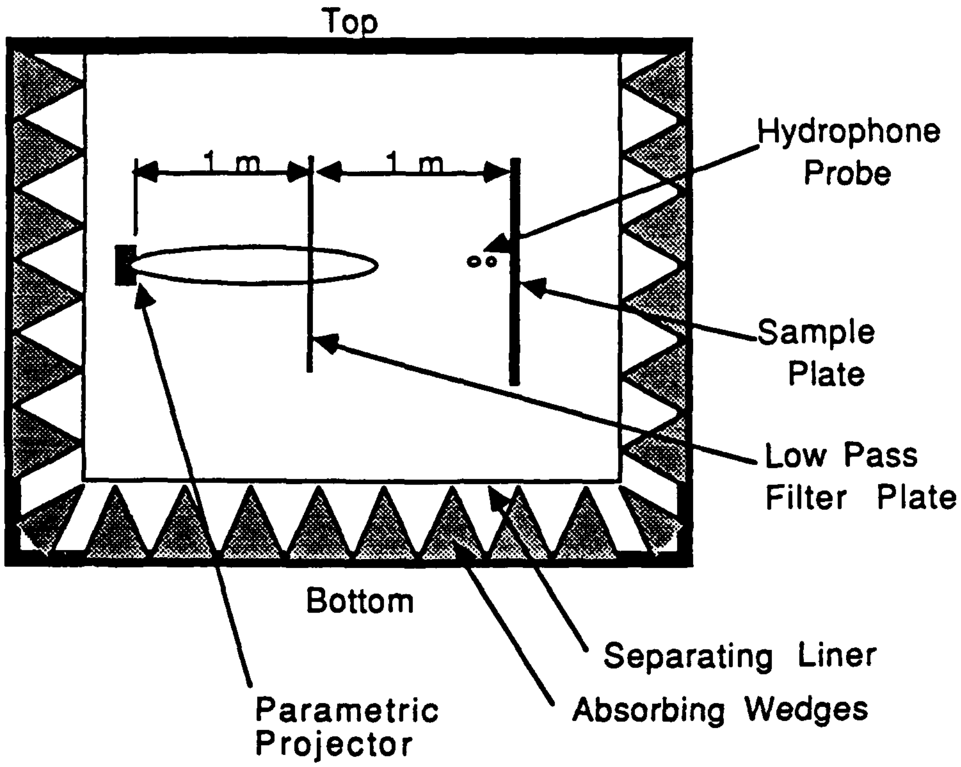

Figure 4.8. Sketch of the water tank environment.

Chapter 5

THE REFLECTION COEFFICIENT

5.1. Introduction

The research described in this thesis has involved designing and implementing a system which would be capable of measuring the acoustic fields scattered by submerged structures. One application of this system is to measure the complex acoustic impedance of a submerged coated plate. To assess the system, we used the intensity scheme to measure the normal component of the specific acoustic impedance of various coated and uncoated plates at oblique angles of incidence. From the measured impedance, we are able to infer the complex surface impedance and ultimately the complex reflectivity of the plate. This chapter outlines the theoretical basis by which we compare the experimental results obtained in this research.

5.2. Theory

Junger and Feit[29] describe the sound field which results when a plane acoustic wave impinges on an infinite elastic plate. Two assumptions are made here; one, that the incident wave is planer and, two, that the plate is infinite. The first of these assumptions is approximately true for small angles of incidence but as $\theta \rightarrow 90°$ the assumption fails. This assumption fails because at near grazing angles, the fluid velocity cannot be parallel to a boundary displaying a finite impedance. Also, the diffraction effects become larger as the angle of incidence approaches grazing. The second assumption, a plate of infinite extent, is valid for plates whose dimensions are larger than 1/2 an acoustic wavelength. At 10 kHz, an acoustic wavelength in aluminum is approximately 1 foot. The test plates used in this experiment were 3 × 3 foot and the infinite plate assumption is approximately valid. Again, this assumption becomes invalid at grazing angles because the cross-sectional area that the projector sees becomes smaller as the angles become larger.

Theoretical analysis of the scattered field produced by an elastic plate is broken into two parts, a field which would result if the plate were infinitely rigid plus a field produced by the radiation of the plate. The plate radiates sound because its elasticity allows it to bend with the incident wave. The plate will therefore oscillate and radiate sound. The scattered pressure, denoted as $\tilde{p}_{se}(x, y)$ is written as

$$\tilde{p}_{se}(x, y) = \tilde{p}_{s\infty}(x, y) + \tilde{p}_{r}(x, y) \tag{5.1}$$

where $\tilde{p}_{s\infty}(x, y)$ is the infinitely rigid plate response and $\tilde{p}_{r}(x, y)$ is the radiated response. The total acoustic pressure in front of the plate is the sum of the incident pressure and the scattered pressure

$$\tilde{p}(x, y) = \tilde{p}_{i}(x, y) + \tilde{p}_{se}(x, y) \tag{5.2}$$

where $\tilde{p}_{i}(x, y)$ is the incident field and is assumed planar. The incident wave is

$$\tilde{p}_i(x, y) = P_i \exp\left[j\ k(x \cos\theta - y\ \sin\theta)\right] \tag{5.3}$$

where the coordinates x, y and θ are defined in Figure 5.1.

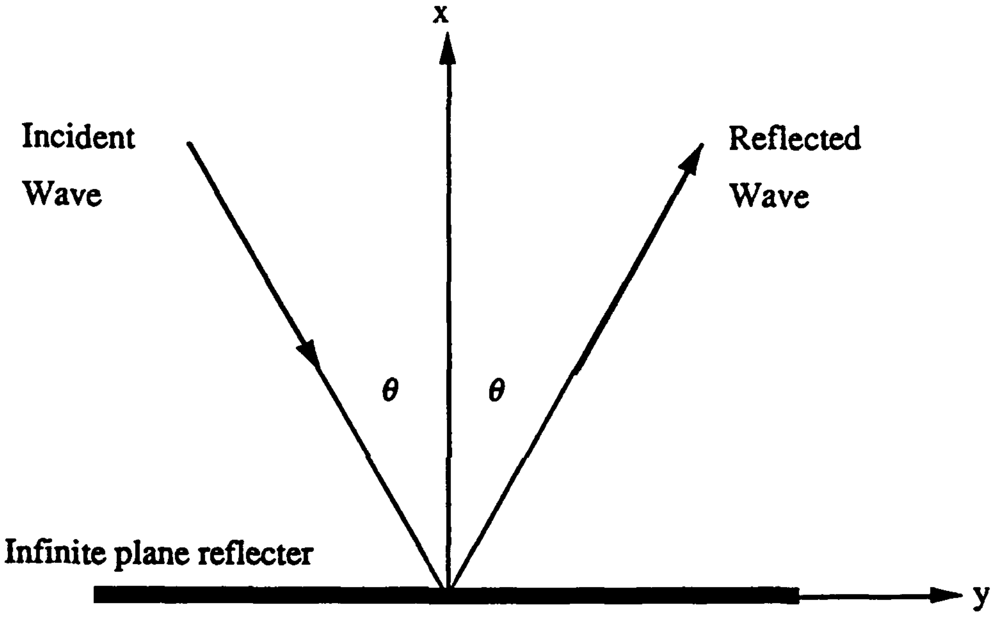

Figure 5.1. Sketch of an Infinite Plane Reflector.

The first part of the scattered field to be examined is that which would be reflected from an infinitely rigid boundary. This pressure is denoted by $\tilde{p}_{s\infty}(x, y)$. An infinitely rigid boundary will totally reflect an incident wave. This portion of the scattered field will therefore have the same magnitude as the incident pressure wave. The incident and reflected pressures for the rigid boundary have different phases. The pressure reflected from an infinitely rigid plate is

$$\tilde{p}_{s\infty}(x, y) = P_i \exp\left[-jk(x\cos\theta + y\sin\theta)\right] \quad . \tag{5.4}$$

The rest of the scattered pressure field is the result of the elastic properties of the plate. The pressure which is radiated by an elastic plate is

$$\tilde{p}_r(x, y) = \frac{2\,P_i \exp\left[jk\left(x\cos\theta + y\sin\theta\right)\right]}{jkh\left(\rho/\rho_s\right)\left[1 - \left(\omega/\omega_c\right)^2 \sin^4\theta\right]\cos\theta - 2} \tag{5.5}$$

where ρ_s is the density of the plate material and h is the plate thickness. The term ω_c is the coincidence or critical frequency and is the frequency at which the flexural wavelength in the plate equals the acoustic wavelength in the adjoining fluid. This frequency is defined as

$$\omega_c = \frac{\sqrt{12}\,c^2}{hc_p} \tag{5.6}$$

where $c_p = \sqrt{E/\left(1 - v^2\right)\rho_s}$ is the low frequency phase velocity of compressional waves in the elastic plate. For completeness, derivation of the radiated pressure for the elastic plate is given in Appendix B.

The total scattered field is obtained by combining the expression for the pressure reflected by a rigid plate, $\tilde{p}_{s\infty}(x, y)$, and the radiated pressure, $\tilde{p}_r(x, y)$. The scattered pressure is

$$\tilde{p}_{se}(x, y) = \tilde{p}_{s\infty}(x, y) + \tilde{p}_r(x, y)$$

$$= P_i \exp\left[jk\left(x \cos\theta + y \sin\theta\right)\right]$$

$$\times \left\{ \frac{jkh\left(\rho_s/\rho\right)\left[1 - \left(\omega/\omega_c\right)^2 \sin^4\theta\right]\cos\theta}{jkh\left(\rho_s/\rho\right)\left[1 - \left(\omega/\omega_c\right)^2 \sin^4\theta\right]\cos\theta - 2} \right\} . \quad (5.7)$$

The *superposition of this expression* with the expression describing the incident pressure describes the total acoustic field in front of the plate.

The pressure reflection factor is defined as the complex ratio of the scattered pressure to the incident pressure. This quantity on the plate surface (y = 0) is

$$\bar{R}(\theta) = \frac{\tilde{p}_{se}\left(r, \theta\right)}{\tilde{p}_i\left(r, 0\right)} = \frac{jkh\left(\rho_s/\rho\right)\left[1 - \left(\omega/\omega_c\right)^2 \sin^4\theta\right]\cos\theta}{jkh\left(\rho_s/\rho\right)\left[1 - \left(\omega/\omega_c\right)^2 \sin^4\theta\right]\cos\theta - 2} . \quad (5.8)$$

This expression is a function of only the plate and fluid parameters, incidence angle and frequency. It is not a function of distance from the surface of the plate. The reflection factor can also be calculated from the acoustic impedance. The measurement technique used in this study measures the impedance at a point located remote from but very close to the surface of the test plate. The impedance which is measured is a function of the surrounding fluid and of the perpendicular distance from the measurement point to the plate surface. The first step in calculating the reflection factor is to account for the separation between the measurement point and the plate surface. The surface impedance of the plate can be calculated from

$$\bar{Z}(\theta) = \bar{Z}_c \frac{\bar{Z}_M - j\,\bar{Z}_c \tan(kx \cos\theta)}{j\,\bar{Z}_c - \bar{Z}_M \tan(kx \cos\theta)} \tag{5.9}$$

where $\bar{Z}(\theta)$ is the surface impedance, $\bar{Z}_M$ is the impedance measured remote from the source and $\bar{Z}_c$ is the characteristic impedance of the surrounding water ($\bar{Z}_c = \rho_o c_o \approx 1.5 \times 10^6$ Rayles). The complex reflectivity can now be calculated from the surface impedance. The expression which relates these quantities is

$$\bar{R}(\theta) = \frac{\bar{Z}(\theta) - \bar{Z}_c}{\bar{Z}(\theta) + \bar{Z}_c} \quad . \tag{5.10}$$

These expressions allow us to compare established theoretical formulations with our experimental data.

5.3. Description of the Reflectivity Experiments

The experiments which were performed to test the accuracy of the two-sensor impedance measurement system involved measuring the complex reflectivity of submerged thin plates at oblique angles of incidence. The materials which were tested were a bare aluminum plate, a sheet of pressure release material and an aluminum plate coated on one side with absorbing rubber tiles. The aluminum plate was 3/8 inch thick. The pressure release material was a 1/4 inch thick sheet of bubble rubber. The absorptive rubber tiles were 1/4 inch thick and were glued to a 3/8 inch thick aluminum plate.

A bracket was designed and built which would allow the test plates to be supported by the trolley support mechanism. This bracket allowed the plates to be rotated about their axis to change the angle of incidence. An indicator attached to the support mechanism showed the angle of rotation. The two-hydrophone probe was held by the bracket at a fixed distance from the plate and aligned normal to the plate surface at a distance of 3/4 inches to the center of the probe.

One problem that is encountered when using finite plates are edge effects. Edge effects are caused by the discontinuity at the edge of the plate diffracting the pressure field. The two-sensor technique has a beneficial characteristic in that it can be employed in the near field of the plate. By keeping the probe as close as possible to the plate surface, we are able to minimize the edge effects. Also, by using a parametric array as a source, we are able to concentrate the incident pressure wave on the center of the plate. At large angles of incidence the effective area of the plate (the area perpendicular to the source) is reduced thereby increasing the problems of edge effects.

As a first test of the accuracy of the two-sensor measurements, the reflectivity of the bubble rubber (pressure release) boundary was measured and is shown in Figure 5.2. This figure shows a comparison of the theoretical value for the reflectivity from an ideal pressure release boundary, $R = 1 \exp\left(-180^\circ\right)$, with the experimental data measured with the two-sensor technique. The experimental points for the magnitude from the two-sensor technique are close to the theoretical value of 1.

The phase of the reflectivity is shown in Figure 5.2b. The measured phase varies within ±30° of a mean value which is slightly greater than the theoretical value. The variation in the experimental results may in part be caused by inaccurate measurement of the distance from the boundary to the hydrophones. The sheet of 1/4 inch thick bubble rubber used as a pressure release boundary was stretched onto a metal frame. This material is very flexible and by rotating the sheet through the water it sagged slightly. This sagging made it difficult to accurately measure the distance from the probe to the surface thereby introducing phase errors.

The next specimen to be tested was the bare aluminum plate. Values for the density and speed of sound used to calculate the theoretical curves were 2700 kg/m^3 and 6300 m/s respectively. Figure 5.3 shows a comparison of the theoretical curves to the experimental data. Figure 5.3a gives the magnitude of the reflectivity. This curve shows reasonable agreement between the experimental results and theoretical values. While this curve does

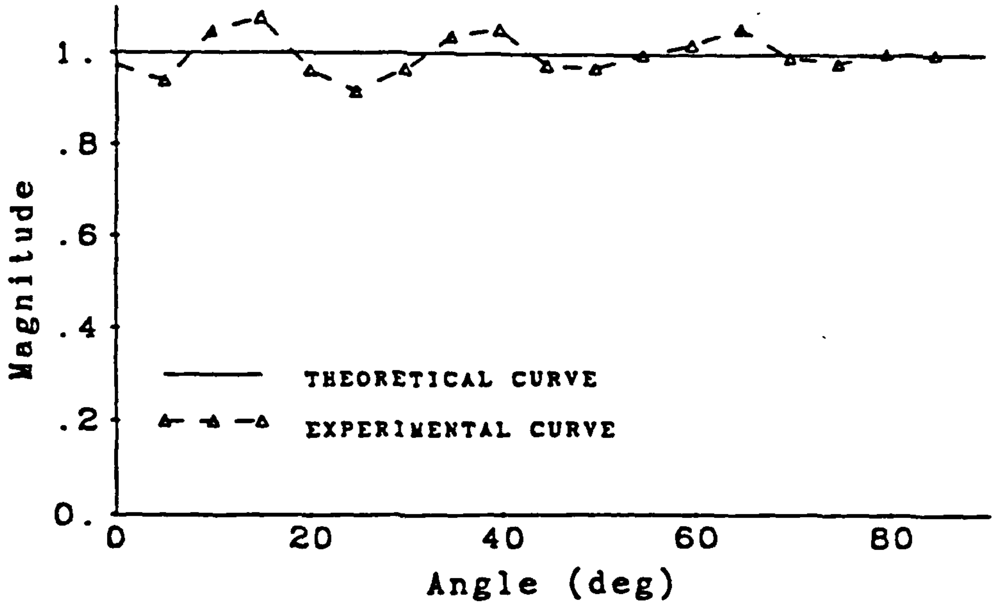

(a) Magnitude

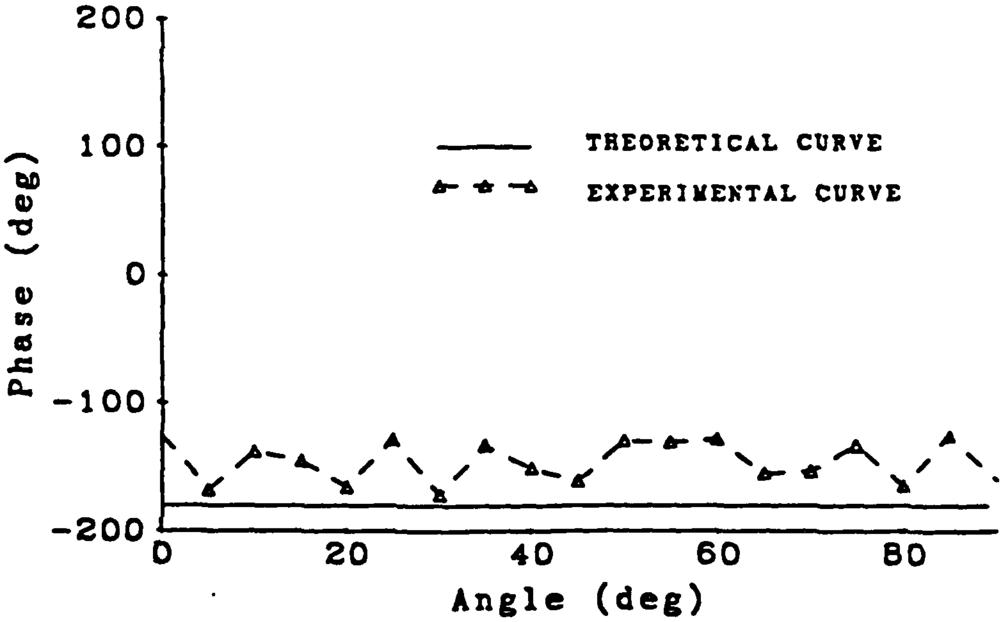

(b) Phase

Figure 5.2. Theoretical and experimental reflectivity of a pressure release boundary (bubble rubber) as a function of angle at 10 kHz.

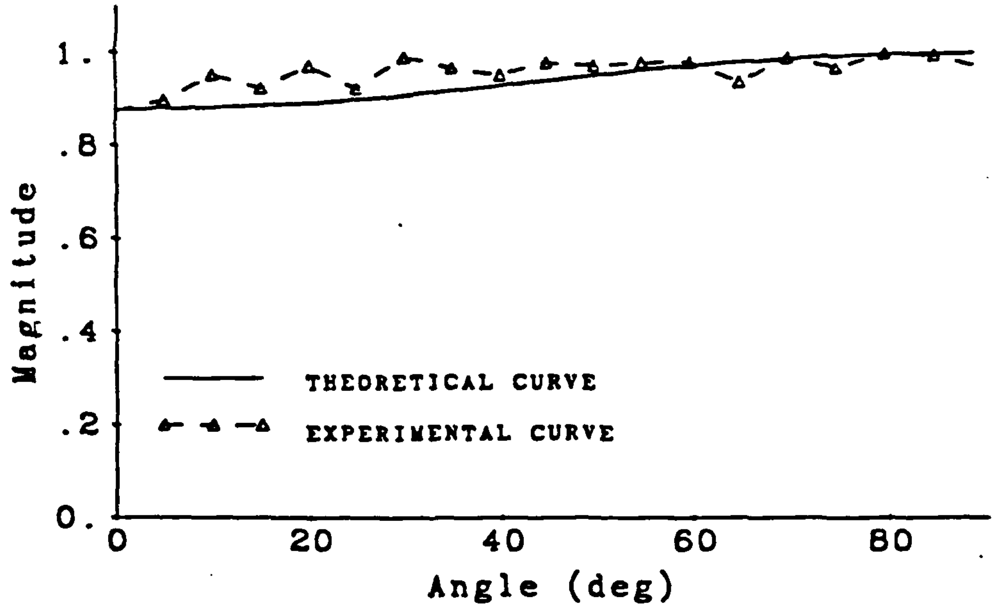

(a) Magnitude

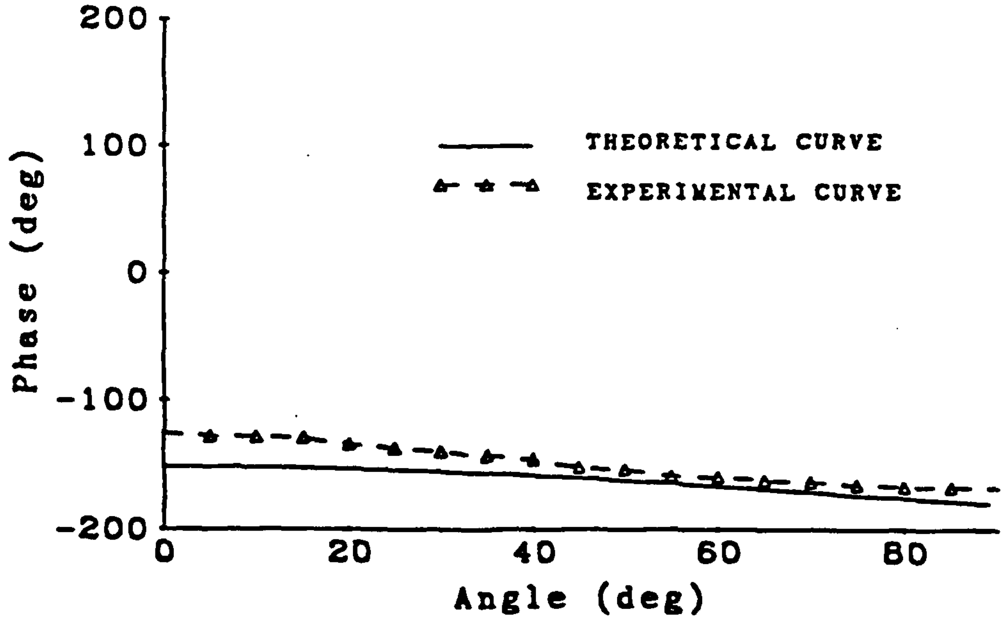

(b) Phase

Figure 5.3. Theoretical and experimental reflectivity of a 3/8 inch aluminum plate as a function of angle at 10 kHz.

show some of the variation with angle which occurred with the pressure release boundary, it does not vary nearly as much.

The phase of the reflectivity for the aluminum plate, shown in Figure 5.3b is in good agreement with the theory. Again, the data is biased from the theoretical curve indicating possible inaccurate determination of the distance from the plate to the probe. This curve did not fluctuate like the phase did with the bubble rubber sheet. Since the plate does not distort its shape like the bubble rubber sheet did, then the distance from the plate to the probe was more constant although the exact distance was different than what was assumed.

Finally, the technique was used on a sample with unknown reflectivity. This was the 1/4 inch tiles glued to a 3/8 inch thick aluminum plate. These tiles are designed for underwater acoustic applications. The results of the reflectivity measurements on this rubber covered plate are given in Figure 5.4. Note that Figure 5.4 shows two sets of experimental data to show reproducibility of the reflectivity measurements. The magnitude of the reflectivity, shown in Figure 5.4a, is approximately equivalent to the magnitude found for the bare aluminum plate. The magnitude with the tiles does vary over the angular range. The value does reach that of the totally reflecting surface at some angles. A possible explanation for this result would be air bubbles trapped in the glue under the tiles. Another interesting result is the large dip in the magnitude which was found at 55°. This result was consistently found in the two

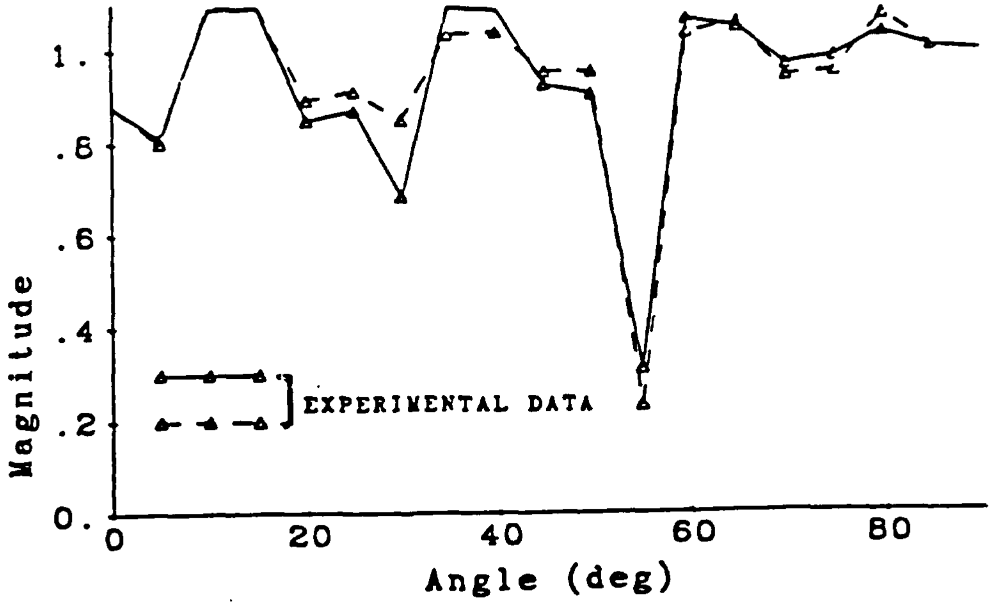

(a) Magnitude

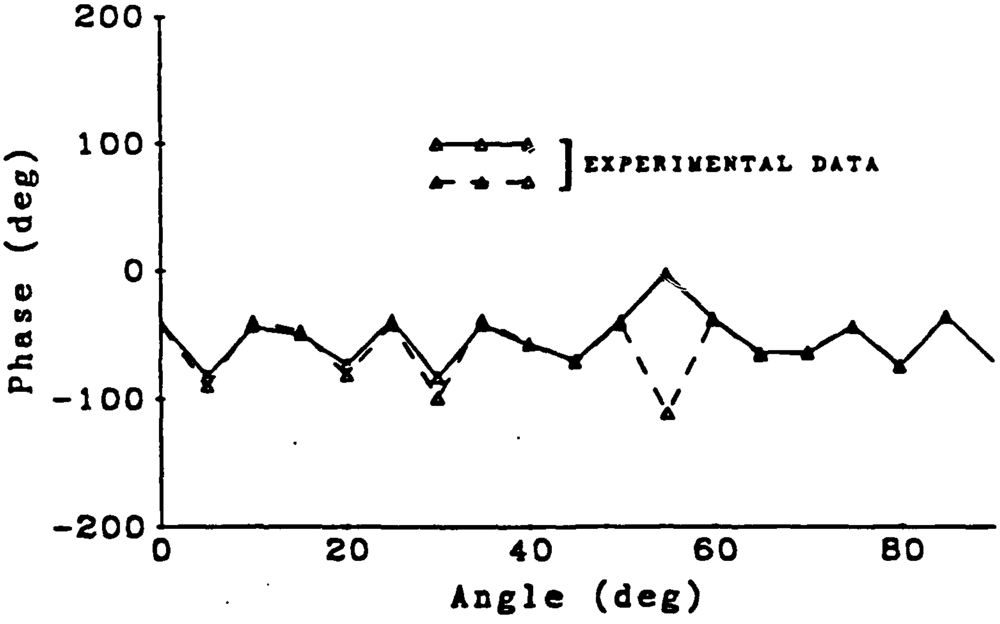

(b) Phase

Figure 5.4. Experimental reflectivity of a 3/8 inch aluminum plate covered with rubber tiles as a function of angle at 10 kHz.

separate measurements. This result shows that at this angle, a large percentage of the incident energy is not reflected the plate-rubber tile combination either because it is absorbed by or transmitted through the test plate. The dip did not show up in the measurements of the bare plate. Another factor with the rubber tile covered plate is that small gaps were present between the tiles. These gaps made the surface rough and scattered sound differently at different angles. The internal structure of the tiles is unknown. Some variation in density through the tile is possible and could cause some variation with angle in the reflectivity.

5.4. Conclusion and Recommendations for Further Research

The two-sensor technique has been shown to be a valuable tool for the study of various acoustic phenomena in air. In this study, we used the technique in water to measure the complex reflectivity of thin plates at oblique angles of incidence. Other methods for measuring this quantity, such as the standing wave ratio method can be very time consuming and impractical for oblique incidence angles particularly for underwater applications.

The measured complex reflectivity compares reasonably with the theoretical formulations over all angles. This is contrary to assumptions that the theoretical expressions do not hold as the angle of incidence approaches 90° where the plane wave assumption is no longer valid. Since the probe is actually located at a finite distance from the surface, the parametrically generated wave appears to provide "plane wave" like results.

The accuracy of the two-sensor method technique for measuring the complex reflectivity is dependent on the precision with which the distance from the measurement probe to the surface is measured. However, once this distance is known with accuracy, the distance need not be measured again throughout the experiment. This contrasts with the standing wave ratio method where the distance from the surface to the nodes must be measured for each frequency.

Using a two-sensor technique allows measurements to be made in the very near field of the plate. This minimizes edge effects which are common to other methods which require measurements made in the far field. Since the effects of diffraction at the edges of the plate are minimized, smaller test plates could be used.

Measurement of the acoustic intensity fields produced by the parametric array and the linear source shows the usefulness of the technique in understanding the acoustic phenomena. The vector plots of the acoustic intensity give a good insight into how the field is behaving. While the present system is able to consistently measure the active intensity, even the slight magnitude errors associated with the two hydrophones make the measurement of the low level reactive intensity fields difficult.

The other portion of this study concerned the use of the parametric array as a source of acoustic energy. This source was found to have a very narrow beam pattern at low frequencies. It was found that care must be taken to assure that the high level carrier signal be attenuated before amplification of the received signal is made. This attenuation was accomplished by a combination of electronic filters and a low-pass filter plate. The low-pass filter plate attenuated the high frequency carrier by 15 dB while passing the low frequency signal with only 2 dB of attenuation. It is believed that by increasing the levels of the carrier signal, the level of the difference frequency pressure could be increased. The amplifier that was made available was marginally powerful enough at the carrier frequency to allow measurements at the difference frequency of 10 kHz. The narrow beam patterns make the parametric array a useful tool for measurements made in small anechoic water tanks. Also, by using the narrow beam source to concentrate the pressure on the center of the test plate, edge effects could be reduced.

Recommendations for further research concerning the used of the two-sensor technique in underwater situations can be made. In terms of the measurement of the complex reflectivity, more accurate measurement of the distance from the probe to the sample should be sought.

Development of more sensitive hydrophone probes for the measurement of acoustic intensity would help to alleviate some of the magnitude mismatch bias errors. It is recommended that the perforated PZT composite hydrophone be further developed to provide a better frequency response and higher sensitivities. These probes could also be made smaller so that less disturbance of the acoustic field is made. In line with this recommendation would be the development of a four or five sensor probe which would allow the measurement of the two or three dimensional intensity field.

Use of pulses in conjunction with the two-sensor intensity method would help to decrease errors in the measurement due to reflections. This improvement would involve modifying the existing measurement system to allow the samples to be taken only when the direct pulse reaches the probe. Concerning the parametric array as a research tool, more studies are needed to increase the levels at the difference frequency. By increasing the power at the carrier frequency, the nonlinear effects of the water would be increased thereby increasing the difference frequency level. This would allow more accurate measurements of the low level reactive intensity to be made.

Measurement of the acoustic intensity and energy fields requires that the data be taken at many points in the tank. This can be very time consuming when the probe is moved manually. Also, exact placement of the probe is a function of how accurately the experimenter moves the probe. For these reasons, an important step in the development of the intensity technique for use in underwater settings would be the automation of probe placement.

BIBLIOGRAPHY

1. Taylor, H.O., "A Direct Method of Finding the Value of Materials as Sound Absorbers," Physical Review, Vol. 2, pp. 270-287, 1913.

2. Wente, E.C. and Bedell, E.H., "Measurement of Acoustic Impedance and the Absorption Coefficient of Porous Materials," Bell System Technical Journal, Vol. 7, pp. 140-146, 1939.

3. Meyer, E., et al., "Sound Absorption and Sound Absorbers in Water," NAVSHIPS 900, 166 U.S. Dept. of the Navy, Washington D.C., 1950.

4. Bolt, R. and Petrauskas, "An Apparatus for Accurate Measurement of the Acoustic Impedance of Sound-Absorbing Materials," Proc. Phys. Soc., Vol. 58, pp. 253-264, 1939.

5. Seybert, A.F. and Ross, D.F., "Experimental Determination of Acoustic Properties Using a Two-Microphone Random Excitation Technique," J. Acoust. Soc. Amer., Vol. 61(5), pp. 1362-1370, 1977.

6. Chung, J.Y. and Blaser, D.A., "Transfer Function Method of Measuring In-Duct Acoustic Impedance, I. Theory, II. Experiment," J. Acoust. Soc. Amer., Vol. 68(3), pp. 907-921, 1980.

7. Corbett, S.S., "A Two-Hydrophone Technique for Measuring the Complex Reflectivity of Materials in Water-Filled Tubes," M.S. Thesis in Acoustics, The Pennsylvania State University, 1983.

8. Sides, D.J. and Mulholland, K.A., "The Variation of Normal Layer Impedance With Angle of Incidence," J. Sound Vib., Vol. 14, pp. 139-142, 1971.

9. Davies, J.C. and Mulholland, K.A., "An Impulse Method of Measuring Normal Impedance at Oblique Incidence," J. Sound Vib., Vol. 67(1), pp. 135-149, 1979.

BIBLIOGRAPHY(continued)

10. Crammond, A.J. and Don, C.G., "Reflection of Impulses as a Method of Determining Acoustic Impedance," J. Acoust. Soc. Amer., Vol. 75(2), pp. 382-389, 1984.

11. Allard, J.F. and Sieben, B., "Measurements of Acoustic Impedance in a Free Field With Two Microphones and a Spectrum Analyzer," J. Acoust. Soc. Amer., Vol. 77(4), pp. 1617-1618, 1985.

12. Allard, J.F., Bourdier, R. and Bruneau, A.M., "The Measurement of Acoustic Impedance at Oblique Incidence With Two Microphones," J. Sound Vib., Vol. 101(1), pp. 130-132, 1985.

13. Lighthill, M.J., Proc. Roy. Soc. (London) A211, pp. 564, 1952; A222, pp. 1, 1954.

14. Ingard, K.U. and Pridmore-Brown, D.C., "Scattering of Sound by Sound," J. Acoust. Soc. Amer., Vol. 28(3), pp. 367-369, 1956.

15. Westervelt, P.J., "Scattering of Sound by Sound," J. Acoust. Soc. Amer., Vol. 29(2), pp. 199-203, 1957.

16. Westervelt, P.J., "Scattering of Sound by Sound," J. Acoust. Soc. Amer., Vol. 29(8), pp. 935, 1957.

17. Westervelt, P.J., "Parametric Acoustic Array," J. Acoust. Soc. Amer., Vol. 35(4), pp. 535-537, 1963.

18. Lauvstad, V. and Tjötta, S., "Problem of Sound Scattered by Sound," J. Acoust. Soc. Amer., Vol. 34(8), pp. 1045-1050, 1962.

19. Muir, T.G. and Willette, J.G., "Parametric Acoustic Transmitting Arrays," J. Acoust. Soc. Amer., Vol. 52(5), pp. 1481-1486, 1972.

20. Berktay, H.O. and Shooter, J.A, "Near Field Effects in End-Fire Arrays," J. Acoust. Soc. Amer., Vol. 53(2), pp. 550-556, 1972.

BIBLIOGRAPHY(continued)

21. Novikov, B.K., Rudneko, O.V. and Soluyan, S.I., "Parametric Ultrasonic Radiators," Soc. Phys. Acoust., Vol. 21(4), pp. 365-368, 1976.

22. Fenlon, F.H., "A Weak Interaction Model for the Axial Difference Frequency Field of Symmetric and Asymmetric Parametric Acoustic Transmitting Arrays," J. Sound Vib., Vol. 64(1), 1979.

23. Elko, G.W., "Frequency Domain Estimation of the Complex Acoustic Intensity and Acoustic Energy Density," Ph.D. Thesis in Acoustics, The Pennsylvania State University, 1984.

24. Thompson, J.K. and Tree, D.R., "Finite Difference Approximation Errors in Acoustic Intensity Measurements," J. Sound Vib., Vol. 75(2), pp. 229-238, 1981.

25. Clay, C.S. and Medwin, N. "Acoustical Oceanography," New York, John Wiley & Sons, 1977.

26. Muir, T.G. and Blue, J.E., "Experiments on the Acoustic Modulation of Large Amplitude Waves," J. Acoust. Soc. Amer., Vol. 46(3), pp. 227-232, 1969.

27. Naze, J. and Tjötta, S., "Nonlinear Interaction of Two Sound Beams," J. Acoust. Soc. Amer., Vol. 37, pp. 174-175 (L), 1965.

28. Safari, A., Newnham, R.E., Cross, L. E. and Schulze, W.A., Perforated PZT-Polymer Composites for Piezoelectric Transducer Applications," Ferroelectrics, Vol. 41, pp. 197-205, 1982.

29. Eller, A.I., "Application of the USRD type E8 Transducer as an Acoustic Parametric Source," J. Acoust. Soc. Amer., Vol. 56(6), pp. 1735-1739, 1974.

30. Junger, M. and Feit, D., "Sound, Structures, and Their Interaction," Second Edition, MIT Press, Cambridge, Mass, 1986.

Appendix A

DERIVATION OF FREQUENCY DOMAIN ESTIMATORS

This appendix outlines the derivation of the frequency domain estimators for the acoustic intensities, energies and impedances. These estimators are utilized to convert the time domain pressure data into frequency domain intensity data. Derivation for the frequency domain estimator for the acoustic intensity begins with Eq. (2.8)

$$\vec{I} = -\frac{1}{2\rho_o \Delta r} E\left\{\left[p_1(t) + p_2(t)\right]\int\left[p_2(t) - p_1(t)\right]dt\right\} \quad . \qquad (A.1)$$

Note that in this appendix, a simplification in notation of $p_i(r_i, t) = p_i(t)$ is made. By expanding Eq. (A.1) and using the substitution

$$z_i(t) = \int p_i(t)\, dt \qquad (A.2)$$

(A.1) can be written as

$$\vec{I} = -\frac{1}{2\rho_o \Delta r} E\left\{p_1(t)\, z_2(t) + p_2(t)\, z_2(t) - p_1(t)\, z_1(t) - p_2(t)\, z_1(t)\right\}$$

$$= -\frac{1}{2\rho_o \Delta r}\left[E\left\{p_1(t)\, z_2(t)\right\} + E\left\{p_2(t)\, z_2(t)\right\}\right.$$

$$\left. - E\left\{p_1(t)\, z_1(t)\right\} - E\left\{p_2(t)\, z_1(t)\right\}\right] \quad . \qquad (A.3)$$

Simplification of this expression into one which is easier to implement is made by using the Parseval relation to convert the expected value operators into spectral quantities. The Parseval relation can be expressed as a cross-correlation function

$$R_{pz}(0) = E\left\{p(t)\, z(t)\right\} \tag{A.4}$$

which for a stationary ergodic process becomes

$$\begin{aligned} R_{pz}(0) &= \lim_{T\to\infty} \frac{1}{T} \int_{-T/2}^{T/2} p(t)\, z(t)\, dt \\ &= \lim_{T\to\infty} \frac{1}{T} \int_{-T/2}^{T/2} p(t) \int_{0}^{t} p(\tau)\, d\tau\, dt \end{aligned} \tag{A.5}$$

and with the use of Parseval's relation,

$$R_{pz}(0) = \frac{1}{2\pi} \int_{-\infty}^{\infty} S_{pz}(\omega)\, d\omega \quad . \tag{A.6}$$

Further, since z(t) is given as an integral of pressure over time, we can replace the variable z by p using the frequency domain equivalent to integration

$$S_{pz}(\omega) = \frac{1}{j\omega} S_{pp}(\omega) \quad . \tag{A.7}$$

Since $p_1(t)$ and $p_2(t)$ are real processes,

$$S_{p_1p_2}(\omega) = S^*_{p_2p_1}(\omega) \quad . \qquad (A.8)$$

The complex intensity spectrum estimator can now be written as

$$\vec{I}^{\,c}(\omega) = -\frac{1}{2j\omega\rho_o\Delta r}\left\{S_{p_2p_2}(\omega) - S_{p_1p_1}(\omega) - j2Im\left[S_{p_2p_1}(\omega)\right]\right\} \quad . \qquad (A.9)$$

Taking the real part of this expression, the active intensity is

$$\vec{I}(\omega) = Re\left[\vec{I}^{\,c}(\omega)\right] = \frac{1}{\omega\rho_o\Delta r} Im\left[S_{p_2p_1}(\omega)\right] \quad . \qquad (A.10)$$

The reactive intensity, given by the imaginary part of (A.9) , is

$$\vec{Q}(\omega) = Im\left[\vec{I}^{\,c}(\omega)\right] = \frac{1}{2\omega\rho_o\Delta r}\left\{S_{p_2p_2}(\omega) - S_{p_1p_1}(\omega)\right\} \quad . \qquad (A.11)$$

The frequency domain estimators for the potential and kinetic energy densities are developed in the same manner. Starting with the time domain estimator for the potential energy density

$$V = \frac{1}{16\rho_o c^2} E\left\{p_1(t)\, p_1^*(t) + p_2(t)\, p_2^*(t) + p_1(t)\, p_2^*(t) + p_2(t)\, p_1^*(t)\right\}$$

$$= \frac{1}{16\rho_o c^2}\left\{R_{p_1p_1}(0) + R_{p_2p_2}(0) + R_{p_1p_2}(0) + R_{p_2p_1}(0)\right\} \quad . \qquad (A.12)$$

By again using the Parseval relation and equating the integrands, we obtain

$$V(\omega) = \frac{1}{16\rho_o c^2}\left\{S_{p_1p_1}(\omega) + S_{p_2p_2}(\omega) + S_{p_1p_2}(\omega) + S_{p_2p_1}(\omega)\right\} \quad . \quad \text{(A.13)}$$

Noting again that (see Eq. (A.8))

$$S_{p_1p_2}(\omega) = S^*_{p_2p_1}(\omega) \quad \text{(A.14)}$$

the potential energy density estimator is given as

$$V(\omega) = \frac{1}{16\rho_o c^2}\left\{S_{p_1p_1}(\omega) + S_{p_2p_2}(\omega) + 2\,Re\left[S_{p_1p_2}(\omega)\right]\right\} \quad . \quad \text{(A.15)}$$

The kinetic energy density estimator is derived from

$$\hat{T} = \frac{1}{\omega^2\rho_o(\Delta r)^2} E\left\{p_2(t)\,p_2^*(t) + p_1(t)\,p_1^*(t) - p_1(t)\,p_2^*(t) - p_2(t)\,p_1^*(t)\right\}$$

$$= \frac{1}{\omega^2\rho_o(\Delta r)^2}\left\{R_{p_1p_1}(0) + R_{p_2p_2}(0) - R_{p_1p_2}(0) - R_{p_2p_1}(0)\right\} \quad . \quad \text{(A.16)}$$

Recalling that

$$S_{p_1p_2}(\omega) = S^*_{p_2p_1}(\omega) \quad \text{(A.17)}$$

leads to the kinetic energy density estimator

$$\hat{T}(\omega) = \frac{1}{\omega^2 \rho_o (\Delta r)^2} \left\{ S_{p_1 p_1}(\omega) + S_{p_2 p_2}(\omega) - 2\, Re \left[S_{p_1 p_2}(\omega) \right] \right\} \quad . \quad (A.18)$$

Appendix B

PRESSURE RADIATED FROM AN ELASTIC PLATE

Derivation of the pressure radiated from an elastic plate begins with the equation of motion for a plate[29]. This equation of motion is

$$\frac{D}{\omega^2}\left(k^4\sin^4\theta - k_f^4\right)\ddot{W}\ \exp(jkx\ \sin\theta)$$
$$= \left[2P_i + \frac{j\rho}{k\ \sin\theta}\ \ddot{W}\ \right]\exp(jkx\ \sin\theta) \qquad \text{(B.1)}$$

where D is the flexural rigidity of the plate, k_f is the flexural wavenumber in the plate and $\ddot{W}$ is the plate acceleration. Through the acceleration, we can obtain an expression for the radiated pressure. The plate acceleration, $\ddot{W}$, is obtained by solving equation (B.1). Simplification of this expression is made by dividing by the exponential and by the ratio $D\,k_f^4/\omega^2\cos\theta$. The resulting equation is

$$\left[\left(\frac{k}{k_f}\right)^4 \sin^4\theta - 1\right]\cos\theta\ \ddot{W}$$
$$= \left[2\ P_i\cos\theta\left(\frac{\omega^2}{D\ k_f^4}\right) + \frac{j\rho c}{\omega}\left(\frac{\omega^2}{D\ k_f^4}\right)\ddot{W}\right] \quad . \text{(B.2)}$$

Further simplification of this expression is made by substituting for the ratio $\left(k/k_f\right)^4$ in terms of the coincidence frequency with

$$\left(\frac{k_f}{k}\right)^4 = \left(\frac{\rho_s\, h}{D}\right)\frac{c^4}{\omega^2} \tag{B.3}$$

and

$$\omega_c^2 = c^4 \left(\frac{\rho_s\, h}{D}\right) \quad . \tag{B.4}$$

These two expressions give

$$\left(\frac{k}{k_f}\right)^4 = \left(\frac{\omega}{\omega_c}\right)^2 \quad . \tag{B.5}$$

Finally, setting $D\, k_f^4/\omega^2 = \rho_s\, h$, we obtain the following for the equation of motion

$$\left[\left(\frac{\omega}{\omega_c}\right)^2 \sin^4\theta - 1\right] \cos\theta\, \ddot{W} = \left[\frac{2\, P_i}{\rho_s\, h}\cos\theta + \frac{j\rho}{kh\rho_s}\ddot{W}\right] \quad . \tag{B.6}$$

Solving this expression for the complex acceleration amplitude, we obtain

$$\ddot{W} = \frac{-2\, P_i \cos\theta}{\rho h\left\{jkh\left(\rho/\rho_s\right) + \left[1 - \left(\omega/\omega_c\right)^2 \sin^4\theta\right]\cos\theta\right\}} \quad . \tag{B.7}$$

The relationship between the radiated pressure and the acceleration is made by satisfying the Helmholtz equation and the boundary conditions at the plate surface. The pressure field satisfying these conditions is

$$p_r(x, y) = j\rho\ddot{W} \cos\left(k_s x\right) \frac{\exp\left[j\left(k^2 - k_s^2\right)^{1/2} y\right]}{\left(k^2 - k_s^2\right)^{1/2}} \tag{B.8}$$

with $k_s = k \sin\theta$ and $\left(k^2 - k_s^2\right)^{1/2} = k \cos\theta$. Hence, the expression relating the radiated pressure to the acceleration can be written as

$$p_r(x, y) = \frac{j\rho\ddot{W}}{k \cos\theta} \exp\left[jk(x \cos\theta + y \sin\theta)\right] \quad . \tag{B.9}$$

By substituting equation (B.7) into this expression, we obtain the radiated pressure

$$p_r(x, y) = \frac{2\, P_i \exp\left[jk(x \cos\theta + y \sin\theta)\right]}{jkh\left(\rho/\rho_s\right)\left[1 - \left(\omega/\omega_c\right)^2 \sin^4\theta\right] \cos\theta - 2} \quad . \tag{B.10}$$